UNIVERSITAT POLITÈCNICA DE CATALUNYA
BARCELONATECH

Large-scale CFD and micro-particle simulations in a large human airways under sniff condition and drug delivery application

by
Hadrien Calmet

Fisica computacional i aplicada PhD program

Large-scale CFD and micro-particle simulations in a large human airways under sniff condition and drug delivery application

Doctoral thesis by: Hadrien Calmet

Thesis advisor: Guillaume Houzeaux

A thesis presented for the degree of
Doctor of Philosophy

Departament de Física
Universitat Politècnica de Catalunya
Spain
October 2020

Abstract

As we inhale, the air drawn through our nose undergoes successive accelerations and decelerations as it is turned, split, and recombined before splitting again at the end of the trachea as it enters the bronchi. Fully describing the dynamic behaviour of the airflow and how it transports inhaled particles poses a severe challenge to computational simulations. The dynamics of unsteady flow in the human large airways during a rapid and short inhalation (a so-called sniff) is a perfect example of perhaps the most complex and violent human inhalation inflow. Combining the flow solution with a Lagrangian computation reveals the effects of flow behaviour and airway geometry on the deposition of inhaled microparticles.

Highly detailed large-scale computational fluid dynamics allow resolving all the spatial and temporal scales of the flow, thanks to the use of massive computational resources. A highly parallel finite element code running on supercomputers can solve the transient incompressible Navier-Stokes equations on unstructured meshes. Given that the finest mesh contained 350 million elements, the study sets a precedent for large-scale simulations of the respiratory system, proposing an analysis strategy for mean flow, fluctuations, wall shear stresses, energy spectral and particle deposition on a rapid and short inhalation.

Then in a second time, we proposed a drug delivery study of nasal sprayed particle from commercial product in a human nasal cavity under different inhalation conditions; sniffing, constant flow rate and breath-hold. Particles were introduced into the flow field with initial spray conditions, including spray cone angle, insertion angle, and initial velocity. Since nasal spray atomizer design determines the particle conditions, fifteen particle size distributions were used, each defined by a log-normal distribution with a different volume mean diameter.

This thesis indicates the potential of large-scale simulations to further

understanding of airway physiological mechanics, which is essential to guide clinical diagnosis and better understanding of the flow and delivery of therapeutic aerosols, which could be applied to improve diagnosis and treatment.

Declaration

This is to certify that the work presented in this thesis has been carried out at Barcelona supercomputing center and has not been previously submitted to any other university or technical institution for a degree or award. The thesis comprises only my original work. Due acknowledgement is specifically made where appropriate.

Hadrien Calmet

Contents

List of Figures

7

List of Tables

Nomenclature

$\boldsymbol{F}_d$ Drag force

$\boldsymbol{F}_g$ Gravitational and buoyancy force

$\boldsymbol{\varepsilon}(\mathbf{u})$ Velocity strain rate

Δt Temporal resolution

Δ Mesh grid resolution

η Kolmogorov scale

η_{dep} Particle deposition efficiency

η_{nasal} Nasal cavity deposition efficiency

λ Taylor microscale

$\mathbf{a}_p$ Acceleration of the particle

$\mathbf{S}(\bar{\mathbf{u}})$ Large-scale rate-of-strain tensor

$\mathbf{u}$ Velocity of the fluid

$\mathbf{u}_p$ Velocity of the particle

$\mathbf{x}_p$ Position of the particle

μ Dynamic viscosity of the fluid

ν Kinematic viscosity of the fluid

ν_{sgs} Subgrid-scale kinetic viscosity

$\overline{\mathbf{u}}$ filtered velocity of the fluid

ρ Density of the fluid

ρ_p Density of the particle

$\tau_{\mathbf{ij}}(\overline{\mathbf{u}})$ subgrid scale (SGS) stress tensor

ε Turbulent dissipation rate

Cd Drag coefficient

d_p Diameter of the particle

$Dv50$ Volume median diameter of log-normal distribution

E Energy flux

I_{turb} Turbulence intensity

IP Inertial parameter

m_p Mass of the particle

N_{dep} Number of particles deposited

N_{in} Number of particles injected

p Static pressure of the fluid

Q Volumetric flow rate

TKE Turbulence kinetic energy

u_* Friction velocity at the wall

V_p Volume of the particle

y Distance to the wall

y^+ Non-dimensional wall distance

$\mathrm{Re_p}$ Particle Reynolds number

CFD   Computational Fluid Dynamic

DCG   Deflated Conjugate Gradient method

GMRES Generalized minimal residual method

I/O   Input/Output

LES   Large Eddy Simulation

MPI   Message passing interface

OpenMP Open Multi-Processing

RANS   Reynolds Averaged Navier-Stokes

Re   Reynolds numbers

Chapter 1

Introduction

The purpose of this chapter is to introduce the state of the art of this specific field of respiratory system. Including two parts, one with the airflow describing the main issues, for instance the choice of the numerical model, the nature of the inflow and the geometry modeling are presented. Then the second state of the art about the particle transport and spray drug delivery related on the human nasal cavity are developed.

1.1 Airflow

The flow in the human large airways is rich with complexity and variety. The geometry is extraordinarily complex with constriction zones and rapid changes in direction. Accordingly, a wide range of local Reynolds numbers (Re) occurs in the human large airways, which involve a mixture of various fluid motions. Further complications arise due to the fact that the breathing pace can change dramatically: at rest, whilst smelling or under heavy exercise. Previous studies state than while one is resting, flow is quasi-steady and laminar (see Zhao et al. [1]). On the other hand, during the kind of inspiration typical of a sniff, which is a rapid and short inhalation, the assumption of laminar flow is not justified. With the high amplitude of the inhalation and the rapid acceleration occurring during the sniff, the flow is transitional and turbulent. Thus accurate numerical modeling is needed. Unsteady flow studies has been performed, where Se and al.[2] used a low-Reynolds $k-\omega$ model, Lindemann et al.[3] used an RNG $k-\epsilon$ model. Today Large Eddy Simulation (LES) model becomes more and more used by the community [4, 5, 6, 7, 8] .

Zhu et al.[9] used the low Reynolds number (LRN) k–ω turbulent model for transient simulations at three ventilation rates, 7.5 L/min, 15 L/min and 30 L/min. While the LES model captures a greater range of turbulence scales, justification for laminar and low-Reynolds k–ω models comes from the predominantly lower flow rates during the respiration cycle. As a comparison, steady simulations have generally adopted a laminar flow assumption for flow rates of 15L/min or less [10, 11, 12, 13, 14, 15], low-Reynolds k–ω models for flow rates greater than 15L/min [16, 17, 18, 19, 20, 21], and to a lesser extent other turbulent models including $k - \epsilon$ [22, 23, 24], and v2-f [25] models.

Doorly et al. [26] investigated variations in the nasal airways and in the modeling of flow in this complex geometry, providing comparisons [27] with numerical and experimental models. Lintermann et al. [28] also investigated variations in nasal airways, although under the scope of the respiratory efficiency. They classified different nasal cavities into ability groups, which support the *a priori* decision process on surgical interventions.

To ensure a realistic inspiration model and velocity profile at the naris, Taylor et al. [29] demonstrated that incorporating the external nose and face not only reproduces the physiological situation, but also from a computational point of view furnishes additional information, such as the spatial position of particles over time. Other works, such as Jayaraju et al. [30] and Ball et al. [31], used the upper human airway with an idealized geometry and presented results concerning mean flow and flow structures. Contrary to Jayaraju et al. and Ball et al., Ghahramani et al. [32] used a realistic model to perform a numerical analysis in the upper human airway. Saksono et al. [33] and Lin et al. [34] demonstrated that incorporating the nasal cavity into the upper airway is essential in order to study the flow in the throat, since the results with and without the nasal cavity are dramatically different.

Many works have been performed with simplified models [35], idealized models [30, 31], or using several realistic models [26, 27], for example Choi et al. [36] investigated the variabilities of intra- and inter-subject of airflow in the human lung.

The laryngeal jet is the most important flow feature occurring in the throat during rapid inhalation. This phenomenon determines mean and fluctuating behaviors of the flow downstream in the tracheobronchiol airways [34]. The laryngeal jet involves various flow types, such as noncircular confined turbulent jet, open cavity flow, shear layers and curved and bifurcating turbulent and transitional pipe flow [36]. Choi et al. [36] detailed the unsteady behavior of the laryngeal jet through spectral analysis, Varghese et

13

al. [37], described similar behaviors with the laryngeal jet with turbulence in a stenotic flow.

One of the objective of this study is to determine the location of transition in the airways during a sniff using a realistic anatomical model and a high resolution of the computational mesh. The spatial and temporal resolutions in this study are very fine, in the order of $1\mu s$ for the temporal resolution and $0.1mm$ for the spatial resolution throughout the domain; well beyond the resolution commonly applied in the literature today [38, 39].

1.2 Particle transport and drug delivery

The nasal cavity is the first line of defense in the respiratory tract that filters out inhaled airbone particulate matters, thus protecting the delicate low airways ([40]). Besides particle deposition in human nasal cavity has been extensively studied in the past ([41, 42, 43, 44, 45, 46, 47]) including nano and micro-particles, in-vitro and in-vivo methods. However particle deposition studies based on realistic human upper airway are less popular ([30, 48]). Furthermore the nature of the inhalation as steady (constant) flow rate was also extensively studied ([49, 50, 51, 52]). Although less investigations exist with unsteady inhalation flow rate as [53] who compared micro-particle deposition under cyclic inspiratory flow with equivalent steady conditions. They concluded that while the general trend was similar, the particle deposition for equivalent steady condition cannot accurately predict the particle deposition for cyclic inspiratory flow. To study the drug delivery of aerosols, the aspect of unsteady particle tracking resulting of the transient airflow is an issue which needs to be addressed in detail.

There is a specific region where drug delivery is particularly important. The olfactory region (upper meatus below the cribiform plate) ([54]) is the challenging target of drug delivery of aerosols in the nasal cavity. The route taken by inhaled particles to reach the brain, via the olfactory pathway, is unclear. There is increasing evidence that inhaled particulate matter depositing in the olfactory region can migrate to the brain along the olfactory bulb as mentioned [55]. Due to the protected area of the human olfactory epithelium, it is estimated that only 10% of inhaled air actually reaches the olfactory region during a normal resting breath, see [56]. As far as the authors know, there is no literature about micro-particle deposition in the human upper airways under sniff condition. The nasal cavity is a promising

14

route for systemic drug delivery due to potential drug absorption through the porous endothelial membrane of the rich vascular capillary bed underneath the nasal mucosa [57, 58]. However, studies have shown many commercially available nasal spray devices deposit most of the atomized drug in the anterior portion of the nose [59, 60], and missing the nasal mucosa in the turbinate regions. Understanding deposition of atomized droplets within the main nasal passage provides insight effective nasal spray device design for targeted drug delivery.

Guo et al. [61] showed that a low viscosity nasal spray formulation with a wider plume angle (69°) and small volume median diameter ($Dv50 = 47 - 86\mu m$) enhanced deposition in the main nasal passage compared to a higher viscosity formulation (32° plume angle; $Dv50 = 100 - 130\mu m$). The liquid viscosity was the most significant influence on droplet size due to the liquid breakup during atomization. Foo et al. [62] found that both spray cone angle and administration angle were important factors in determining deposition efficiency, where sprays with small cone angles were capable of reaching 90% deposition efficiency in the main nasal passage. It also found that particle size, viscosity, and inspiratory flow rate had relatively minor influence on deposition within the nasal cavity.

Other experimental studies include [63] that found greater anterior deposition in children (12 year old model) leading to decreased effectiveness; Pu et al. [64] investigated the effect of spray formulation (e.g. viscosity) on deposition patterns in a nasal cavity cast; Warken et al. [65] found the optimum administration angle for nasal sprays applied to ten 3D-printed nasal cavity replicas, and showed that it could increase deposition in the main nasal passage. They also suggested inhalation flow had no significant effect on the deposition pattern, based on steady flows of 10 and 60 L/min. However this may differ if unsteady inhaled flow or a sniff was used. Characterisation of the nasal spray was performed experimentally with measurements of external characteristics of unsteady spray atomization from a nasal spray device [66], and measurements of droplet size distribution and analysis of nasal spray atomization from different actuation pressure [67]. Newman et al. [68] evaluated the role of in-vitro and in-vivo methods of two similar nasal pump sprays, where significant differences in in-vitro parameters were not reflected in differences in nasal deposition in-vivo. This suggests that any in-vivo studies (and to some extent in-silico studies) should expect differences in results.

Computational studies of sprayed particle deposition in the human nasal

cavity have found relationships for deposition efficiencies or penetration into the turbinate mucosa of the main nasal passage, with nasal spray parameters, such as spray cone angle and the particle size distribution produced. Kimbell et al. [69] found that particle penetration past the nasal valve improved when particle inertia was reduced through smaller particle diameters or reduced spray velocity. The positioning of 1cm into the nostril, with inspiratory flow present was recommended. Inthavong et al. [59, 25] found that if the particles exhibited increased tangential velocities (through swirling) as it exited the spray nozzle, then increased deposition in the turbinate region could be achieved. This assumed a hollow cone spray which is the typical spray formation produced from pressure-swirl atomizers.

Other computational studies include: Keeler et al.[70] who investigated the influence of nasal airway geometry from different ethnic groups on spray particle deposition and found that white and Latin Americans had the least patent nasal cavity, although this was based on four models per ethnic group; Kiaee et al. [71] that found particle diameter and particle injection speed, were the dominant parameters (other parameters were spray cone angle, spray release direction, and particle injection location) that influenced deposition in seven adult nasal airways; and Fung et al. [72] performed CFD modelling to characterise the nasal spray atomization stage. Djupesland et al. [73] showed a bi-directional nasal delivery concept reduced lung deposition by taking advantage of the posterior connection between the nasal passages persisting when the soft palate automatically closes during oral exhalation.

The influence of breathing conditions during spray delivery on the uptake of the drugs are unknown. Inhalation can be a short burst of high flow rate (as a sniff), a shallow steady breath, or zero breathing found in a breath hold. However, many computational studies with drug delivery have only applied a steady flow condition. For example studies have used laminar steady inspiratory flow rates [60, 59, 71, 70] when the flow rate was approximately <15L/minor, and steady RANS (Reynolds Averaged Navier-Stokes) turbulent flows when the flow rate was >20L/min [25, 74]. While there are many ways to inhale during drug delivery, this study looked at the influence of a sniff compared to commonly used steady flow rate, and a zero inhalation flow on particle deposition in the human nasal cavity.

To increase the accuracy of the work, high fidelity LES turbulence model was used to account for the transient, and unstable nature of the fluid-particle dynamics in the flow field. While the RANS models provide efficient computational cost, studies showed the fluid-particle turbulent dispersion coupling

required empirically based adjustments [75, 76, 77]. To avoid this, the Large Eddy Simulation (LES) method was used for the transient, and turbulent flow behaviour as provides anisotropic turbulent fluctuations which are transferred directly onto the particles.

Studies employing LES techniques include: Bates et al. [7] assessed the relationship between movement and airflow in the upper airway motion determined from magnetic resonance imaging; Farnoud et al. [78] and Payri Marin et al. [79] used the LES model to deliver mono-disperse particles with the diameters of 2.4 and 10 μm uniformly and randomly injected at the nostrils with constant inhalation flow rates of 4.78 L/min and 7.5 L/min; Covello et al. [80] studied droplet deposition for different sizes of water droplets on a patient-specific anatomy under steady inspiration at two breathing intensities; Bahmanzadeh et al. [5] investigated airflow and micro-particle deposition in human nasal airway pre- and post-virtual sphenoidotomy surgery ; Mylavarapu et al. [81] inspected the airflow through the nasal cavity comparing its results to experimental pressure drop measurements; and Li et al. [82] evaluated the performance of various turbulence models including the LES model for airflow through a nasal cavity. It's expected that the results using LES method will contribute to the existing literature regarding nasal spray device performance.

1.3 Main contributions

The main contributions of this thesis are:

- Dynamics of unsteady flow in the large airways during a rapid inhalation through large-scale CFD on a highly-detailed geometry.

- The results presented here were obtained on a series of progressively refined computational meshes, the finest one containing 350 million elements.

- It was also found that spontaneous fluctuations in nasal airflow velocities occur, resulting from shear layer instabilities (jet breakdown and flapping).

- It has been found that whilst spontaneous fluctuations in velocity arise in the nose, the dominant site of turbulence production during inhalation is in the supra-glottic region, as opposed to the glottis itself.

- The most important deposition mechanism for micro-particle is inertial impaction. As a consequence of their higher inertia and deviation from the flow streamlines, larger particles (10 and 20 μm) stay trapped in the nasal cavity which plays the role of filter. Smaller particles (1 and 5 μm) with low inertia can penetrate further.

- Some hot spots are observed, of which the most important is the laryngeal region, where chaotic flow highly promotes particle deposition.

- The polydisperse particles from the nasal spray under sniff condition, produced an increase of 300% deposition in surface area coverage compared with the different inhalation conditions in the main nasal passage which is where the highly vascularised mucosal walls exist.

- Other targeted regions such as the olfactory region showed negligible deposition, thus the spray particle conditions are ineffective for olfactory deposition for possible drug delivery to the brain.

- This study has produced the new deposition profiles for polydisperse particles. While a large set of parameters were evaluated (e.g. 15 particle size distributions, 3 breathing profiles, 4 regional deposition locations = 180 combinations)

1.4   Journal Papers

The following journal papers have arisen from the material presented in this thesis.

- Bates AJ, Doorly DJ, Cetto R, Calmet H, Gambaruto AM, Tolley NS, Houzeaux G, Schroter RC. Dynamics of airflow in a short inhalation. Journal of the Royal Society Interface. 2015 Jan 6;12(102):20140880.

- Calmet H, Gambaruto AM, Bates AJ, Vázquez M, Houzeaux G, Doorly DJ. Large-scale CFD simulations of the transitional and turbulent regime for the large human airways during rapid inhalation. Computers in biology and medicine. 2016 Feb 1;69:166-80.

- Calmet H, Houzeaux G, Vázquez M, Eguzkitza B, Gambaruto AM, Bates AJ, Doorly DJ. Flow features and micro-particle deposition in a

human respiratory system during sniffing. Journal of Aerosol Science. 2018 Sep 1;123:171-84.

- Calmet H, Kleinstreuer C, Houzeaux G, Kolanjiyil AV, Lehmkuhl O, Olivares E, Vázquez M. Subject-variability effects on micron particle deposition in human nasal cavities. Journal of Aerosol Science. 2018 Jan 1;115:12-28.

- Calmet H, Inthavong K, Eguzkitza B, Lehmkuhl O, Houzeaux G, Vazquez M. Nasal sprayed particle deposition in a human nasal cavity under different inhalation conditions. PloS one. 2019;14(9).

Chapter 2

Methods

To simulate the flow in the large human airways, computational meshes of different sizes were generated based on a single realistic geometry derived from Computer Tomography images. The numerical simulations were carried out using an in-house finite element code, Alya [83]. In the following, descriptions of the geometry, the mesh, the fluid/particle solver and the boundary conditions are given.

2.1   Geometry

The three-dimensional computational model was reconstructed from a clinically acquired computed tomography scan of a 48-year-old male subject, retrospectively collected from a large hospital database. The scan was performed in the supine position and the resulting data set comprises of 912 images in the axial plane, with $1mm$ slice thickness and in-plane $0.65 \times 0.65mm$ pixel size. Further details of the subject and acquisition are provided by Bates et al. [84]. Local ethics committee approval and patient consent were obtained to use the data for the investigation. A consultant radiologist reported the nasal airways are clear and of normal appearance. The position of the tongue base and other soft tissues in the pharynx were deemed consistent with the patient being scanned in the supine position. The vocal cords were noted to have the appearance of being abducted, whereas the trachea was considered to be of normal dimensions, not demonstrating any abnormalities. The airway in the pharynx may be narrower than if the patient had been standing, but the geometry is within the normal range.

The preliminary surface definition, obtained from a process of semi automatic segmentation of the medical images, is of insufficient quality for direct use in numerical simulations. This is due to the limited resolution of the image stack together with the linear sub-pixel interpolation used in the segmentation, which results in an overly faceted and step-like surface representation. The resulting surface was then smoothed using Taubin's algorithm [85]. Surface mesh refinement was therefore performed, taking care that the refined surface definition lay within half a pixel size of the initial segmentation. Since this length scale is representative of the underlying uncertainty bounds, the resulting surface representation was deemed anatomically realistic and faithful to the medical data. A rigid-body reorientation to approximately align the posture to the Cartesian axes was performed as a final step to facilitate subsequent analysis.

2.2 Mesh

The mesh discretisation used for scientific computing and simulation of the passages of the upper human respiratory system must be of high quality. An unstructured mesh was employed, due to the complex shape of the computational domain, especially apparent within the elaborate passageways of the nasal cavity. Given the importance of a good spatial discretisation, details of the mesh generation and size characteristics are outlined in the following. The mesh generation software employed was ANSYS ICEM CFD (ANSYS Inc., USA) and the description relates to the use of this software.

The approach used employs an octree-based method to generate a fine resolution surface mesh of the computational domain. Since this mesh resolution is finer than the previous representation, surface smoothing is once again required to avoid local flat patches and maintain a smoothly varying representation. The surface smoothing was performed using successive Laplace smoothing [86] and aspect ratio (ratio of shortest to longest edge) smoothing [87] in order to avoid surface shrinkage.

The second stage of the meshing process is the generation of a volumetric mesh, for which the Delaunay method was employed. This yielded a tetrahedral volume mesh with a smooth cell transition ratio ($\sim$1.2) employed close to the boundary wall. Finally a multi-layer prism mesh was created to resolve the high velocity gradients at the wall, with a few pyramids needed to ensure the transition between the prism layer and tetrahedral mesh in the
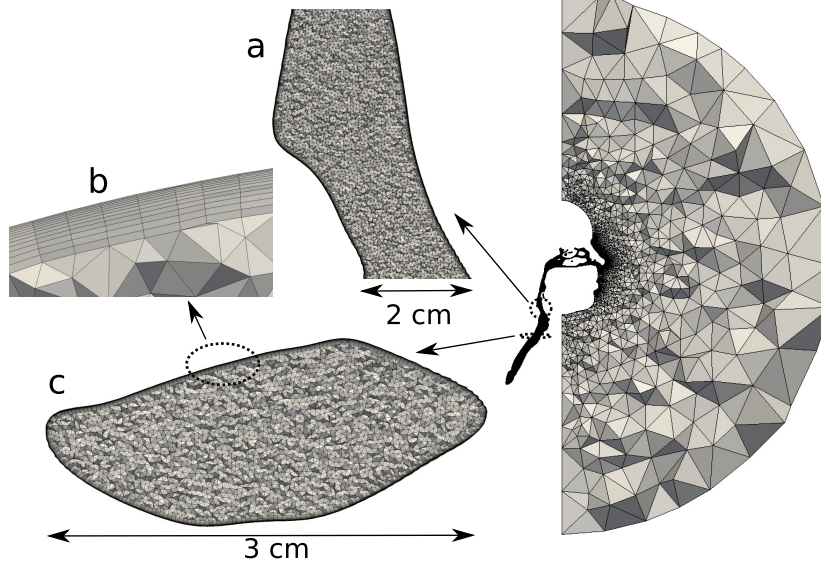
Figure 2.1: Sagittal view of upper airway mesh M2 (medium mesh) and details: (a) section in the sagittal plane above the glottis, (b) detail of prism layers, (c) section in the axial plane in the supra-glottic region.

core of the computational domain.

Three different mesh sizes were created with the parameters given in Table 2.1.

Mesh	$N_N(\times 10^6)$	$N_E(\times 10^6)$	$\Delta T(\mu s)$	$h(mm)$	$h_{bl1}(\mu m)$	N_{bl}	R_{bl}
M1 (coarse)	2	8	100	0.5	50	5	1.2
M2 (medium)	14	44	10	0.3	6	13	1.2
M3 (fine)	110	350	5	0.15	3	26	1.2

Table 2.1: Summary of different mesh resolutions and simulation parameters with N_N: number of nodes, N_E: number of elements, ΔT: time step, h: mean edge length of elements, h_{bl1}: height of the first element in the prism layer, N_{bl}: number of prism layers and R_{bl}: the prism growth ratio

The coarsest mesh (M1), with 8 million elements, was employed to obtain a general description of the flow field and the particle tracking result. The medium-sized mesh (M2), with 44 million elements, strikes a balance between

22

computational costs and accuracy of solution, and was used to provide the majority of airflow results presented in this study. The fine-sized mesh (M3), with 350 million elements, was used for the mesh convergence study then also to provide some results. More informations about computational limitation is given in Section 2.7

Examples of the medium mesh (M2) are presented in Fig. 2.1. For mesh M2, a minimum element height of 6 μm at the wall in used for the most critical region (just above the glottis, see Fig. 2.2), which corresponds to a value of $y^+ = \frac{u_* y}{\nu} = 0.5$ at the peak of the sniff inflow, where u_* is the friction velocity at the wall, y is the distance to the wall and ν is the local kinematic viscosity of the fluid . This value of y^+ can be considered to be sufficiently small for resolving the near-wall flow dynamics [88] and falls into the range defined by Piomelli and Balaras [89] that describes well resolved wall-layers. The mesh generation of the coarse and medium meshes M1 and M2 was achieved using the ANSYS ICEM CFD sofware. Mesh M2 took 3 hours to be generated, on a single Intel Xeon X5650 core. A total of 4 GB of RAM was used while meshing.

The finest mesh (M3) was produced using the Mesh Multiplication technique described in [90]. This technique consists in refining the mesh uniformly, recursively, on-the-fly and in parallel, inside the simulation code. For tetrahedra, hexahedra and prisms, each level multiplies the number of elements by eight, while a pyramid is divided into ten new elements. Mesh M3 was obtained using a one-level mesh multiplication from mesh M2, therefore obtaining approximately (due to the presence of pyramids) eight times more elements. The time to produce this multiplied mesh in parallel is almost negligible [90].

2.3   Fluid solver

It has to be mention that the numerical model described below in this section was used to produce all the results in Chapters 3, 4 and 5. Other numerical model was used for the drug delivery application Chapter.

Discretization method. We consider the incompressible Navier-Stokes equations, one of the physical modules of the Alya system [91], a high performance computational mechanics code developed at BSC-CNS. Let μ be the viscosity of the fluid, and ρ its constant density. The problem is stated as follows: find the velocity $\mathbf{u}$ and static pressure p in a domain Ω such that

they satisfy in a time interval

$$\rho\frac{\partial\mathbf{u}}{\partial t} + \rho(\mathbf{u}\cdot\nabla)\mathbf{u} - \nabla\cdot[2\mu\boldsymbol{\varepsilon}(\mathbf{u})] + \nabla p = 0, \tag{2.1}$$

$$\nabla\cdot\mathbf{u} = 0, \tag{2.2}$$

together with initial and boundary conditions. The velocity strain rate is $\boldsymbol{\varepsilon}(\mathbf{u}) = \frac{1}{2}(\nabla\mathbf{u} + \nabla\mathbf{u}^t)$.

The numerical model to solve these equations is based on a stabilized finite element method. The stabilization is based on the Variational MultiScale method which is considered as an implicit Large Eddy Simulation method [92]. The formulation is obtained by splitting the unknowns into grid scale and subgrid scale components. In the present formulation of Alya, the subgrid scale is, in addition, tracked in time and in space, thereby giving more accuracy and more stability to the numerical model [93].

Algebraic solver. The discretization of the Navier-Stokes equations yields a coupled algebraic system to be solved at each linearization step within a time loop. The resulting system is split to solve the momentum and continuity equations independently. This is achieved by applying an iterative strategy to solve for the Schur complement of the pressure. According to our scheme, at each linearization step it is necessary to solve the momentum and continuity equation twice. This split strategy is described and validated in [94].

The momentum equation algebraic system is solved using the GMRES method, with a simple diagonal preconditioner with a relatively low Krylov dimension. Usually, convergence is obtained in tens of iterations. The continuity equations is solved using the Deflated Conjugate Gradient (DCG) method [95], together with a linelet preconditioner to accelerate the convergence in the boundary layers [96].

Parallelization. The Alya code is written in Fortran90/95 and parallelized with MPI. The partition of the mesh is carried out on-the-fly with the METIS library [97]. The time for the partition is only a few seconds, even for mesh M3, for which the mesh multiplication is performed after the partition.

The fluid solver consists mainly of two basic steps, the assembly of the matrix and the right hand side of the Navier-Stokes system, and the solution of this system using the iterative solvers described previously. The assembly step does not require any communication, and its speedup is directly related

24

to the load balance provided by METIS. The MPI exchanges in the iterative solvers are carried out in an asynchronous way, enabling to overlap work and communication during the matrix-vector products. The parallelization of the DCG solver is based on MPI gather functions, as extensively described in [95]. Finally, parallel I/O is achieved using the HDF5 [98] and MPI-IO libraries [99] in order to postprocess the velocities and pressure on the mesh. In addition, filtering strategies enable to postprocess these variables on reduced portions of the mesh or to track single point values at each time step. These filtering techniques are necessary to reduce the amount of stored data and accelerate their visualizations.

2.4 Particle solver

Particles and fluid are solved in Alya. One-way coupling is used, i.e particles are transported after the solution of the fluid although the particles will not influence the fluid properties. The parallelization scheme for particle is radically different than that of the fluid, which can lead to important miss balance. In [100] we deeply describe both the implementation method and the strategy to avoid bottlenecks.

The transport of particles is simulated in a Lagrangian frame of reference, following each particle individually. From the numerical point of view, the main assumptions to develop the model are:

- Particles are assumed sufficiently small to neglect their effect on the air: therefore, a one way coupling is considered;

- Particles do not interact with each other;

- Particle rotation is neglected;

- Thermophoretic forces are neglected;

- The forces considered are: drag $\boldsymbol{F}_d$, gravitational and buoyancy $\boldsymbol{F}_g$;

Let $\mathbf{x}_p$, $\mathbf{u}_p$, $\boldsymbol{a}_p$ be the dynamical variables of particle p, namely the position, velocity and acceleration, respectively. Let m_p be its mass, ρ_p its density, d_p its diameter, and V_p its volume. Particles are transported solving Newton's second law, and by applying the series of forces mentioned previously:

$$\boldsymbol{a}_p = (\boldsymbol{F}_d + \boldsymbol{F}_g)/m_p. \tag{2.3}$$

The equation for the drag force assumes the particle has reached its terminal velocity and is given by

$$\boldsymbol{F}_d = -\frac{\pi}{8}\mu d_p C_d \mathrm{Re}_\mathrm{p}(\mathbf{u}_p - \mathbf{u}), \tag{2.4}$$

where Re_p is the particle Reynolds number involving its relative velocity with the fluid:

$$\mathrm{Re}_\mathrm{p} = \frac{|\mathbf{u}_p - \mathbf{u}|d_p}{\nu}.$$

The drag coefficient is given by Ganser's formula [101]:

$$
\begin{aligned}
C_d &= \frac{24}{\mathrm{Re}_\mathrm{p}\, k_1}(1 + 0.1118(\mathrm{Re}\, k_1 k_2)^{0.6567}) + 0.4305\frac{k_2}{1 + 3305/(\mathrm{Re}\, k_1 k_2)}, \\
k_1 &= \frac{3}{1 + 2\psi^{-0.5}}, \\
k_2 &= 10^{1.84148(-\log_{10}(\psi))^{0.5743}}, \\
\psi &= \text{sphericity}, \; (= 1 \text{ for a sphere}).
\end{aligned}
$$

The gravity and buoyancy forces contribute to the dynamic of the particle whenever there exist a density difference:

$$\boldsymbol{F}_g = V_p \boldsymbol{g}(\rho_p - \rho),$$

with $\boldsymbol{g}$ being the gravity vector.

Time integration.

Let us assume the particle path must be computed from time step n to the next one $n + 1$, where the time step size is defined as $\delta t := t^{n+1} - t^n$.

The time integration to actualize the particle dynamics at the new time step $n + 1$ is based on the Newmark method. This method is quite general in the sense that given the acceleration at time steps n and $n + 1$, one can obtain the velocity and position at the new time step $n + 1$ in an explicit form, using $\mathbf{a}_p^n$, or implicit form using a linear combination between $\boldsymbol{a}^n$ and $\mathbf{a}_p^{n+1}$. The switch between these possibilities are two parameters, namely β and γ which thus enable to control the accuracy and stability of the method.

Given the accelaration computed at time step $n + 1$, the scheme consists in solving the following equations:

$$
\begin{aligned}
\mathbf{a}_p^{n+1} &= \mathbf{F}^{n+1}/m_p, \\
\mathbf{u}_p^{n+1} &= \mathbf{u}_p^n + \delta t(\gamma \mathbf{a}_p^{n+1} + (1 - \gamma)\mathbf{a}_p^n), \\
\mathbf{x}_p^{n+1} &= \mathbf{x}_p^n + \mathbf{u}^n \delta t + \frac{1}{2}\delta t^2(2\beta \mathbf{a}_p^{n+1} + (1 - 2\beta)\mathbf{a}_p^n).
\end{aligned}
$$

The drag force given by Equation 2.4 depends on the relative velocity of the particle with respect to the fluid at $n + 1$, and therefore to the position of the particle at the new time step. For robustness purpose, we apply a Newton-Raphson scheme to converge the non-linearity in velocity, but not in position. Once the velocity is obtained, the position is updated. In order to gain additional control on the particle path, an adaptive time step strategy is adopted. The strategy is based on an error estimation of the Newmark-scheme.

Numerical implementation

The particle transport computation can be carried out in both a single-code or multi-code version. In the latter case, particles are transported using the same code and MPI partition as the fluid; in the last case, two instances of the code are used to enable asynchronism. The parallelization is hybrid, based on MPI+OpenMP, together with a dynamic load balance mechanism, as particle are likely to be located in very few MPI processes. The parallel strategy is extensively described in [102].

2.5 Boundary conditions

The computational domain is extensive and comprises, in order of inspired flow direction, a hemisphere of the subject's face exterior, followed by the bilateral nasal passages, through to the pharynx, larynx, trachea and down to the third branch generation in the lungs, as shown in Fig. 2.1 and 2.2. A no-slip boundary condition is imposed on the passage walls and the flat surface of the external hemisphere.

Inflow condition. The inflow velocity is imposed as a Dirichlet condition on the hemisphere dome. It is prescribed as a time varying uniform velocity with direction normal to the hemisphere. The radius of the hemisphere is $0.5m$. It was chosen to be large enough to avoid the inlet boundary conditions affecting the flow field within the airways on expiration ($0.3m$ and $1m$ were

(a)

(b)

(c)
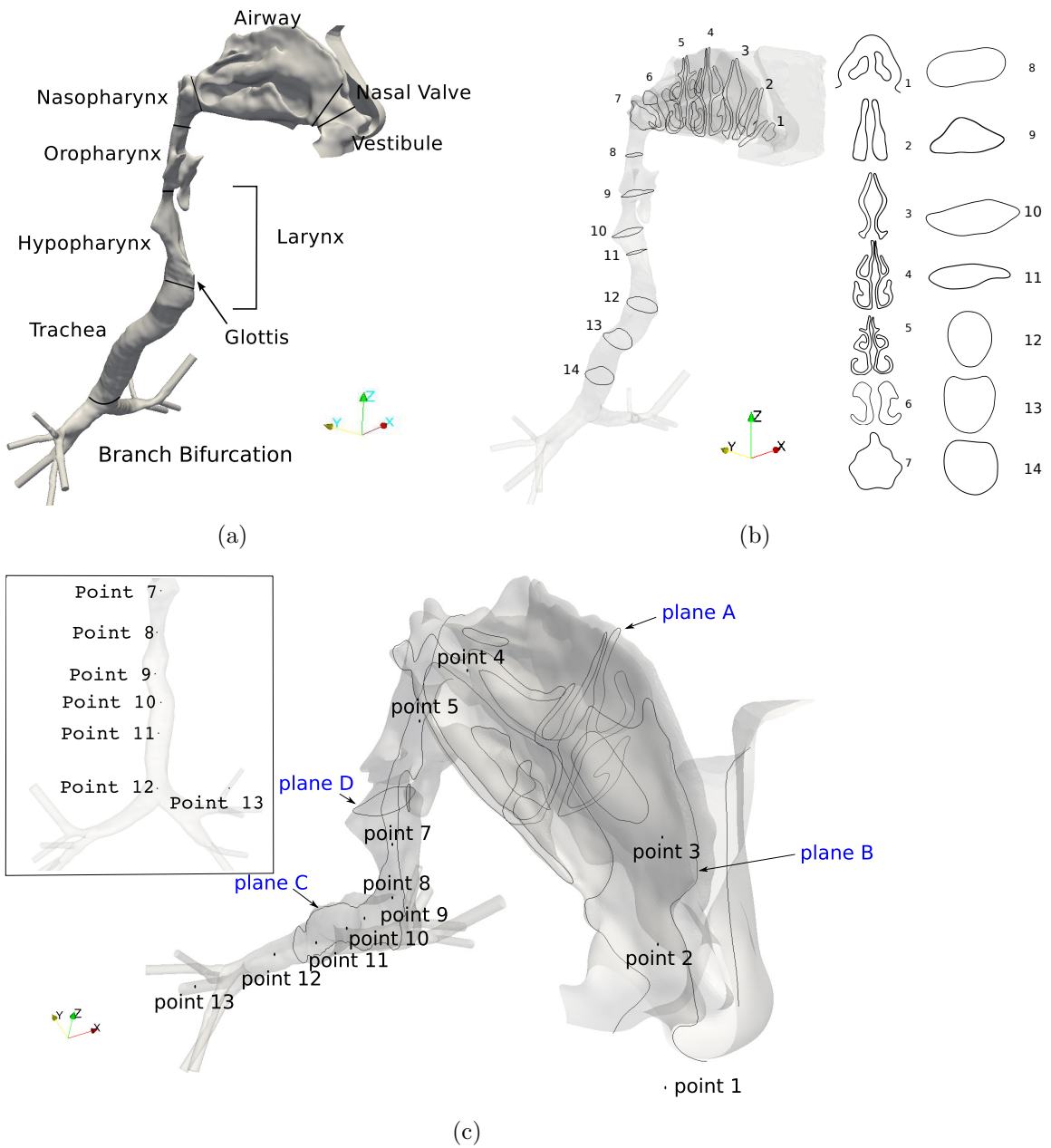
Figure 2.2: (a) Nomenclature of the approximate regions of the upper airways. (b) Location of different slices along the airways. (c) Locations of sections and points used as measurement locations for the results. Point coordinates are given in the appendix, see table 7.1. Plane A and slice 3 are the same.

28
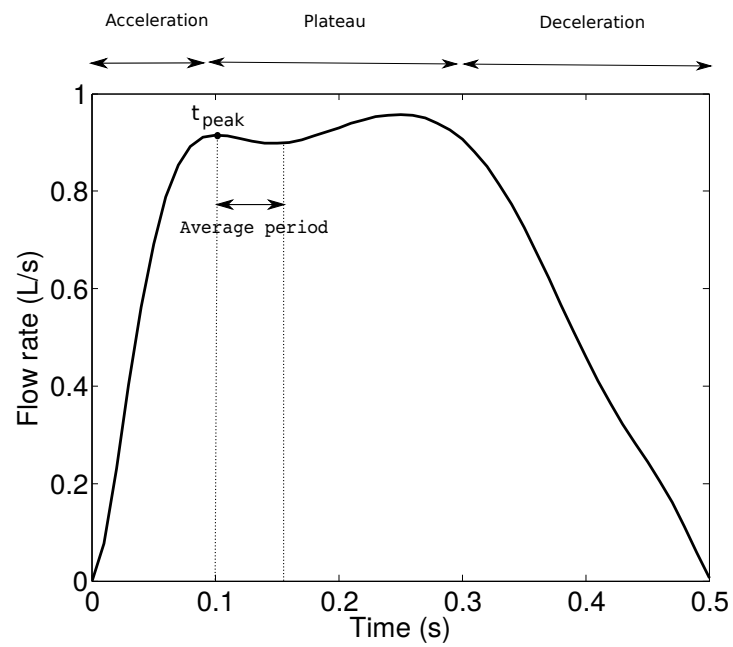
Figure 2.3: Flow rate profiles and average period, The 10th order polynomial function is given in the appendix see Eq.2.5 and Table7.2.

also tested). Consequently, for inspiration this hemisphere size is considered to be sufficient. To model the sniff, we use a polynomial function of order 10 derived from the experimental work detailed in Rennie and al. [103], in which several short inhalations from rest as initial conditions were measured for different subjects. The 10th order polynomial function (see Eq. 2.5) describing the temporal evolution of the flow rate is provided in Fig. 2.3, with the coefficients of the flow defining equation 2.5 are referenced in the appendix section.

$$P(x) = \sum_{i=0}^{10} C_i x^i \times 1.74 \qquad (2.5)$$

Particle injectors were located at each nostril at slice 1, see Fig. 2.2 and particles were distributed uniformly at the slice. Four different particle sizes, i.e., d_p=1, 5, 10, 20 μm were considered. 12,500 particles for each size were released at the initial time and re-injected every 0.05 s until the last injection time (0.45s) thus a total of 9 times during the sniff period. The total number of released particles during the entire simulation was 450,000. 20,000 suspended particles were present in the domain at the end of the simulation, which represents less than 1% of the relative error for each particle size considering the total deposition result. The initial velocities of particles were assumed to be the same as the airflow velocity at the nostril. Once the particle have crossed an outlet boundary element, the particle is out of the computational domain and removed from the simulation. Furthermore particles are deposited as soon as they get in contact with wall boundaries.

We consider deposition efficiency as the ratio of particles deposited on a given surface with respect to the number of injected particles. Based on previous studies ([104, 48]) and convergence tests, the number of particles of each size released at each time (12,500) is above the number necessary to ensure deposition results which are independent of the number released.

Outflow condition. A zero-traction outflow condition is imposed as a Neumann condition (the surface is free from external stress) at the third bronchial branch. In order to ensure fully developed flow at the outflow sections, the final bronchial branches were extruded to constant cross-sectional pipes for several diameters. These bronchial branches are set to have the 5 last layers of elements with higher constant viscosity to reduce turbulence and thus to avoid entrant flow that would unstabilize the solution.

2.6 Model validation

2.6.1 Analysis of grid convergence

The mesh convergence study was performed by time averaging the velocity magnitude profile at a location in the trachea. The time average was taken over the period shown in Fig. 2.3, during the plateau phase [0.1-0.13 s].The velocity profile is shown over a line extending from the anterior to posterior along the middle of slice 11, defined in Fig. 2.2b.
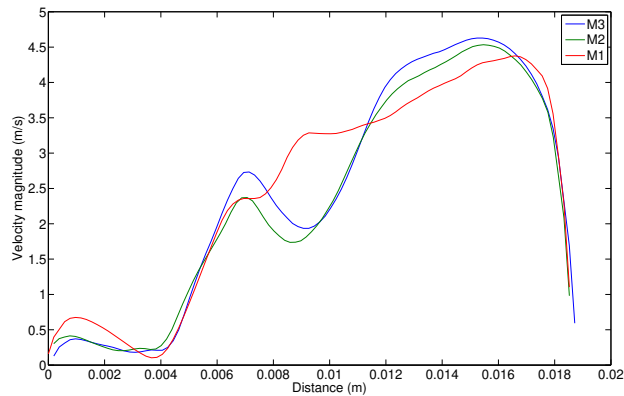
Figure 2.4: Time average velocity magnitude profile with different mesh resolution at the sagittal plane on the slice 11, see Fig. 2.2b.

The profiles look very similar for the medium mesh (M2) and the fine mesh (M3), although some discrepancies are still visible for the two higher grid sizes. For reasons explained in the next section, the medium mesh was used to provide the majority of results presented in this study.

2.6.2 Particle deposition

Particle deposition in the nasal cavity was compared to experimental data reported by [105, 106] and numerical data [107, 108, 104] (see Fig. 2.5) where the flow rate used for the comparison was a constant 20L/min. In order to standardize the results, the inertial parameter (IP) was used, i.e.

$$IP = d_p^2 \cdot Q \tag{2.6}$$

31

where d_p is the particle aerodynamic diameter (i.e. $1g/cm^3$) and Q is the volumetric flow rate. Fig. 2.5 shows good agreement between the simulation performed by the present code (Alya) and the numerical results of [107, 108, 104]. Differences in deposition results are due to the coarser airway surfaces in the replica producing higher deposition efficiencies than the numerical model, already observed frequently in literature, see [109, 110] who provide an extended study which can be summarized as the "wall roughness region enhanced particle capturing effect" or other study [111] who compared deposition of different level of surface roughness replicas (see Fig. 2.5 Model A,B,C) from [105] with LES simulations.
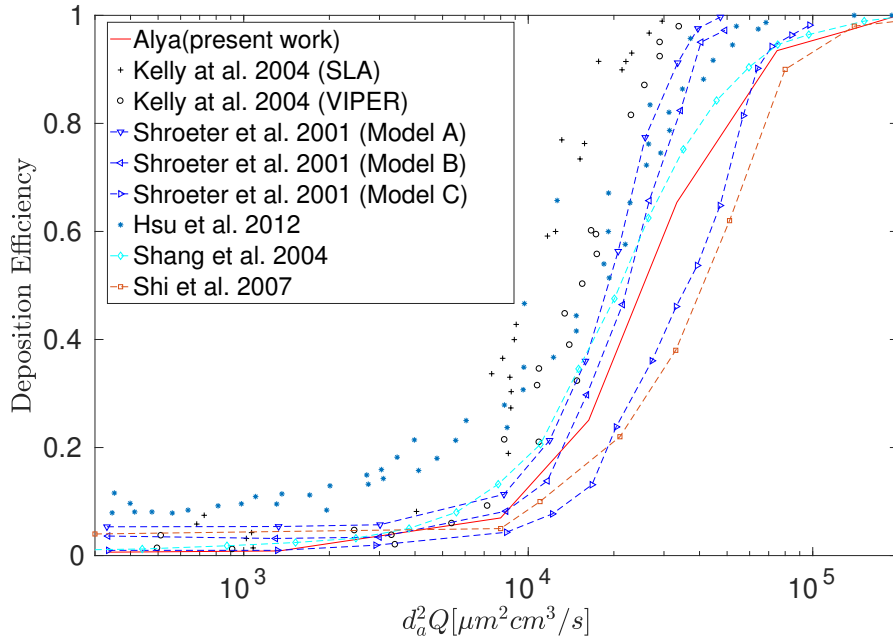
Figure 2.5: Micro particle deposition efficiency comparison between simulation and experiments.

The particle deposition efficiency is defined as:

$$\eta_{dep} = \frac{N_{dep}}{N_{in}} \tag{2.7}$$

where N_{dep} is the number of particles deposited on the surface area of interest, which can be the total respiratory tract wall or local surface areas,

e.g., olfactory regions, and N_{in} is the total number of particles released at the nostrils.

2.7   Computational resources

The simulations were carried out on the MareNostrum supercomputer, hosted by the Barcelona Supercomputing Center, and on the Fermi supercomputer, hosted by Cineca. For example, to carry out the simulation for the medium mesh M2 on the MareNostrum, 50000 time-steps are required on 1456 cores requiring approximately 200 hours. On the Fermi supercomputer, 16384 cores were used. Usually, in order to keep a good parallel efficiency, between 20000 and 40000 elements are used on each core. This makes the RAM requirement of the simulation very low under the possibilities of the computational nodes of the supercomputers used in this work.

In order to clarify the computational limitation aspect of this thesis, it has to be stated that the airflow results (Chapters 3 and 4) were done with M2 and M3 meshes. Thank to a computational grant from PRACE: project Pra04 693 (2011050693 to the Fourth PRACE regular call) we were able to present results using the medium-sized mesh M2, except for the sniff beginning [0.0–0.13 s], where the M3 was used. Then one year later without computational grant we carried out the particle tracking results (Chapter 5) with M1 mesh due to the computational cost.

Moreover for drug delivery application chapter we truncated the geometry removing the throat part and used a new mesh resolution between M1 and M2 resolution grid size, see futher informations in Chapter 6.

Furthermore using the in-house code Alya system which is permanently on progress, we used for Chapters 3, 4, 5 the numerical strategy implicit Large Eddy Simulation method. Then for Chapter 6, explicit Large Eddy Simulation method was used.

Chapter 3

Airflow features results

This chapter aims to provide the basic information necessary to understand the flow features happening in the human respiratory tract under sniff condition. In the interest of the reader, the results of this chapter are presented as a journey through the human airway.

3.1 Laminar to transitional flow in nasal cavity

Monitoring the local Reynolds number along the tract gives information on the flow regime. The local Reynolds number was calculated based on the area-average velocity and hydraulic diameter of each slice as [112]. The flow rate used to compute the Reynolds number was the peak value of the sniff function, $Q_{peak} = 0.9Ls^{-1}$ coresponding to $t_{peak} = 0.1s$, see Fig. 3.1.

To confirm if the flow is laminar, transitional or turbulent, the value of the local Reynolds number is not sufficient, in complex geometry and/or complex inflow, additional information is needed. A detailed analysis of the spectra is required to state the character of the flow: laminar/transitional/turbulent.

The values of the first slices close to the nasal valve (slice 1,2) belong to the range from laminar to turbulent regime, which indicate a possible transitional flow. While the slices crossing the turbinate region (slice 3,4,5) indicate a possible laminar flow.

Transitional regime can be observed in one of two ways; one is the visual analysis of flow temporal evolution [27], another is the local spectral analysis where the decomposition of the local velocity with time series Fourier
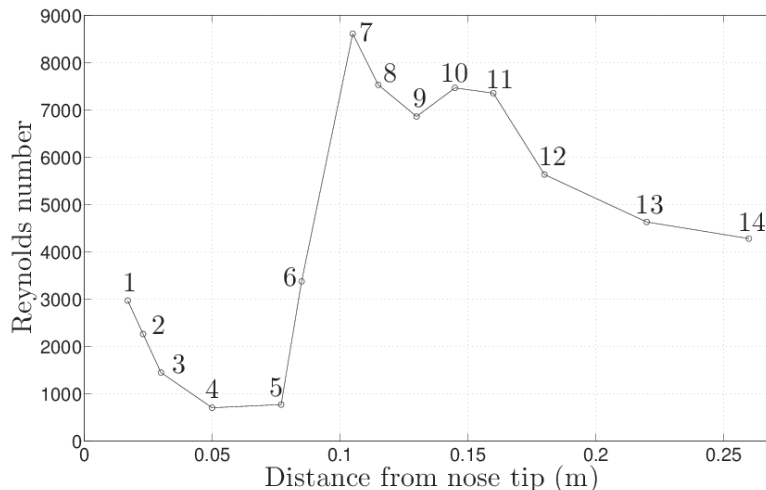
Figure 3.1: Cross-sectional-area-average Reynolds number as a function of distance from nose tip. The number positions refer to the different slices see Fig.2.2.

produces some clear harmonic peaks in the low frequency ranges [113].

In [6], the authors demonstrated that the flow in the nasal cavity is unsteady downstream of the nasal valve. A key feature of this unsteady flow is the vortex shedding and flapping motion of the shear layer, located on the boundary between the nasal valve jet and the superior separated flow region. Spectral analysis of these large-scale motions can provide relevant information.

A one-dimensional spectral analysis that considers all components of the velocity fluctuation is computed for the time period [0.1-0.15 s], which we recall is the start of the plateau phase of the sniff waveform. All the details concerning the spectral analysis and parameters are provided later in the next section.

Fig. 3.2 is the normalized energy spectrum of local velocity fluctuations at the point 3 (see Fig. 2.2), located within the right-nasal cavity and a closer view of the interest zone where the harmonic peaks are observed.

With the unsteady features observed in the literature, numerically by [6] and experimentally by [27] the presence of the harmonic peaks are observed. Here transitional flow can be considered.

Further downstream of the nasal valve, the values of the local Reynolds
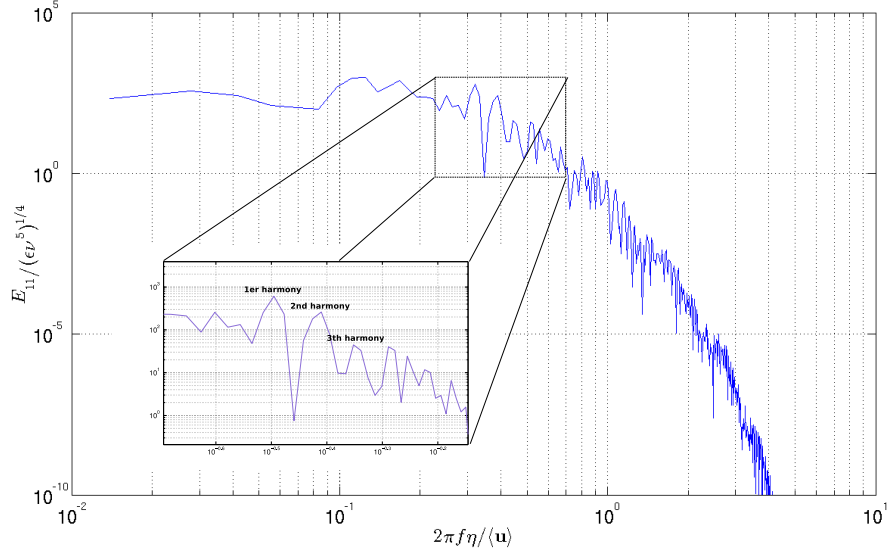
Figure 3.2: Normalized energy spectrum of velocity fluctuations at the location point 3, see Fig. 2.2 and detail view of the interest zone.

number (slices 3,4,5) show a laminar regime along the nasal turbinate region. This tendency is also observed into this section by [112].

To outline the airflow field in the nasal cavity, the inlet flow entering in the nostril changes drastically in the direction of the nasal valve, going from vertical to horizontal where the diameter is reduced. This complex geometry produces some specific features and unsteady phenomena, see Fig. 3.2. Then, most of the inhaled air flows through the wider middle-to-low portion of the main passageway, which is free of obstacles.

Further, where left and right cavities join with different velocities begins the nasopharynx.

3.2 Transitional to turbulent flow in the nasopharynx

The nasopharynx is a region where the confluence of different outflow velocities of the left and right cavities mix together. Fig. 3.3 shows the complexity of this particular flow, where two different airflows join into a significant
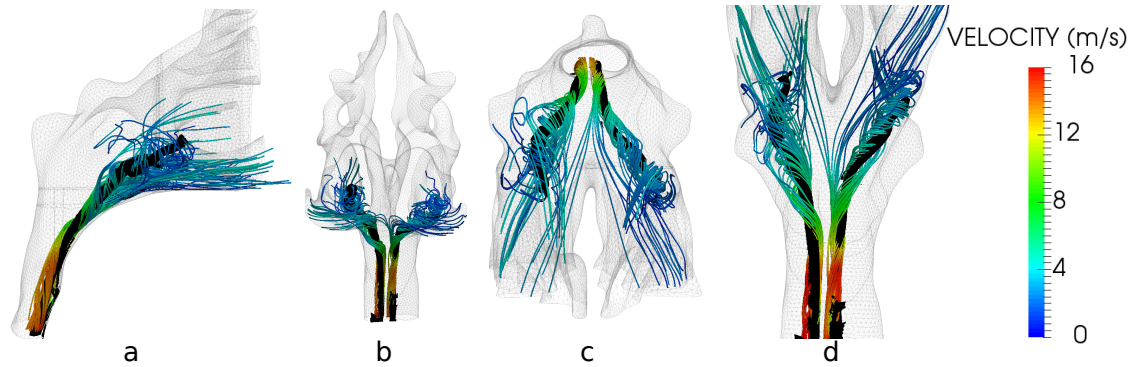
Figure 3.3: Streamlines colored by velocity magnitude and black iso-surface of Q-criterion of different views of the nasopharynx at $t_{peak} = 0.1$s. (a) Lateral view. (b) Front view. (c) Top view. (d) Down isometric view.

curvature.

Fig. 3.3 shows streamlines colored by velocity magnitude and iso-surface of Q-criterion of different views of the nasopharynx at $t_{peak} = 0.1$s. Here vortex identification is represented by Q-criterion which is defined by [114].

$$Q_{crit} = \frac{1}{2}(||\bar{\Omega}||^2 - ||\bar{S}||^2) > 0 \tag{3.1}$$

where, S and Ω are, respectively, the symmetric (strain and shear) and antisymmetric (rotation) components of the velocity gradient. When the Q-criterion is positive, it represents locations in the flow where the rotation Ω dominates the strain and shear S. Dean vortices [115] are observed, resulting from the curved passage undergoing an almost 90 ° bend from the the horizontal nasal passage to the vertical descending sections. Only two main symmetric swirling vortices are represented, although the flow in the nasopharynx is more complex than these two vortical structures.

These two symmetric swirling vortices are located at the inferior part of the nasopharynx, called the soft palate, the symmetric location and their strengths are identical. Further down the velocity jumps by a factor 4 at the end of nasopharynx due to sharp flow area reduction in the passage. Furthermore, the presence of Dean vortices can include events leading to transition to turbulent flow [115].

The value of the local Reynolds number for the slice 6 in Fig. 3.1 indicates possible transitional flow while the values for the slice 7 and 8 are turbulent.

Wilcox defined the turbulence intensity as an turbulence indicator for internal flow [116],

$$I_{turb} = \sqrt{\frac{2TKE}{3U^2}} \qquad (3.2)$$

where TKE is the turbulence kinetic energy and U is the area-average velocity. Fig. 3.4 is the Cross-sectional-area-average of turbulence intensity calculated with the area-average of TKE and the area-average velocity of each slice during the plateau phase of [0.1-0.15 s], see Fig. 2.2.

In the nasopharynx section (slice 7 and 8), the values of the turbulence intensity is above 7%, describing transitional-turbulent flow. This can be observed in the appendix section where the cross sections of TKE are displayed (see Fig. 7.1). High values are observed for the slices 7 and 8.

We can remark from Fig. 3.4 that the turbulence intensity in the nasal cavity (slice 1 to 6) is unexpectedly significant, between 5% to 10%. This is due to the high values of Reynolds stresses, produced by oscillations of the flow in nasal cavity. This complex geometry promotes the unsteady flow but the calculation of the turbulence intensity is not accurate for this particular case. In Section 3.1, it is demonstraded than the flow in the nasal cavity is laminar-transitional but not turbulent. Therefore, in Fig. 7.1, low values of TKE in the nasal cavity are observed.

Due to the high level of fluctuations produced by the laryngeal jet [6, 84], it can observed that the state of the laryngeal section (the throat) is clearly turbulent, see Fig. 3.4, with 2 peaks (slice 10 and 12).

3.3 Turbulent flow in the laryngeal region

Fig. 3.5 qualitatively illustrates the location of the turbulence vortical structures in the pharyngolaryngeal region. We clearly observe a transition of the vortex structures direction, initially tendentially aligned with the flow direction in the nasopharynx region, while further downstream in the larynx the flow turbulence has undergone a cascade from larger to smaller structures which are now aligned largely transversally to the flow direction. The vortices aligned with the flow direction in the nasopharynx, Dean vortices, are described in Section 3.2.

From Fig. 3.5 we can visually identify the source of instabilities and production of turbulence structures. At the nasopharynx downstream there
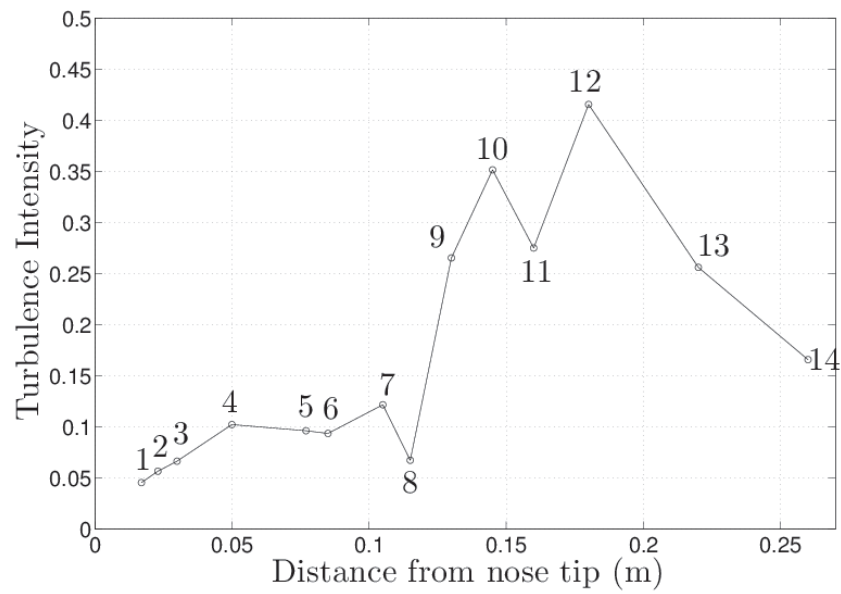
Figure 3.4: Cross-sectional-area-average turbulence intensity as a function of distance from nose tip. The number positions refer to the different slices described in Fig. 2.2.
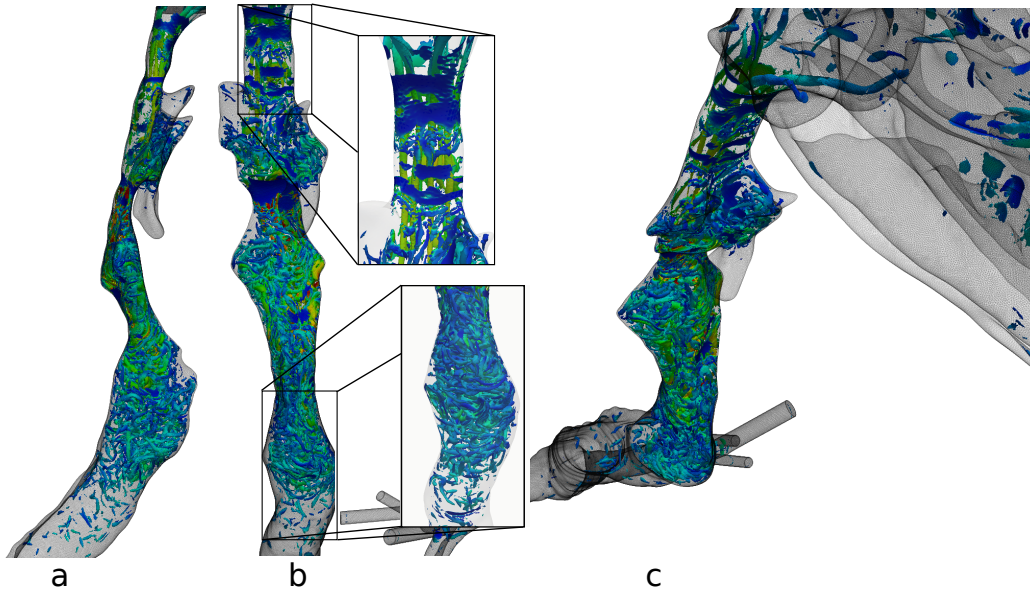
Figure 3.5: Iso-surface of the Q-criterion (value=4.5×10^5) in the pharyngola-ryngeal region at $t_{peak} = 0.1s$. (a) Lateral view. (b) Front view. (c) Isometric view.

is a severe stenosis that forms a jet with longitudinal vortical structures, which enters the oropharynx where there is a sudden expansion in the cross-sectional area of the passage. The fluid mechanics behaviour of free jets is that of Kelvin-Helmholtz instability, which occurs when there is a velocity difference across the interface between the higher velocity jet and the surrounding air. These instabilities promote a cascade from large vortex structures to smaller ones, resulting in a turbulent flow, see Fig. 3.4, slice 10. Again we observe a second stenosis at the downstream section of the oropharynx that is due to the subject lying in supine position and the tongue relaxing, reducing the patency of the passage. After this stenosis there is again a change in anatomy geometry that promotes the gradients across shear layers and the production of turbulence, see Fig. 3.4, slice 12. As the flow moves downstream, by the time it reaches the trachea the turbulence structures have largely broken down and dissipated.

3.4 Summary

The purpose of this chapter was to explore and describe the main features of the dynamic and unsteady flow occurring in the large airway during a rapid and short inhalation.

Thanks to the use of a simulation code specially designed for large-scale computational resources, the numerical model presented was able to simulate all the flow regimes in different airway segments. The laminar to transitional regime in nasal cavity is demonstrated through spectral analysis. The flow distribution at a section of the nasal cavity gives an insightful overview of the intricate wall-bounded flow occurring. This includes the flow partitioning, which is effected by the nasal valve directing the flow far upstream as a jet, and the turbinate structures that project into the passages and divide the airspace, diverting the airflow to different regions of the cavity.

The main features present in the nasopharynx are highlighted, transitional to turbulent state happening in this region is discussed. The turbulent flow in the laryngeal region is described, illustrated by the complex configuration of vortical structures. This is the dominant site of turbulence production, more precisely located in the supra-glottic region. As the flow reaches the lower portion of the trachea, the turbulence intensity as greatly reduced, with few vortical structures identifiable.

In the next chapter, a detailed analysis of the airflow is presented. Analysis for pressure drop, mean flow, fluctuations, wall shear stress, energy flux, and energy spectral are exposed. Furthermore, deeper investigations about the transition regime are presented.

Chapter 4

Airflow variables results

A sniff is a short, transient and unsteady inspiration, defined by the flow rate imposed as detailed in Section 2.5. The flow rate profile of the sniff is shown in Fig. 2.3, and can be divided into three phases: the acceleration [0-0.1 s], the plateau [0.1-0.4 s] and the deceleration [0.4-0.5 s]. Each phase results in a distinct flow field, largely due to the resulting forces driving the inspiration. The acceleration phase is known to produce roll-up structures in the nasal cavity for a zero initial velocity [26], quickly establishing the bulk flow field due to the small cross-sectional passageways. Bates et al. [84] noted that nasal washout and stabilisation of nasal regional flow division occur within the first phase. The plateau phase is the most appropriate segment of the flow profile for the turbulence analysis as the velocity is approximately constant, and the time window is of sufficient duration to calculate turbulence statistics. The last phase is the deceleration, where breakup of flow structures and vortices begin to dominate. These are quickly suppressed in the nasal cavity due to the small patency of the passages. For more explanation of the three phases, see Bates et al. [84].

A time window during the plateau phase of [0.1-0.15 s] is chosen to compute the mean flow and the turbulence measures. This window was taken as sufficiently long due to the fine temporal resolution available, and sufficiently short to avoid large-scale transients to interfere with the analysis. Also, the right nasal cavity was focused on, due to interesting features, such as recirculation in the anterior nasal cavity, which was not present in the left cavity of this subject for this flow profile but has been reported in other studies [26, 117]. Unless otherwise stated, results are presented using the medium-sized mesh M2, except for the sniff beginning [0.0-0.13 s], where the
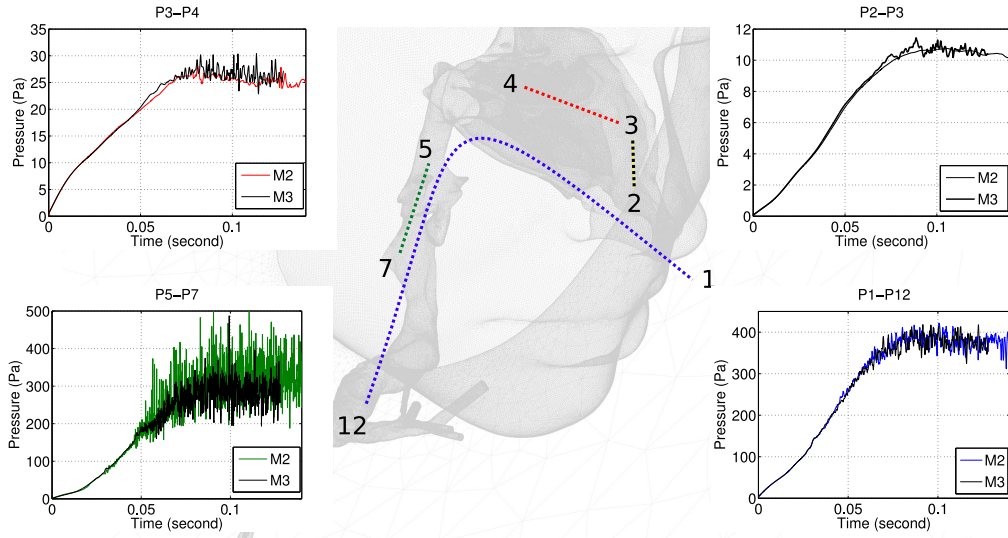
Figure 4.1: Static pressure drop across different compartments of the upper respiratory system during time period [0.0-0.13 s]. Comparison for mesh resolution M2 and M3 is shown.

M3 was used. This was due to temporary CPU usage limitations at the time of running the cases for this work, see Section 2.7.

4.1 Pressure drop

Physiologically, airflow through the respiratory system is driven by the pressure drop, Fig. 4.1 presents the static pressure drop across compartments of the airways. A comparison is made for the mesh resolution, M2 and M3. The results displayed are for the beginning of the sniff waveform, time period [0.0-0.13 s].

The pressure drops in Fig. 4.1 highlight the role of the different compartments in the upper respiratory system:

- The pressure drop across the anterior nasal valve (P2-P3), i.e: between before the anterior nasal valve (point 2) and after the anterior nasal valve (point 3), in the right cavity. The anterior nasal valve is the smallest cross section area in the vestibule.

- The pressure drop across the nasal cavity (P3-P4), i.e: between after

the nasal valve (point 3) and before the nasopharynx (point 4) in the right cavity. The nasal cavity is a very complex geometry with very thin cross sections. It is composed by three passageways, superior, middle and inferior meati.

- The pressure drop across the larynx (P5-P7), i.e: between the oropharynx (point 5) and after the larynx (point 7). This zone plays an important role in the turbulent flow in the descending airways.

- The overall pressure drop (P1-P12) i.e: between outside the nose (point 1) and the carina (at the first bifurcation of the lung) (point 12).

The values of pressure drop in Fig. 4.1 show clearly that the highest pressure loss occurs in the throat and not in the nose. The pressure drop across the anterior nasal valve (P2-P3) is less than across the nasal cavity (P3-P4), despite it being a narrower section.

Oscillations are observed for the fine mesh (M3) in the anterior nasal valve pressure drop trace. This indicates that a fine mesh resolution ($0.15mm$) is needed to capture features occurring in this region, as discussed later in Section 4.6. There are also higher amplitude of oscillations in the nasal cavity with the fine mesh solution, while in the remaining region the pressure drop appears sufficiently resolved. On the other hand in the larynx (P5-P7) there is a higher amplitude of oscillation and also a higher mean pressure drop value for the medium mesh (M2) compared to the fine one (M3).

The computed tomography (CT) scan is performed with the patient in the supine position. Gravity causes a collapse of the peripharyngeal tissues in the oropharynx, leading to a reduced patency; while in a standing posture the airspace in the larynx is greater. This observed collapse leads to the high pressure drop in the larynx (P5-P7).

4.2 Mean flow

The time window [0.1-0.15 s], used to compute the temporal mean velocity, is chosen as part of the plateau phase corresponding to the same time period for which the turbulence analysis is performed. The flow rate is approximately constant during this time period, and the mean velocity provides an overview of the dominant persistent flow features.
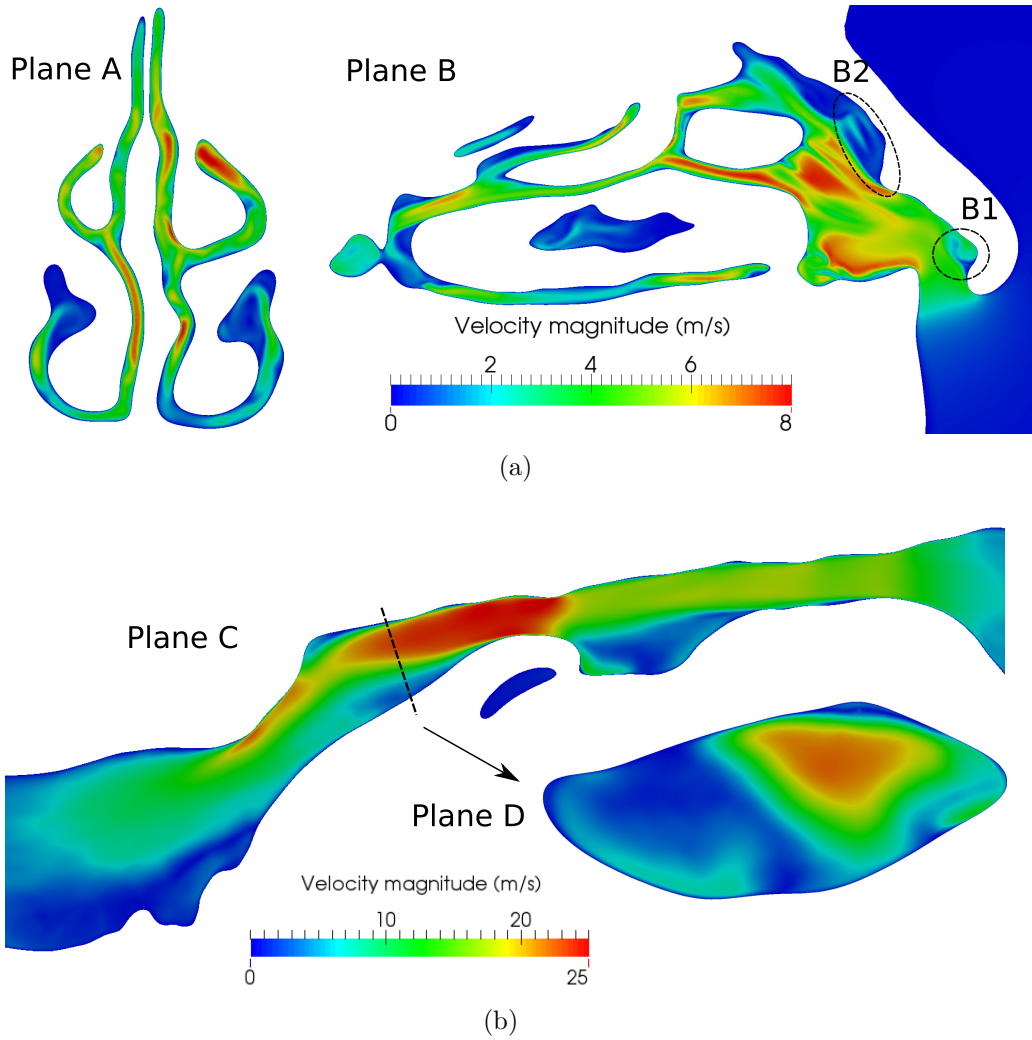
Figure 4.2: Mean velocity of cross-sections. (a) Coronal plane in the middle of nasal cavity (plane A) and sagittal plane of right nasal cavity (plane B) with the two recirculation zones. (b) Sagittal plane of laryngotracheal area (plane C) and a coronal plane of the supra-glottic region(plane D). (a) and (b) are computed for the time period [0.1-0.15 s] and the mean velocity scale is different to enhance the features in the nasal cavity and in the laryngotracheal area. See Fig. 2.2 for cross-section location.

45

Fig. 4.2 shows the mean velocity in four different cross sections of the airway, chosen to be approximate mid-passage locations. In the sagittal plane of the right nasal cavity (plane B) two recirculation areas are visible: the first is small and centred in the vestibule (B1), while the second is located in the upper anterior part of the nasal cavity (B2) and is both larger and more complex. The B2 recirculation region is caused by flow separation at the superior edge of the nasal valve. This feature has been observed in the literature, for instance in the experimental study of Doorly et al. [26] with the use of a high speed PIV setup, where it was stated that a shear layer that is generated on the boundary of the separation region, causes a transitional flow that is observed as periodic flapping (and will be discussed in greater detail in Section 4.6). The nasal valve has a small cross-sectional area and causes the flow to focus and form a jet that is directed towards the middle turbinate leading edge. A rapid change in geometry orthogonal to the jet direction occurs downstream of the nasal valve and is especially pronounced on the superior portion of the nasal valve. This superior portion is the thinnest section of the nasal valve [117], and is often related to corrective surgery to widen and increase the angle it forms.

The flow distribution in the nasal cavity can be observed by a coronal cross-section (see plane A), as this plane is perpendicular to the bulk flow direction. It is evident that the flow distribution between the bilateral passages is not the same due to evidently different passage shapes and patency. It can be observed however that the bulk of the flow inspired traverses the middle portion of the nasal cavity, leading to slow flow velocity in the lower meatuses despite their large dimensions. Higher flow rates are observed in the centrer-line of the septum and middle meatus passages. The olfactory region, located at the superior part of the nasal cavity, has a slower flow rate and is an indication that the transport phenomena are characterised by both advection and diffusion in this region. In comparison to slower flow rates however [26, 117], a sniff advects a larger volume of inspired air towards the olfactory cleft.

In the oropharynx region, there is another marked reduction in the passage cross-sectional area. This stenosis prompts a jet to be formed, as seen in planes C and D. This jet has also been reported in the literature where it has been referred to as the laryngeal jet [36, 118]. This jet persists a short distance downstream, as seen by a region of focused high magnitude velocity, and is broken down rapidly. The rapid breakdown is characterised by the short length and fast decrease with regard to the jet mean velocity, as
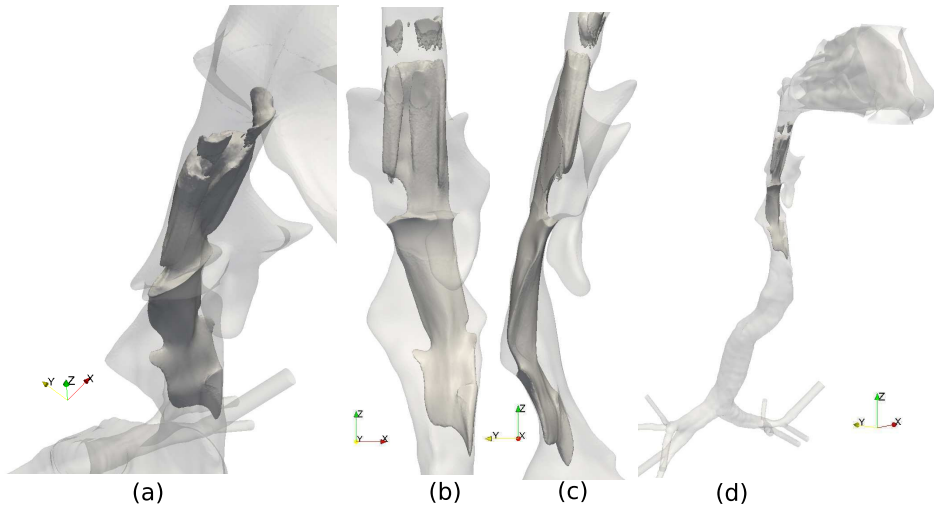
Figure 4.3: Different views of the laryngeal jet, given as the mean velocity iso-surface, computed for the time period [0.1-0.15 s]. (a) Top isometric view. (b) Front view. (c) Lateral view. (d) Isometric view.)

the flow passes the larynx and enters the trachea. This indicates noticeable temporal fluctuations (low mean values), as will be discussed later in Section 4.3. As the passage changes direction, the jet impinges on the posterior hypopharynx wall and causes a high wall-shear stress region (as shown in Fig. 4.6 for a single time instant), that together with the expanding passage area at the start of the trachea, promotes the jet breakup.

Iso-surfaces of mean velocity in the laryngotracheal region are shown in Fig. 4.3 and provides a three-dimensional representation of the laryngeal jet. Two vortex structures are also identifiable at the upstream region to the oropharynx stenosis, and are the result of Dean vortices formed by the passage 90 degree change in angle at the nasopharynx. From the front view of Fig. 4.3, it can be seen that the laryngeal jet is deviated downstream of the glottis, due to the sinuous geometry related to the posture of the subject during the scan.

Fig. 4.4 shows four different slices (described in Fig. 2.2) with the time average velocity $\langle \mathbf{u} \rangle$ and the instantaneous velocity $\mathbf{u}$. It is apparent that the mean velocity does not differ significantly from the time instant one within the nasal passages, however in the descending tract a noticeable difference is evident.

47
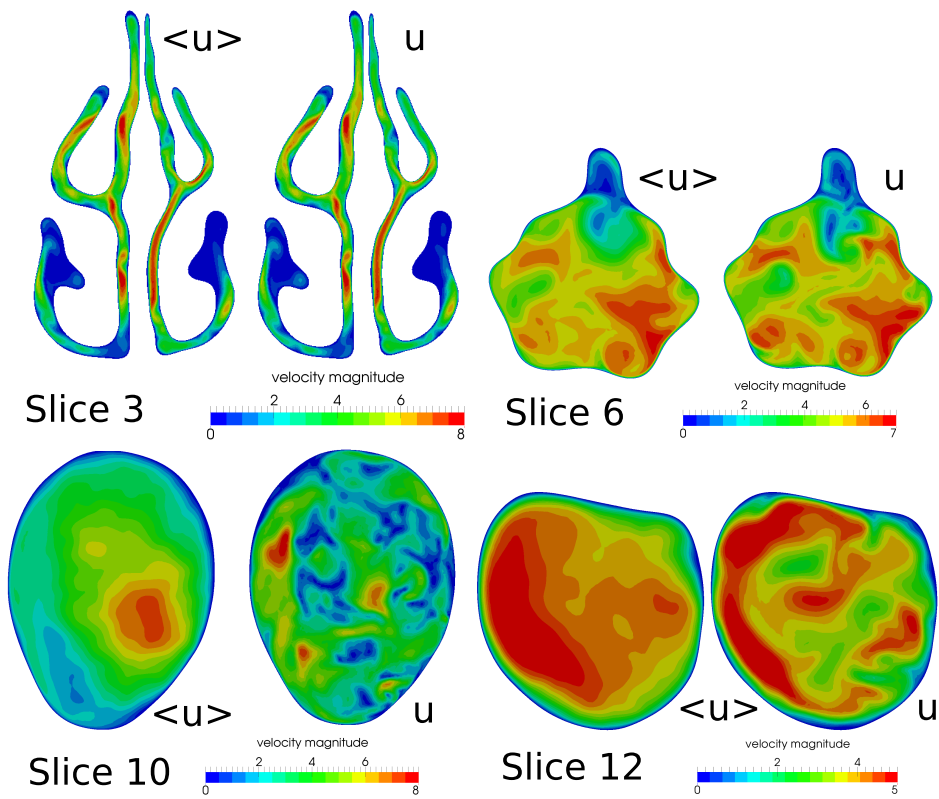
Figure 4.4: Different cross-sectional slices of the airways, referenced in Fig. 2.2, $\langle \mathbf{u} \rangle$ the time average velocity (computed for the time period [0.1-0.15 s]), and $\mathbf{u}$ the instantaneous velocity (0.15 s).

4.3 Fluctuations in the flow

Having outlined the flow features discernible from the mean flow field, we now turn our attention to the temporal fluctuations. The root mean squared velocity fluctuations vector is computed for each component of the velocity vector like $\mathbf{u}'_{rms} = \sqrt{\langle \mathbf{u}'^2 \rangle}$, for the time period [0.1-0.15 s]. The resulting vector magnitude, presented in Fig. 4.5 for some cross-sections of the flow field, can highlight the unsteady flow regions with respect to the mean flow.

An immediate result of the $\mathbf{u}'_{rms}$ is that in the nasal cavity, the magnitude of the fluctuations are one order of magnitude smaller than in the laryngeal region. Similar results have been reported in Zhao et al. [1], which noted that the airflow in the human nasal cavity even during sniffing is transitional or exhibits low intensity turbulence. Bates et al. [84] stated that, for the same subject used in the present study, the flow in the right nasal cavity is more unsteady than in the left nasal cavity. On comparing the cross-sections of mean and fluctuating velocity in the nasal cavity, shown respectively in Fig. 4.2 and 4.5, the regions of higher $\mathbf{u}'_{rms}$ do not correlate with the regions of higher mean velocity, but instead these regions occur at the edges of high velocity regions, indicating that the unsteadiness is caused by the breakdown of shear layers.

Conversely, in the laryngeal region cross-sections shown in Fig. 4.2 and 4.5, the regions of high $\mathbf{u}'_{rms}$ correspond to the shear layers located on the boundary of the laryngeal jet, indicating that in this region the fluctuations in the velocity are likely related to a high Reynolds number. The high values of $\mathbf{u}'_{rms}$ persist downstream of the laryngeal stenosis where the jet is initiated, into the trachea with decreasing magnitude and localization. These findings are related to the turbulent dissipation through smaller scales, which occurs rapidly in the laryngeal region due to the change in direction of the airway that forces the jet to impinge on the posterior glottis region, and thus favour vortex breakdown.

4.4 Wall-shear stress

The wall-shear stress is an important measure for the respiratory airways, being responsible to a large extent for the resistive forces during respiration, and related to exchange processes and the near-wall flow field [119]. In Fig. 4.6 the surface integrated wall-shear stress for different compartments
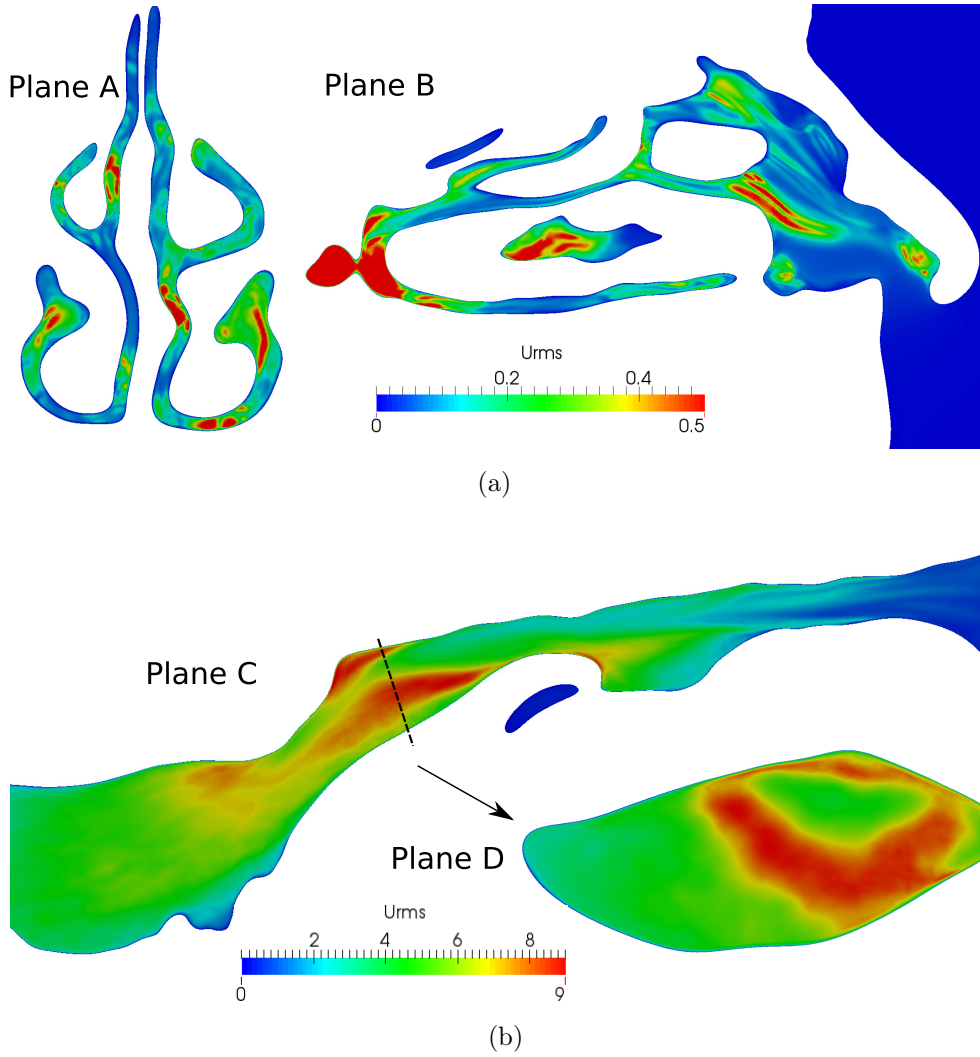
Figure 4.5: rms velocity fluctuations magnitude of a few cross-sections. (a) Coronal plane in the middle of nasal cavity (plane A) and sagittal plane of right nasal cavity (plane B). (b) Sagittal plane of laryngotracheal area (plane C) and a coronal plane of the supra-glottic region(plane D). (a) and (b) are computed for the time period [0.1-0.15 s] and the rms velocity fluctuations scale is different to enhance the features in the nasal cavity and in the laryngotracheal area. See Fig. 2.2 for cross-section location.

(a)

(b)

(c)

(d)
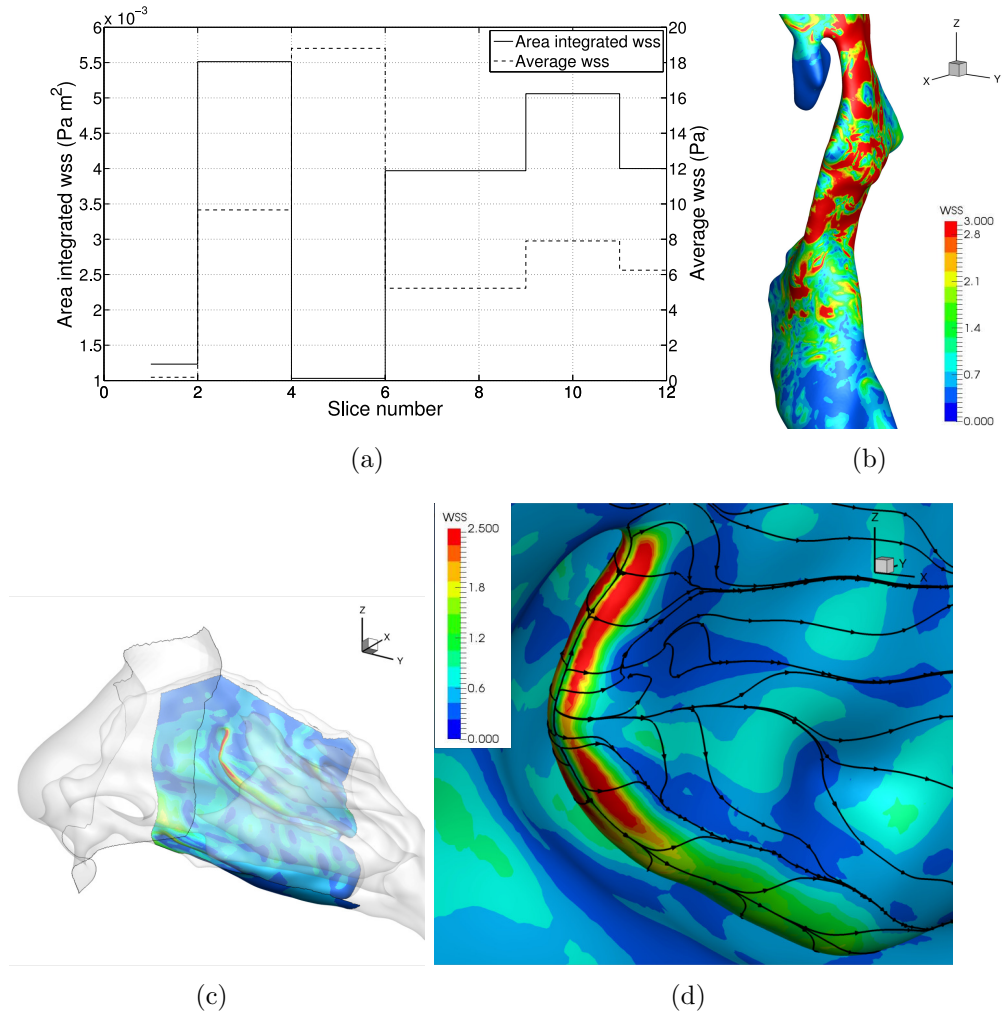
Figure 4.6: (a) The surface integrated wall-shear stress value over different sections on the left hand vertical axis and the average wall-shear stress (i.e. the surface integrated wall-shear stress divided by the considered area surface) on the right hand vertical axis (see Fig. 4.7). (b) Map of wall-shear stress magnitude in the hypopharynx and trachea (sections 8-11). (c) General view of map of wall-shear stress magnitude in the right nasal cavity mid-region. (d) Detail of the anterior protrusion of the right nasal cavity middle turbinate, with map of wall-shear stress magnitude and surface shear lines. All results correspond to results at the time t=0.15 s.

51

(see Fig. 2.2) of the airways are plotted. The thin and scroll-like form of the nasal cavities exposes the flow to a large wall surface area, such that despite having, in general, low wall-shear stress values, the integrated stress (between sections 2-4, see Fig. 4.7 for slice location map) is greater than the other regions. A large resistance also occurs between sections 9-12, which correspond to the passages of the hypopharynx and further downstream. However, in contrast, the wall-shear stress values in these regions are large and the wetted surface area is in comparison small. On the whole, compartmentalising the anatomy, the greatest resistance is reported between section 6-12, which corresponds to the descending airways from the oropharynx. The nasal valve (present between section 1-2) also causes considerable resistance due to the constriction.

The complex, undulating shape of the wall at the mid-region of the nasal cavity affects the flow by partitioning it into different regions. The undulations may also favour exposing core flow to the nasal lining, enhancing exchange processes between lining and the flow as well as deposition of suspended particles. The turbinates are important geometric features in the partitioning of the flow, and in Fig. 4.6 a detail of the anterior protrusion of the middle turbinate is shown, with the wall-shear stress magnitude and the surface shear lines (computed as integrated paths of the wall shear stress). As noted above in Section 4.2, the nasal valve forms a jet that is directed at the anterior protrusion of the middle turbinate, and as it impinges a stagnation line is clearly visible at the leading edge. Furthermore, the surface shear lines show that the flow is directed away on either side of this impingement line.

The wall-shear stress, surface shear lines, and consequently the near-wall flow field [119], vary smoothly in the nasal cavity. These findings are in contrast to the region of the hypopharynx where a bend in the conduit is present, and we observe a higher and disturbed wall-shear stress magnitude, as shown in Fig. 4.6. The impingement zone in the hypopharynx breaks down the flow, enhancing mixing and bringing the core flow in contact with the lining. This highly energetic zone of impingement and mixing may serve to enhance deposition of smaller particles still in suspension that were not filtered in the nasal cavity.
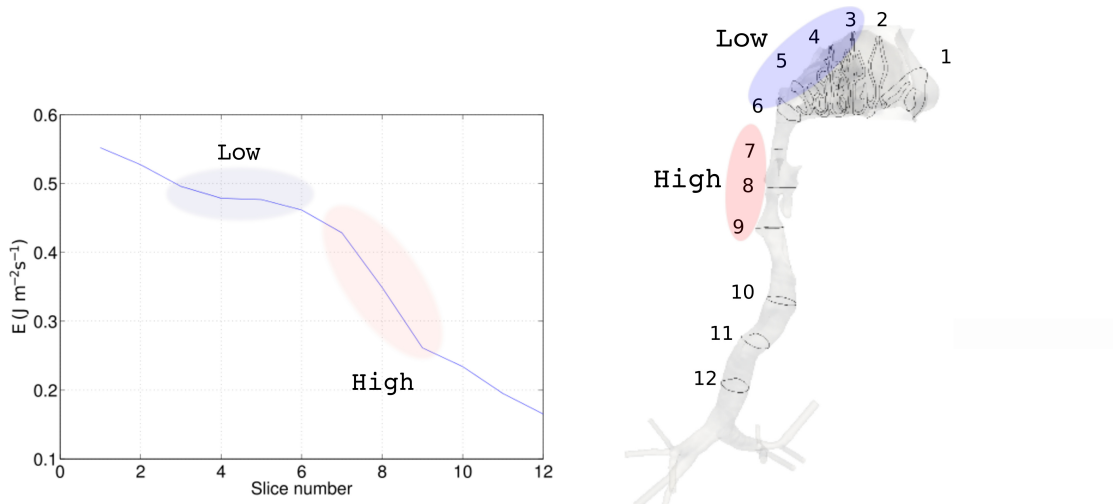
Figure 4.7: Energy flux computed at different sections along the airways.

4.5 Energy flux

In order to understand the physiological aspects of flow resistance during breathing, we plot the normalized energy flux along the respiratory tract in Fig. 4.7. The energy flux is the rate of transfer of energy across a surface, Γ, and is given by:

$$\text{Energy flux} = E = \int_{\Gamma} \left[\left(P + \frac{1}{2}\rho|\mathbf{u}|^2 \right) |\mathbf{u}| \right] d\Gamma \tag{4.1}$$

where P is static pressure, $\frac{1}{2}\rho|\mathbf{u}|^2$ is dynamic pressure, ρ the density of the air and $|\mathbf{u}|$ the velocity magnitude of the airflow. Time averaged measures were used for the period $[0.1-0.15\ s]$. The energy flux is computed at different cross-sections in the domain, with an orientation approximately normal to the mean flow.

As expected, the energy flux decreases along the tract at varying rates. The sharpest decreases in energy flux are coincident to large values in the integrated wall-shear stress (Fig. 4.6), indicating that the wall-shear stress plays a key role in the resistive forces during a sniff. We observe that in a few regions the energy flux does not decrease noticeably, and these correspond to regions where the flow enters a larger airspace and comparatively slows down, noticeably in the nasopharynx and the lower portion of the trachea.

53

4.6 Flapping and transitional flow in the right nasal cavity

In the following sections the unsteady dynamics of the flow are considered. The flow in the nasal cavity is transitional just downstream of the nasal valve due to the jet that is formed, but is remarkably steady after the anterior meatuses due to the reduced calibre of the passages and the large surface area. The lower airways, however, in the regions of the larynx and the trachea, exhibit turbulent flow that is triggered by the laryngeal jet and the curvature of the passage.

In order to fully resolve the temporal and spatial scales directly, the results of this section are computed using the finest mesh (M3). To provide reproducibility and clarity of results, the spectral analysis in this work is performed with a short-time Fourier transform, with a width equal to half the period and an overlap of 50% in order to reduce signal noise, and with a Hann window to ensure periodicity.

The main body of the nasal valve jet effectively does not exhibit oscillatory motion. A key feature of the transitional flow downstream of the nasal valve is the vortex shedding and flapping motion of the shear layer, located on the boundary between the nasal valve jet and the superior separated flow region. Transient motion is also seen on the lower boundary of the jet but to a smaller extent. The velocity and vorticity magnitude are plotted in Fig. 4.8 for a sagittal plane cross-section of the right nasal cavity, together with the spectral analysis of the velocity at two locations for the time period [0.08-0.12 s].

The instabilities initiate at the rapid change in geometry, downstream of the nasal valve, and are amplified as they advect downstream. As such, the oscillations recorded at the upstream point (3B) occur shortly before being observed at the downstream point (3A), with a delay of $\sim 0.002\ s$. This delay is calculated by observing the recorded time lag of the first main peak of the oscillations, for points 3A and 3B, and fits with the observation that the time average velocity magnitude in this region $\langle |\mathbf{u}| \rangle \approx 5\ m/s$ and the distance between 3A and 3B is $\approx 0.01\ m$. The flapping of the shear layer observed between points 3B and 3A, induces the roll-up and subsequent shedding of vortices, as shown in Fig. 4.9.

The amplitude of the flapping motion increases downstream, being larger at point 3A than at point 3B. From the spectral analysis of the velocity mag-
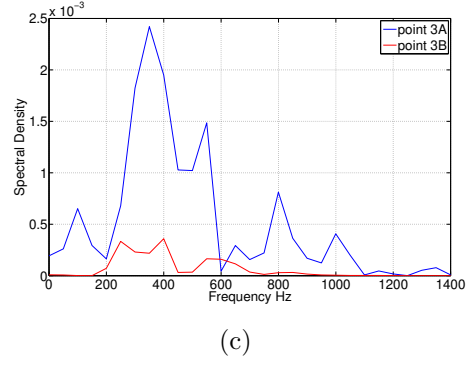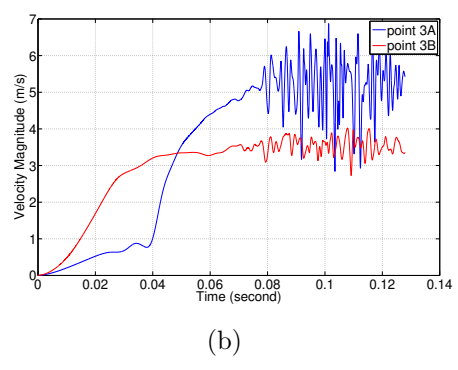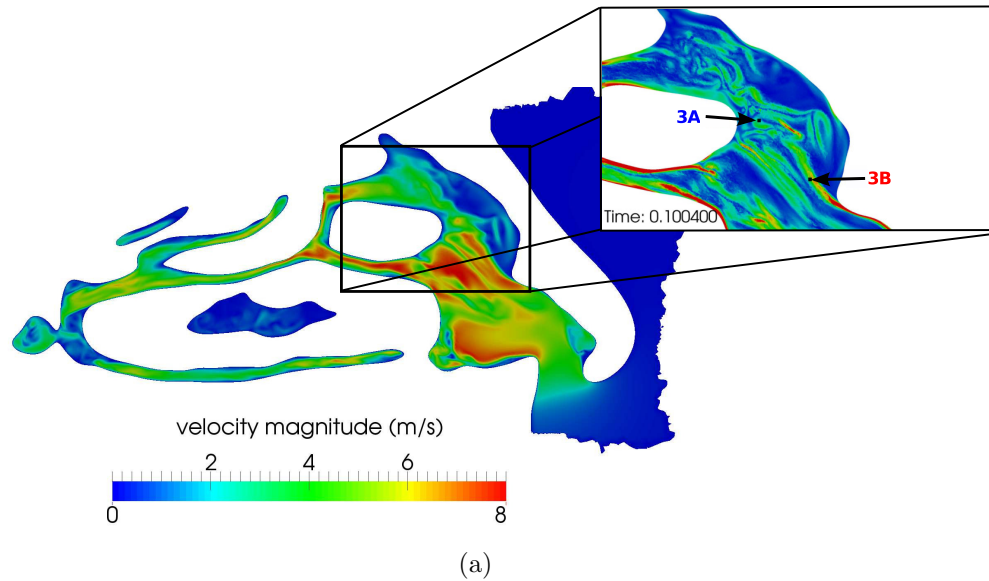
Figure 4.8: (a) Cross-section in the sagittal plane of the right nasal cavity (Fig. 2.2, plane B), showing the velocity magnitude and vorticity magnitude (the zoom highlights the occurrence of the flapping between 3A and 3B). (b) Temporal evolution and (c) spectral analysis of the velocity magnitude at two different locations (3A and 3B), during the beginning of the sniff waveform.

nitude calculated for the time window [0.08-0.12 s], the dominant frequency modes and amplitudes are rather dissimilar at these two points. There is a noticeable decrease in the modal energy and dominant frequency of oscillation for the upstream point (3B) with respect to the downstream point (3A). The dominant frequency recorded at location 3A (350 Hz) is approximately three times greater in amplitude than that recorded at location 3B. However, point locations do not represent the entire 3D field.

The development of the vortex shedding in the upper and anterior right nasal cavity is affected by the interaction with the geometry. The narrowness of the cavity dissipates the velocity gradients and the flow structures, while also increasing the vorticity magnitude. Snapshots during the vortex shedding discussed above are shown in Fig. 4.9. The period of the vortex shedding is approximately 0.0028 s, or a frequency equal to 350 Hz. It is the dominant frequency recorded at location 3A, as show in the spectral analysis in Fig. 4.8.

Unlike the right nasal cavity, the left does not exhibit a flow separation region superior to the nasal valve jet. Despite this difference, the flow remains unsteady in the left cavity and transitional during the plateau phase of the sniff waveform. A greater analysis of the bilateral cavities will be the scope of subsequent investigation.

4.7 Turbulent flow in the laryngeal and trachea regions

We will now concentrate on the analysis of the flow field along the descending airways. The dominant turbulent flow is observed in the descending airways due to the laryngeal jet. The anatomy of the subject harbours a marked reduction in airway area above the glottis due to the supine position maintained during the CT scan. In this posture the tongue and soft tissues have lowered and reduced the normal patency of the airways. A strong jet is observed that, together with the varying shape of the airways, results in a turbulent flow field that quickly dissipates through the breakup of the vortex structures.

A one dimensional spectral analysis, that considers only the vertical component of the velocity fluctuation is computed for the time period [0.1-0.15 s], the start of the plateau phase of the sniff waveform. Only the vertical compo-
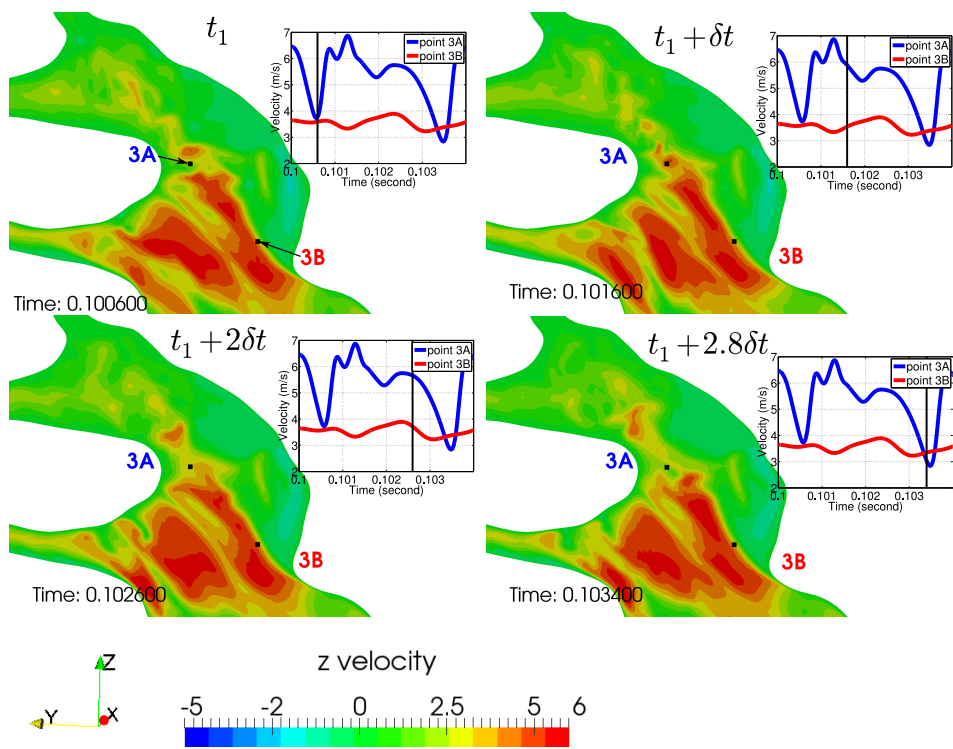
Figure 4.9: Four snapshots in the sagittal plane of the right nasal cavity, showing the vertical component of the velocity. Traces of the temporal evolution of the velocity magnitude recorded at two locations are also shown, where the vertical line indicates the current snapshot time.

	Point 7	Point 8	Point 9
$A(m^2)*10^{-4}$	1.5	2.2	2.0
$\langle|\mathbf{u}|\rangle(m/s)$	16.5	6	3.6
$Re*10^5$	2.2	1.0	0.5
$\epsilon(m^3/s^{-3})$	3300	1100	250
$\eta(\mu m)$	32	42	60

Table 4.1: Local informations about the time average velocity magnitude ($\langle|\mathbf{u}|\rangle$), the cross sectional area (A), the Reynolds Number based of the hydraulic diameter (Re), the dissipation rate (ϵ) and the kolmogorov lenght scale (η) in the three locations of picture 4.10.

nent of the velocity is considered because it is approximately the streamwise direction. Here the spectrum amplitude (E_{11}) is normalised by the Kolmogorov length scale $\eta = (\nu^3/\epsilon)^{1/4}$, where $\epsilon = 2\nu\langle S_{ij}S_{ij}\rangle$ is the dissipation rate and S_{ij} is the strain rate tensor. Here, four overlapping Hann window functions are used for the short-time Fourier transform to reduce noise. The result at three points located within the laryngeal jet as it enters the trachea, are presented in Fig. 4.10. These three locations were chosen to lie downstream of the laryngeal jet where the greatest velocity magnitude is observed, seen schematically in the figure by the mean velocity iso-surface (see also Fig. 4.3 for detail).

In this work, Taylor's hypothesis assumption is used. We convert the time sampled signal into spatial sampling with a bulk flow advection, where $\kappa = 2\pi f/\langle|\mathbf{u}|\rangle$ is the wave number related to the sampling frequency f and $\langle|\mathbf{u}|\rangle$ the local time average velocity magnitude. Varghese et al. [37] recommends the use of characteristics of the constriction to normalize the energy spectra, however here the Kolmogorov scaling is used to normalize the energy spectra following Pope [120] and Saddoughi et al. [121], for convenience and comparison purposes.

As such we can investigate the tracheal turbulent dissipation. The lines that appear in the figures correspond to the -5/3 slope, which is known as the *inertial sub-range* and is associated with the range of frequencies in which the energy cascade takes place. In this region, dominated by inertial transfer, the energy production is equal to the energy dissipation. The -10/3 slope represents the range of frequencies characteristic of the *post-stenotic flow* [36, 37, 122]. The -7 slope characterizes the *dissipation range*, where viscous
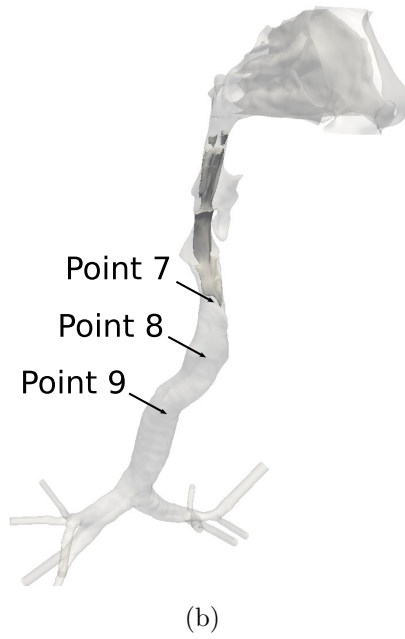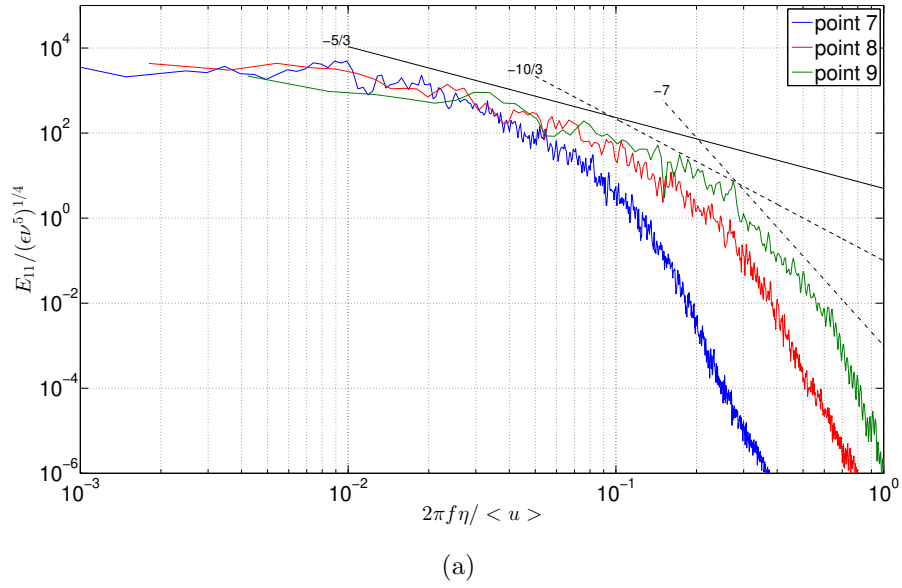
58

(a)

(b)

Figure 4.10: (a) Normalized energy spectrum of streamwise velocity fluctuations at three different locations downstream of the jet. (b) The laryngeal jet and the location of the three points.

forces dominate[120].

The energy contained at the low frequency on the 3 different spectra are approximately equal. However, a few distinct peaks in the low frequency portion of the spectrum are observed at location 7, which are not observed at locations 8 and 9. These low frequency modes are due to the presence of larger structures produced by the laryngeal jet created by the upstream constriction.

The inertial sub-range, represented by the -5/3 slope, is seen to widen and cover a greater portion of the spectrum as the flow progresses downstream. This observation indicates that progressing downstream from the region of turbulence production (the laryngeal stenosis in this subject), the energy transfers from larger to smaller eddy size, and consequently occupies a larger range at higher frequencies. These observations are consistent with the work of Varghese et al. [37] which suggest that after a certain distance from the constriction, fully developed turbulent flow is obtained for an idealised geometry. In the case of this specific subject, highly non-equilibrium flow is observed approximately around the start of the trachea.

As expected and agreeing with the observations of Varghese et al. [37], the post-stenotic regime (-10/3 slope) is more evident closer to the constriction at location 7, while this regime decreases further downstream at locations 8 and 9.

In Table 4.1, the time average velocity magnitude ($\langle|\mathbf{u}|\rangle$), the cross sectional area (A), the Reynolds number (Re) based of the hydraulic diameter, the time average velocity magnitude and the kinetic viscosity of air, the dissipation rate (ϵ) and the Kolmogorov length scale (η) are reported for the three locations identified in Fig. 4.10 during the time period [0.1-0.15 s] of the sniff waveform. As we progress downstream of the jet, both mean velocity magnitude and dissipation rate decrease, while the cross-sectional area is approximately constant. The higher velocity fluctuations, which are related to the dissipation rate, decrease as the flow moves downstream and was described also by Varghese et al. [37]. With a decrease in dissipation rate, the Kolmogorov length scale increases as the flow enters the smaller airways.

The values of the Kolmogorov length scale η, are of the same order as those observed in a pipe flow with the Reynolds number $Re \approx 10^5$, see [123]. The implication of this observation is that the complex morphology of the conduit does not play an important role in terms of the turbulence intensity. Studies on idealised pipe flow geometries may therefore be sufficient to represent dominant features of the real flow.
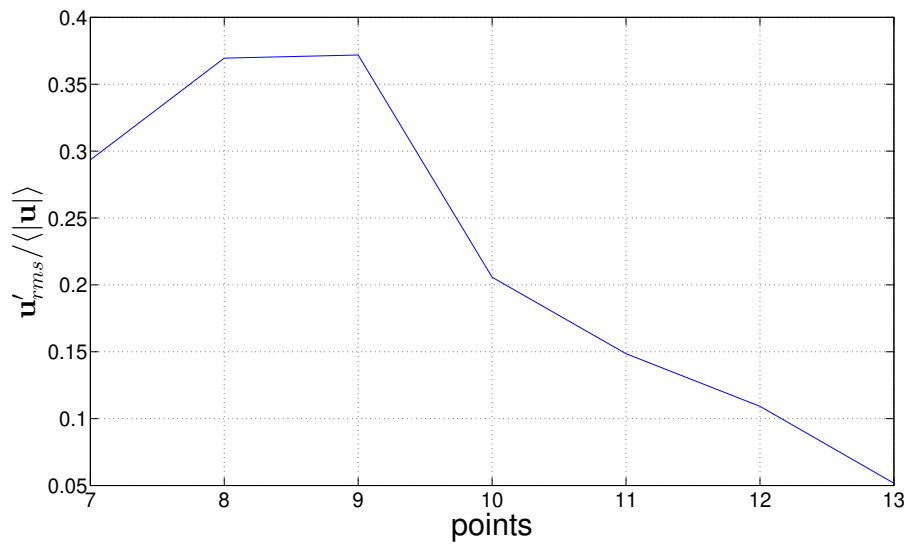
(a)
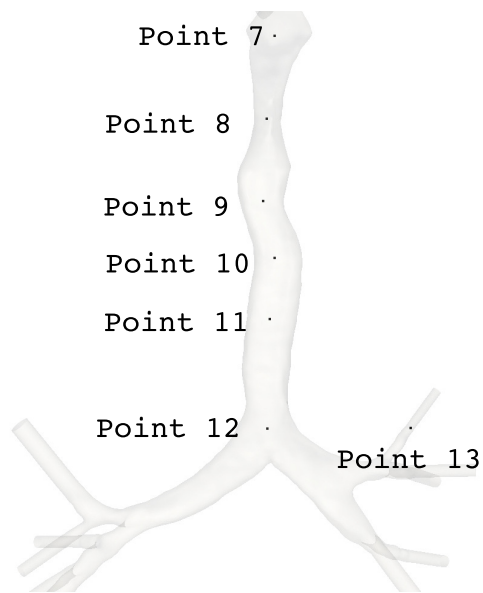
(b)

Figure 4.11: (a) Ratio of $\mathbf{u}'_{rms}/\langle|\mathbf{u}|\rangle$ computed at different points along the descending airway until the lung. (b) Representation of these point locations.

Fig. 4.11 shows the ratio of $\mathbf{u}'_{rms}/\langle|\mathbf{u}|\rangle$ computed at different points along the descending airway. This ratio is defined as turbulence level or turbulence intensity. There is a high turbulence zone for the points 8 and 9 ($\approx 40\%$). After these points, the turbulence level decreases quickly as the flow advects downstream, with a value at the carina (point 12) equal to 10%. The value of the turbulence intensity at one of the second level bifurcation (point 13) is 5%.

4.8   Energy spectra

A spectral analysis of the turbulent kinetic energy is computed for the time period [0.1-0.13 s], the start of the plateau phase of the sniff waveform. Turbulent kinetic energy is defined as:

$$TKE = 0.5(\langle u'^2\rangle + \langle v'^2\rangle + \langle w'^2\rangle) \quad with \quad \mathbf{u}' = \mathbf{u} - \langle\mathbf{u}\rangle \qquad (4.2)$$

where $\langle\mathbf{u}\rangle$ denotes the time average velocity, $\mathbf{u}'$ is the fluctuation of the velocity, and $\mathbf{u}$ is the instantaneous velocity signal.

Here the energy spectra is not normalized in the frequency domain, and is presented in Fig. 4.12 for four locations at two mesh resolutions. In order to compare the spectra, we conserve the same scaling. The four locations exhibit dramatically different flow features: the right nasal cavity (point 3), the oropharynx (point 5), the larynx (point 7), and the trachea (point 9) (locations referenced also in Fig. 2.2). These locations were chosen to investigate the turbulence characteristics occurring along the tract.

Fig. 4.12 shows that the energy content is markedly different at the different locations, with the spectral energy content in the larynx (point 7) being the highest due to the presence of large scale structures produced by the laryngeal jet. It can also be observed that the lowest energy content is located in the right nasal cavity (point 3), which is consistent with the analysis of root mean square velocity fluctuations, discussed above in Section 4.3. The well-defined low frequency peaks observed at point 3, are related to the vortex shedding as discussed in Section 4.6. The spectra scaling of the point 3 is not well adapted to the signal but as mentioned above, in order to compare the spectra, we conserve the same scaling.

As the inspired air traverses the upper airways, it first enters the nasal cavity where the turbulence intensity is low, as similarly reported by Zhao
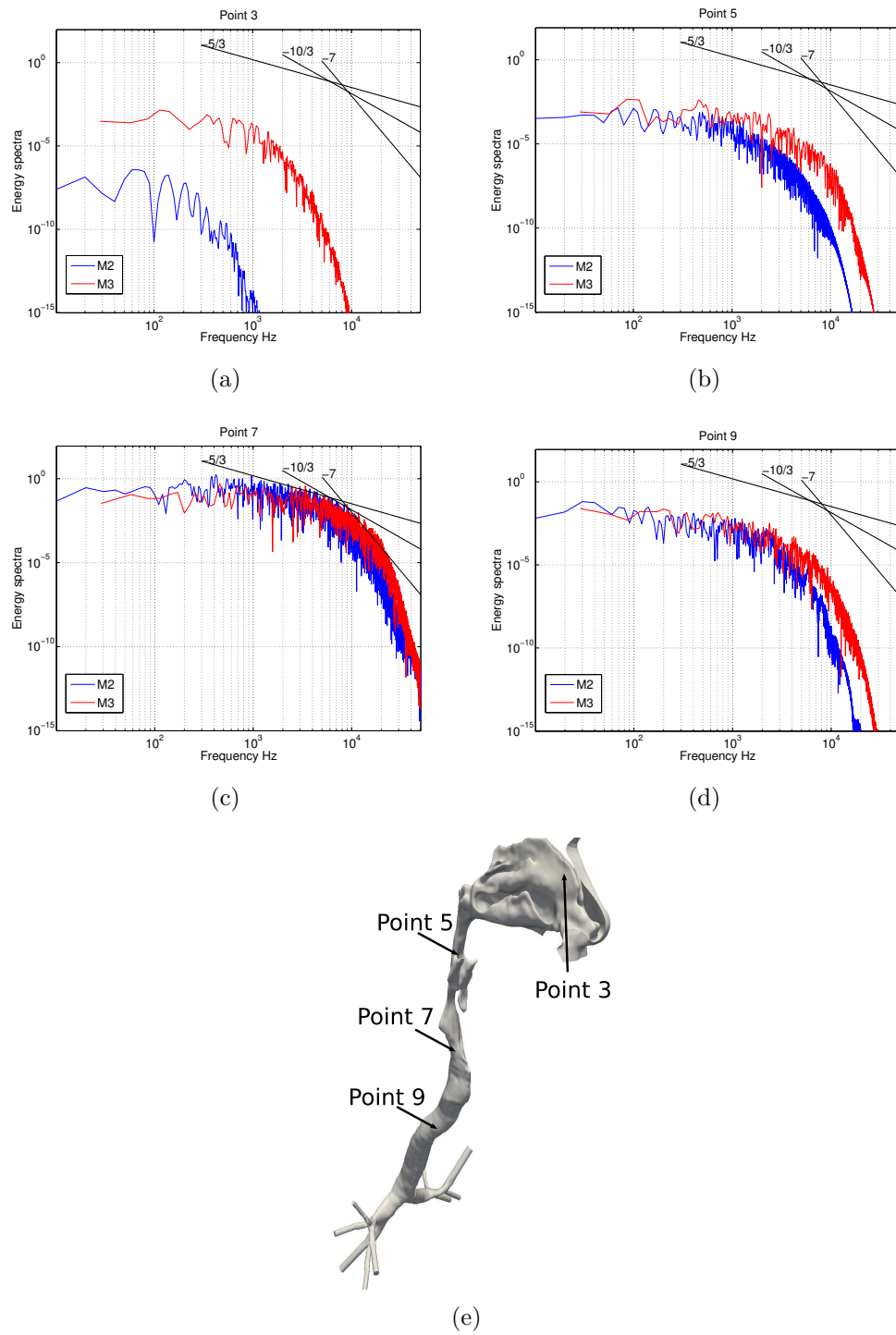
Figure 4.12: Energy spectra in four different locations, three lines denote the slopes of -5/3, -10/3 and -7, as noticed on the spectrum figures. (a) Point 3. (b) Point 5. (c) Point 7. (d) point 9. (e) Location of the points

et al. [1]. On reaching the oropharynx, turbulence is produced given the increasing velocity due to smaller cross-sectional areas. Considering the spectral energy content, the highest turbulence intensity is observed in the larynx and is related to the presence of the large structures. In the larynx, the inertial sub-range (-5/3 slope) extends to a wide frequency range compared to the other locations ($1 \times 10^3 - 5 \times 10^3 \ Hz$). The -10/3 slope associated with the post-stenotic flow is also more evident at point 7. As the flow descends the trachea, the energy of the large structures is dissipated, hence the energy content decreases and the vortical structures are broken down into smaller ones. As a consequence, the frequency spectrum and the ranges are of reduced size in comparison to the findings at point 7.

For both mesh resolutions, the inertial sub-range is similar and can be considered to be well resolved. The effect of a finer mesh resolution is seen however for the post-stenotic flow range, which extends further at higher frequencies for the finer mesh (M3). Another observation is that the slope -7 develops at lower frequencies for the M2 mesh (44M), at $10^4 Hz$, than the M3 mesh, which is approximately at $1.5 \times 10^4 Hz$. The -7 slope concerns the dominance of viscous forces.

4.9   Summary

It has been found in this chapter that whilst spontaneous fluctuations in velocity arise in the nose, the dominant site of turbulence production during inhalation is in the supra-glottic region, as opposed to the glottis itself. This finding is likely related to the effect of posture on the subject airway and highlights the need for further investigative studies. High-fidelity CFD simulations revealed the causes of flow unsteadiness and enabled the production and decay of turbulence measures to be mapped.

This inspiratory waveform is of interest as an extreme case of strong forced breathing, leading to complex fluid mechanics, and is often associated to methods of drug delivery or behaviour aspects, for example short repeated sniffing is a common inspiration waveform used to smell objects. These results show the potential of large-scale CFD simulations on detailed patient-specific geometries as a benchmark for future investigations.

In the next chapter, Lagrangian framework coupled with the flow solution is used, revealing the effects of flow behaviour and airway geometry on the deposition of inhaled microparticles.

Chapter 5

Particle results

In this chapter the results of the particle deposition under sniff condition are presented, first for each size of particles injected, i.e., 1, 5, 10 and 20 μm, then sorted with the three different phases of the sniff, i.e., acceleration, plateau and deceleration, see Fig. 2.3. Then the particle deposition efficiency, defined in Eq.2.7, in the olfactory cleft for all the injected particle sizes under sniff condition are shown.

All results presented in this chapter were obtained with the coarse mesh (M1), i.e; 9 million elements, $0.5mm$ size of volume element and time step of $1.10^{-4}s$. The motivation of using the coarse mesh and the bigger time step was firstly, a computation cost reason. It is very costly to simulate unsteady particle tracking on fine mesh and time step. Then we assumed that the unsteadiness aspect of the airflow is weak in the nasal cavity thus the deposition mechanism as inertia is relatively unaffected. Therefore the turbulent state in the laryngeal region is captured with both meshes.

5.1 Deposition pattern per particle diameter size

Fig. 5.1 shows the deposition pattern for each particle sizes injected in the realistic geometry of human upper airway system under sniff condition. η_{nasal} represents the nasal cavity deposition efficiency and d_p the size of the particle diameter. The regional deposition fraction is calculated according to the nomenclature defined in Fig. 2.2. Nasal cavity encompasses vestibule, nasal valve and airway.
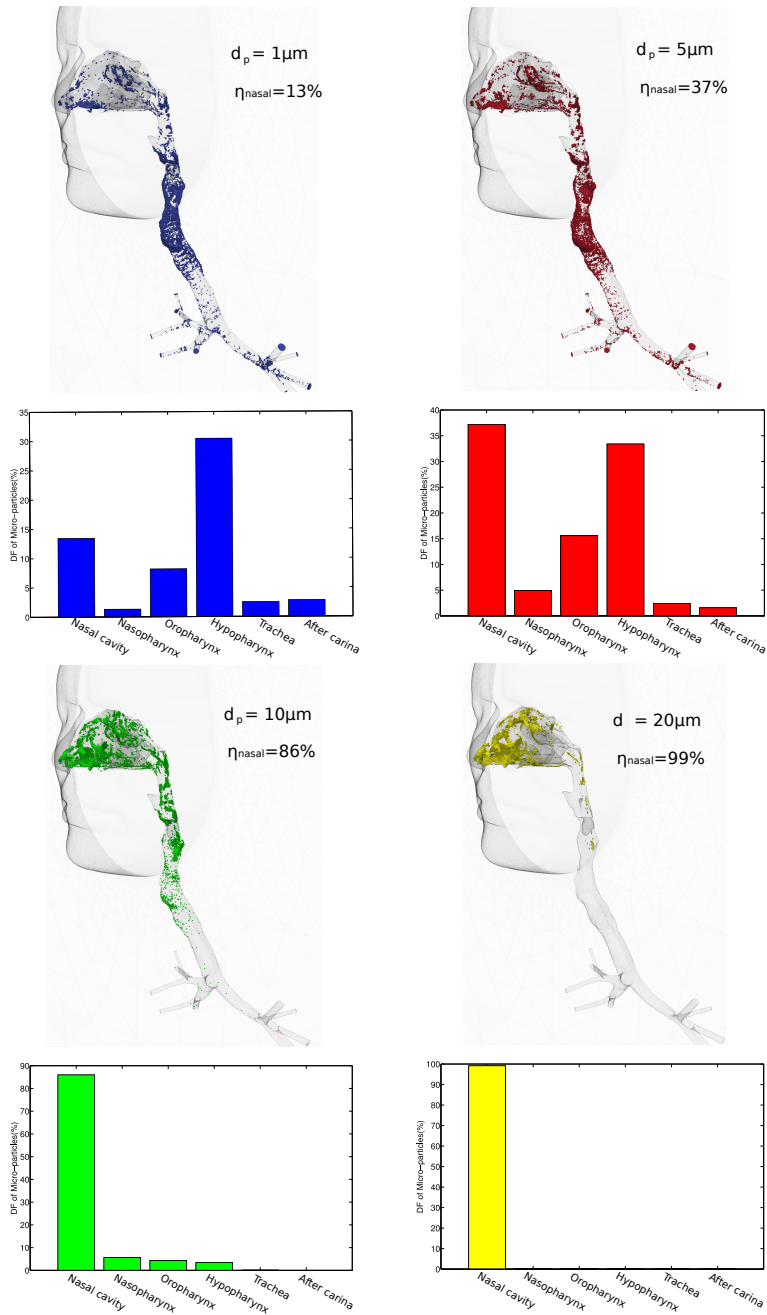
Figure 5.1: Deposition patterns and regional deposition fraction for 1, 5, 10 and 20 μm during the sniff.

Clearly the main physical mechanism of deposition in action at this range of particle size under sniff condition is the inertial impaction, which is proportional to the airflow rate and the particle diameter squared, as expressed with the impaction parameter in Eq.2.6.

η_{nasal} increases when particle diameter size increases, until almost 100% for the particle aerodynamic diameter $20\mu m$. As a consequence of their higher inertia and deviation from the flow streamlines, larger particles (10 and 20 μm) stay trapped in the nasal cavity playing the role of filter. On contrary, smaller particles (1 and 5 μm) with low inertia can penetrate further. These smaller particles have the tendency to be deposited more uniformly than larger particles along the respiratory tract even until the lungs. Some local prominent accumulation of deposited particles, also called hot spot are observed which are located in some places in the nasal cavity then in the nasopharynx and finally in the larynx. A greater analysis of the zonal deposition in the nasal cavity will be the scope of subsequent investigation.

The hot spot observed in the nasopharynx is produced by the centrifugal force occurring in the 90° bend passageway acting on the particles. The other hot spot is located in the laryngeal region. The nature of the flow on this region is largely discussed on Section 3.3 and it is demonstrated that the level of turbulence intensity is the highest on the respiratory tract under sniff condition. This chaotic flow highly promotes the particle deposition through the turbulence dispertion mechanism.

5.2   Deposition pattern per phase

Fig. 5.2 shows the deposition pattern for all the injected particle sizes under the three different phases of the sniff condition as we could see in Fig. 2.3 and the regional deposition fraction corresponding.

Acceleration phase. The inlet flow rate increases suddenly from zero to $1L/s$ in $0.1s$. This short and rapid acceleration produces some clear observations concerning the deposition. As mentioned before in this section, the main physical mechanism of deposition in this study is inertial impaction. It is clearly observed with the regional deposition fraction than increasing the flow rate and particle diameters, the deposition efficiency increases. The pattern of the deposition shows that lager particles (green and blue spheres) are located in the nasal cavity. The higher inertia and deviation from the flow streamlines of larger particles produce under the acceleration condition
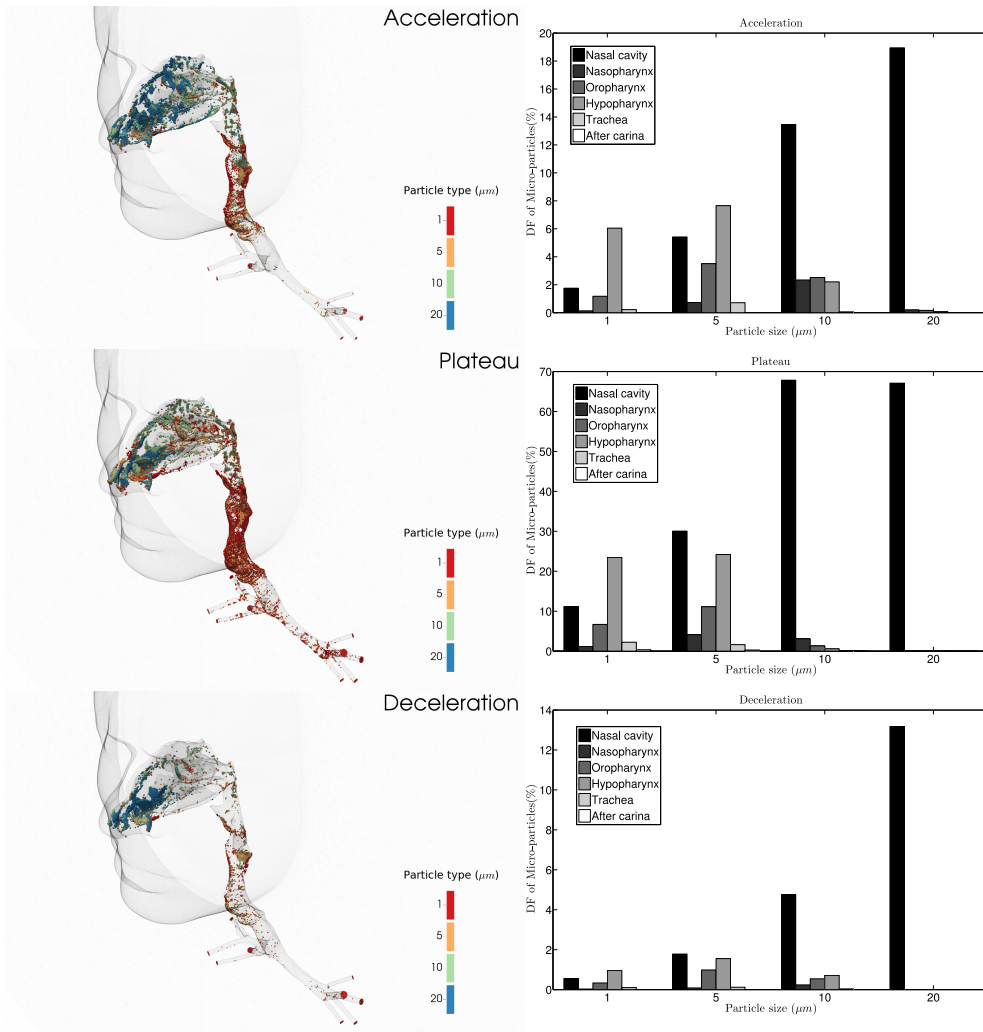
Figure 5.2: Deposition patterns and regional deposition fraction for the three phases of the sniff: acceleration, plateau and deceleration, see Fig. 2.3.

68

this important deposition in the nasal cavity. On the contrary, deposition of smaller particles (red and orange spheres) are scattered along the respiratory tract, more precisely in the laryngeal region.

Plateau phase. During this phase, the flow rate is approximately constant during 0.2s. The deposition fractions are almost equivalent for lager particles and are located exclusively all in the nasal cavity. As under the acceleration condition, the deposition fraction for smaller particles are scattered along the respiratory tract with higher value in the hypopharynx for 1 μm particle size and the nasal cavity for 5 μm particle size. It is noticeable that the regional deposition fraction is clearly identically proportional as pattern under the plateau condition that under the entire sniff condition, see Fig. 5.1. Some conclusions could be formulated than the particle deposition would be equivalent under the sniff condition and equivalent steady inhalation condition. This hypothesis would help to reduce the computational cost of the simulation. This assumption has to be verified and will be the scope of subsequent investigation.

Deceleration phase. The values of particle deposition during the period of the deceleration are the lowest of the three phases. The deposition pattern is very similar to the acceleration one.

5.3   Deposition efficiency in the olfactory cleft

Fig. 5.3 shows the particle deposition efficiency in the olfactory cleft for all the injected particle sizes under sniff condition. As expected, the values of η_{olfa} are low, as the olfactory cleft region is a protected zone in the nasal cavity, see Section 3.1. Although the deposition efficiency of the 10 μm particle size is remarkably high, as 2.7%. Even the 20 μm particle size is important with 0.5%. [55] compared the olfactory deposition of inhaled nano-particles in humans and in rats and they commentated that the highest value was $\eta_{olfa} = 1\%$. Naturally the conditions of the present study are different, lower and constant flow rate and with nano-particles. However the olfactory region is a challenging target for the drug delivery in respiratory airways. $\eta_{olfa} = 2.7\%$ for 10 μm particle size represents an important dose of therapeutic aerosols. Even if olfactory deposition is expected to vary among individuals [55], more investigations is required to confirm the trend.

69
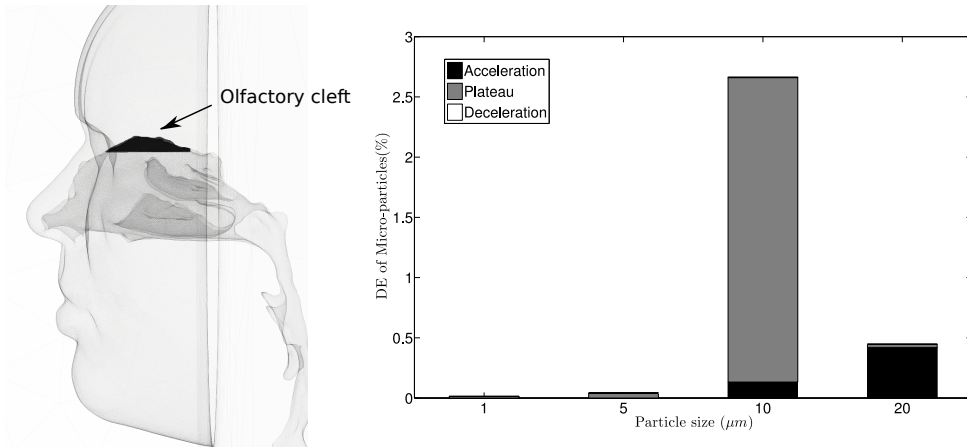
Figure 5.3: Location of olfactory cleft and deposition efficiency for 1, 5, 10 and 20 μm under sniff condition.

5.4 Summary

Micro-particle deposition in the realistic geometry of human upper airway system under sniff condition demonstrated that the most important deposition mechanism is inertial impaction. As consequence of their higher inertia and deviation from the flow streamlines, larger particles (10 and 20 μm) stay trapped in the nasal cavity playing the role of filter. On contrary smaller particles (1 and 5 μm) with low inertia can penetrate further. These smaller particles have the tendency to be deposited more uniformly than larger particles along the respiratory tract even until the lungs. Some hot spots are observed, whose the most important is the laryngeal region, where chaotic flow highly promotes particle deposition.

The regional deposition fraction is almost identical under the plateau condition that under the entire sniff condition. Furthermore the highest deposition efficiency in the olfactory region is $\eta_{olfa} = 2.7\%$ for 10 μm particle size, which represents an important dose of therapeutic aerosols. This finding has to be investigated in future investigations with finer mesh density and smaller time step.

Due to the posture of the subject, the production of turbulence in the supra-glottic region, and its intensity, may be considerably altered if the subject were in the upright position, for example as the tongue would not relax into the airspace. Further investigation of the anatomy geometry in

different postures will be beneficial, as well as analysis of further subject specific cases. The study has considered a specific waveform, namely a sniff profile taken as from population average, and it will be valuable to explore the fluid mechanics for different breathing patterns.

Olfactory region still the challenging target for the drug delivery in respiratory airways. In this context, the next chapter will present nasal sprayed particle deposition in a human nasal cavity under different inhalation conditions.

Chapter 6

Drug delivery application

The previous three chapters have characterised and quantified the dynamic and unsteady flow and particle deposition occurring in the large airway during a rapid and short inhalation. In this chapter, the drug delivery application associated with this inspiratory waveform is presented.

Deposition of polydisperse particles representing nasal spray application in a human nasal cavity was performed under transient breathing profiles. The LES turbulence model was used to describe the fluid phase. Particles were introduced into the flow field with initial spray conditions, including spray cone angle, insertion angle, and initial velocity. Since nasal spray atomizer design determines the particle conditions, fifteen particle size distributions were used, each defined by a log-normal distribution with a different volume mean diameter (Dv50).

The truncaded geometry was used to reduce the computation domain and focus the study on the human nasal cavity only. Futhermore the geometry included a spray nozzle inserted into the left nostril which created an occluded nostril opening, see Fig. 6.1. The precise location of the nozzle is discussed later.

A serie of meshes were created for the study, see Table 6.1. All the mesh procedure is explained in detail in Chapter 2, see Section 2.2.

6.1 Boundary and initial conditions

The computational domain included a large hemisphere surrounding the patient's face that ensured an accurate velocity field in the vicinity of the nos-

Mesh	$N_N(\times 10^6)$	$N_E(\times 10^6)$	$\Delta t(\mu s)$	$\Delta(mm)$	N_{pl}	$h_{pl}(mm)$
N1	0.6	2.3	5.8	0.8	3	0.6
N2	1.8	6.3	3.7	0.4	5	0.3
N3	14.2	50.1	1.2	0.2	10	0.3

Table 6.1: Summary of different mesh resolutions and simulation parameters with N_N: number of nodes, N_E: number of elements, Δt: time step, Δ: grid size, N_{pl}: number of prism layers and h_{pl}: height of total prism layer.
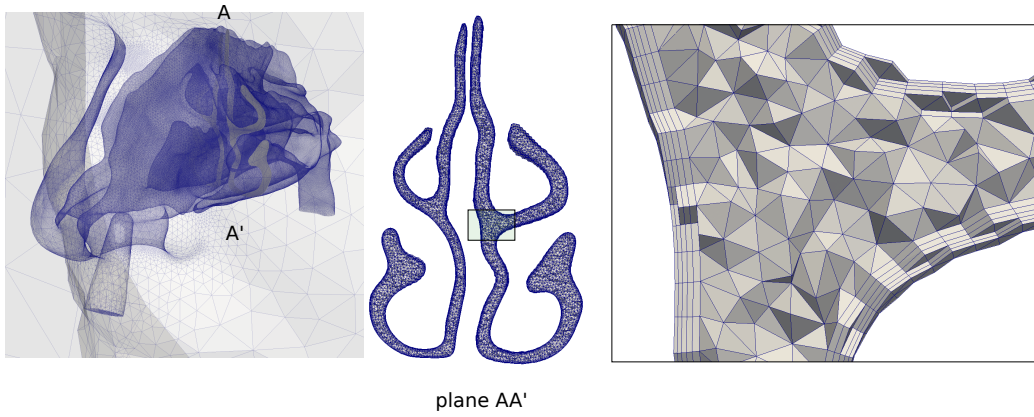

plane AA'

Figure 6.1: Grid generation topology for N2

trils [29, 108]. A no-slip boundary condition was imposed on all airway walls and the flat surface of the hemisphere to mimic the effects of the face and body.

Inflow condition: Nasal spray medicines typically have more variable bioavailability than medicines delivered by other routes of administration because of variability associated with use (e.g. in the patient's inspiratory flow pattern). While patients are instructed to breathe in slowly during the application, other modes of breathing can occur, such as a sniff, or a breath hold. Three different inhalation conditions were investigated. i) a sniff, labelled as profile A1; ii) constant flow rate, labelled as profile A2; and iii) breath hold, labelled as profile A3.

The sniff (profile A1) was in the form of a rapid and short inhalation, which was transient and prescribed as a time varying uniform velocity with direction normal to the hemisphere. To model the sniff, we used a polynomial function of order 10 derived from the experimental work detailed in [103], also see Chapter 2, Section 2.5 for further detail. The constant flow rate (profile A2) was set to $Q = 20L/min$. This is frequently used in the literature and considered as normal constant breathing inspiration. [104, 112, 47]. The non-breathing flow (profile A3) was created with a zero velocity field on the entire domain, which depicts a long holding breath with the assumption of no inhalation/exhalation effects. The inlet velocity profiles for A1 and A2 (Fig. 6.2) were imposed as a Dirichlet condition on the hemisphere dome.

Outflow condition: A zero-traction outflow condition was imposed as a Neumann condition (the surface is free from external stress) at the outlet of the naso-pharynx.

6.2 Large eddy simulation method

The fluid solver used the high performance computational mechanics code Alya [83], developed at Barcelona Supercomputing Center. The spatially filtered Navier-Stokes equations for a fluid moving in the domain Ω bounded by $\Gamma = \partial\Omega$ during the time interval (t_0, t_f) consist in finding a filtered velocity $\overline{\mathbf{u}}$ and the static pressure p such that
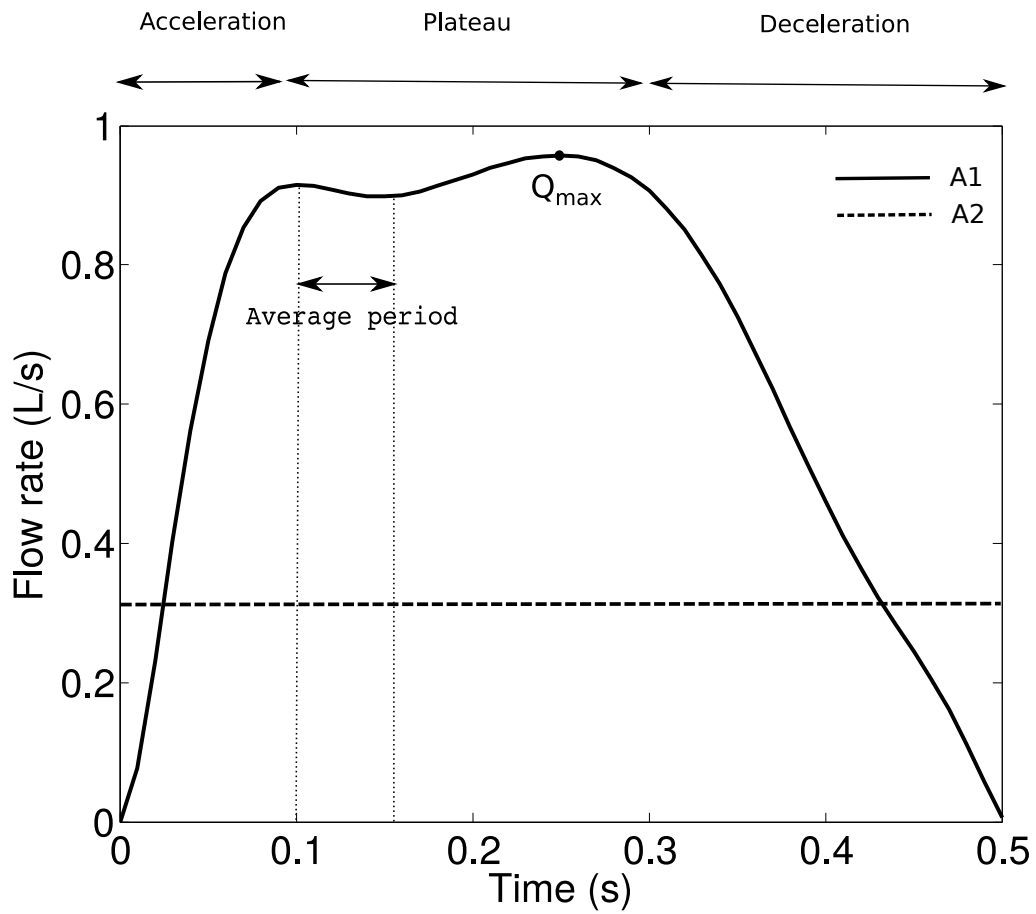
Figure 6.2: Flow rate profiles of different inhalation conditions, A1 and A2

$$\frac{\partial \overline{\mathbf{u}}}{\partial t} + (\overline{\mathbf{u}} \cdot \nabla)\overline{\mathbf{u}} - 2\nu\nabla \cdot \mathbf{S}(\overline{\mathbf{u}}) + \frac{1}{\rho}\nabla p - \mathbf{f} = -\nabla \cdot \tau_{\mathbf{ij}}(\overline{\mathbf{u}}) \qquad \text{in } \Omega \times (t_0, t_f),$$

$$(6.1)$$

$$\nabla \cdot \overline{\mathbf{u}} = 0 \qquad \text{in } \Omega \times (t_0, t_f), \qquad (6.2)$$

where ν is the kinetic fluid viscosity, $\mathbf{f}$ the vector of external body forces and $\mathbf{S}(\overline{\mathbf{u}})$ is the large-scale rate-of-strain tensor. In Eq 6.1 $\tau_{\mathbf{ij}}(\overline{\mathbf{u}})$ is the subgrid scale (SGS) stress tensor, which must be modelled. Its deviatoric part is given by

$$\tau_{\mathbf{ij}}(\overline{\mathbf{u}}) - \tfrac{1}{3}\tau_{\mathbf{kk}}(\overline{\mathbf{u}})\delta_{\mathbf{ij}} = -2\nu_{sgs}\nabla \cdot \mathbf{S}(\overline{\mathbf{u}}) \qquad (6.3)$$

where $\delta_{\mathbf{ij}}$ is the Kronecker delta. Suitable expression of the subgrid-scale viscosity, ν_{sgs} was used to close the formulation. The wall-adapting local-eddy viscosity model (WALE)[124] was applied. This model has demonstrated good results in simulations of respiratory airways which is comparable to more computational demanding models like the dynamic Smagorinsky model (see [125]).

In the following we consider the skew-symmetric form

$$NL_{skew}(\mathbf{u}) = \mathbf{u} \cdot \nabla\mathbf{u} + \frac{1}{2}(\nabla \cdot \mathbf{u})\mathbf{u}$$

which has the advantage that it conserves kinetic energy at the discrete level and is commonly used in numerical analysis and DNS and LES simulations where energy conservation provides enhanced results (see for instance [126, 127, 128]).

A non-incremental fractional step method was used to stabilise pressure. This allowed the use of finite element pairs that do not satisfy the inf-sup conditions, such as equal order interpolation for the velocity and pressure used in this work. The set of equations is time integrated using an energy conserving Runge-Kutta explicit method lately proposed by [129] combined with an eigenvalue based time step estimator [130].

In the LES approach, the grid resolution (Δ), which is the filter size, and time resolution (Δt) are crucial to obtain a reasonable ratio between the grid size and the smallest eddies of the turbulent motions (the Kolmogorov scale, η). While there is no universally accepted criterion for LES grid size requirement, a ratio $\frac{\Delta}{\eta}$ less than 20 is reasonable [131]. The grid resolution should also be between the turbulent length scales of Taylor microscale (λ)

76
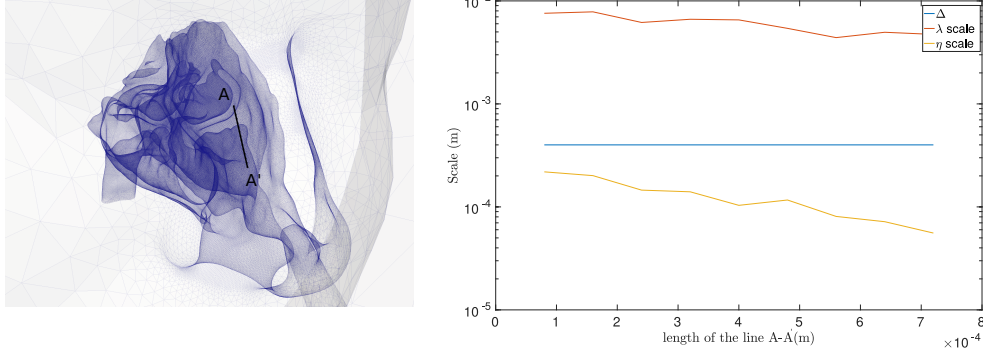
Figure 6.3: Comparison of different turbulence scales (N2 mesh and $Q_{max} = 57.4L/min$) on the most critical region (downstream of nasal valve).

and Kolmogorov scales (η). The Taylor microscale is used to characterise a turbulent flow and is larger than Kolmogorov scale [132]:

$$\lambda = \sqrt{\frac{10(\nu + \nu_{sgs})TKE}{\varepsilon}} \qquad (6.4)$$

$$\eta = \left(\frac{(\nu + \nu_{sgs})^3}{\varepsilon}\right)^{\frac{1}{4}} \qquad (6.5)$$

where TKE is the turbulent kinetic energy, ε is the turbulent dissipation rate, ν is the fluid kinetic viscosity, and ν_{sgs} is the subgrid-scale viscosity. Fig. 6.3 shows the grid size (Δ) of model N2 compared to the turbulence scales along line A-A', which is located downstream of the right nasal valve at the maximum of the sniff profile $Q_{max} = 57.4L/min$. The grid size was between the Taylor and Kolmogorov scale and the equivalent ratio $\frac{\Delta}{\eta}$ was 3. With this criterion we affirm that the grid is sufficiently fine for LES.

all the informations about the particle solver is given in Chapter 2, see Section 2.4.

6.3 Nasal spray

Experimental measurements of particle size distributions produced from nasal spray devices [133, 134, 135, 136] were used as a base to define the initial particle conditions. Additional data from [69] was also used which included

77
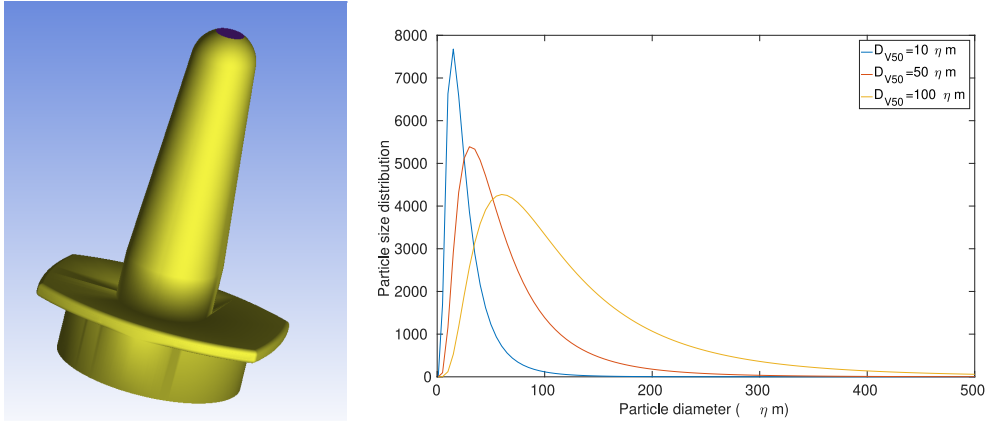
Figure 6.4: Log-normal distribution function showing the profiles for medians of $D_{V50} = 10, 50, 100$

reported values of spray angles from 32° to 79°, averaged spray velocity 1.5 to 14.7 m/sec, and mean droplet size of 50μm. The sprayed particle conditions in this study were: spray half cone angle = 40° ; mean spray exit velocity= 18.0m/s; and a solid-cone type injection was assumed. The particle sizes were defined with a log-normal distribution defined through the probability density function

$$f(x) = \frac{1}{\sqrt{2\pi}x\ln\sigma_g}\exp\left[-\frac{(\ln x - \ln x_{50})^2}{2(\ln\sigma_g)^2}\right] \tag{6.6}$$

where x is the particle diameter. The log normal distribution median was initially set to x_{50}, also know as $Dv50$ which is the volume median diameter, and $\ln\sigma_g$ is the standard deviation, where $\sigma_g = 2.08$.

Nasal spray atomizers can be designed to change the particle size distribution. The volume median diameter of Eq 6.6 was changed in the range $Dv50 = 10-150\mu m$ in increments of $10\mu m$, to observe its influence on particle deposition. The resulting particle size distributions for $Dv50 = 10, 50, 150\mu m$ are shown in Fig. 6.4. The total number of particles released in one actuation was approximately 1 million.

A realistic nasal spray device based on the Flonase and Beconase devices, was included where the nozzle length was $2cm$ (Fig. 6.5). [137] suggested that vestibular nozzle insertion in a 3D nasal model was not essential for reliable airflow simulations as the inlet perturbations (due to the nozzle placement
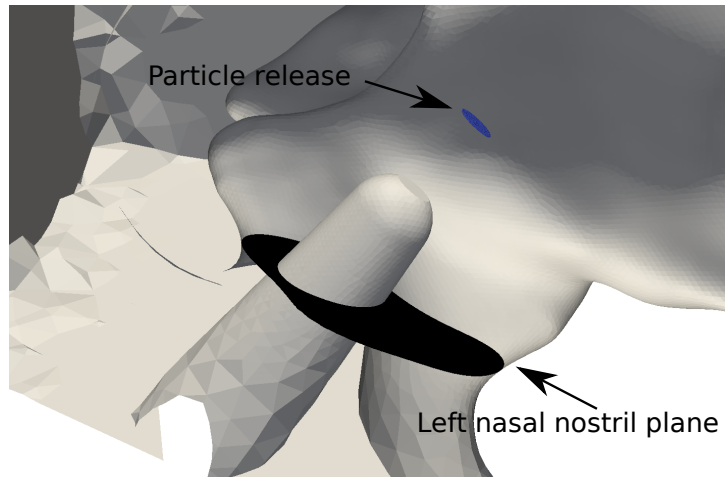
Figure 6.5: Spray insertion into nasal cavity, showing relative distances. Particles released from a break-up distance downstream from the spray nozzle.

zone) hardly affected the posterior airflow and particle transport and deposition trends. Their study used laminar flow models of flow rates based on the subject-specific allometric scaling [138], $\dot{V} = 1.36M^{0.44}$ for males (sitting awake) and $\dot{V} = 1.896M^{0.32}$ for females (sitting awake). Inclusion of the spray nozzle produces an occluded flow region at the nostril inlet and this leads to increased local flow acceleration. This is expected to be strengthened in the sniffing condition where the peak flowrate was 5 times of [137]. Further differences include a turbulent flow field which accounts for the stronger inlet perturbations not found in resting laminar breathing rates.

The intranasal spray guide by [139] suggests nasal sprays be directed away from the septum and towards the lateral nasal wall. The nozzle in this study was placed 0.5cm into the centroid of the left nasal nostril plane (see Fig. 6.5) at an insertion angle of 30° to the coronal vertical axis, and 20° to the saggital vertical axis.

Particles were introduced into the computational domain from a breakup length of $3mm$ from the nozzle exit [133] at the start of the simulation and re-injected every $0.005s$ until the last injection time ($0.08s$) thus a total of 16 injections. This produced a total of 1million particles released during the entire simulation. The number of suspended particles remaining in the domain at the end of the simulation was negligible considering the total deposited.

All the validation about particle deposition is presented in Chapter 2, see Section 2.6.

6.4 Modelling of surface area deposition coverage

To convert deposition of a Lagrangian particle onto a surface, a projection on the boundary mesh was used. A given surface B was considerd as composed of the union of boundary mesh elements b of which particles deposit onto. Setting n_b^{boun} as the number of particles accumulated on a particular mesh element b and $\rho_b^{boun} = n_b^{boun}/|b|$ is the particle number density on each element, where $|b|$ is the area of element b. To pass these boundary densities to the nodes of the mesh, a L^2-projection method was used to (e.g. transfer of a discontinuous field to a continuous nodal field). Setting ρ_i^{node} as the density of particles on each node i, and applying the projection produces:

$$\sum_b \sum_j \int_b N_i N_j \rho_j^{node} db = \sum_b \int_b \rho_b^{boun} N_i db \quad \forall\, i \in B,$$

where N_i's are the boundary shape functions associated with the boundary nodes $i = 1, 2, \ldots$. The left-hand side term can be lumped in order to obtain a diagonal mass matrix to solve for ρ_i^{node} on each node i.

Summing over i, and noting that $\sum_i N_i = 1$, produces:

$$\sum_b \sum_j \int_b N_j \rho_j^{node} db = n_b^{boun}, \tag{6.7}$$

which conserves the total number of particles on both the boundary and nodal information (Fig. 6.6)

6.5 Computational requirements

The simulations were carried out on the MareNostrum supercomputer, hosted by the Barcelona Supercomputing Center. For instance, to carry out the simulation on the MareNostrum, 110,000 time-steps are required on 480 cores requiring approximately 20h for A1, 15h for A2 and 2h for A3. In order to keep a good parallel efficiency, between 20,000 and 30,000 elements are used on each core.

B

Particle density ρ_b^{boun} per boundary b ▶ Project ρ_b^{boun} from boundaries to nodes ρ_i^{node}
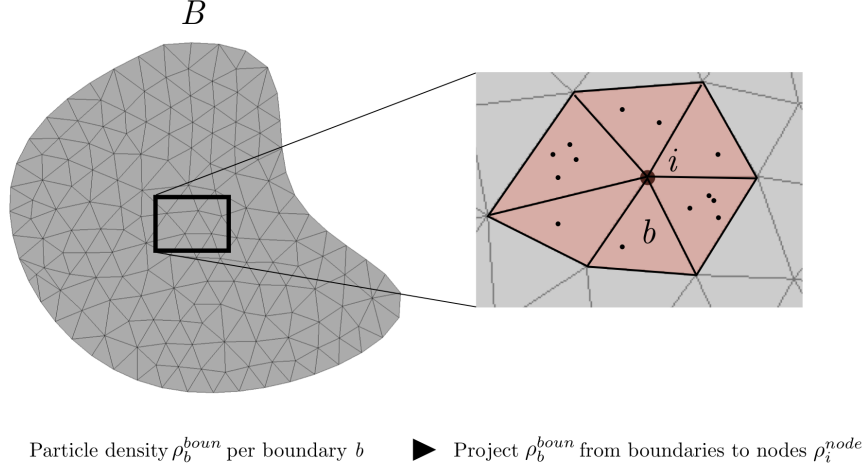
Figure 6.6: Transferring the boundary density of particles ρ_b^{boun} to the nodes ρ_b^{node} via a projection.

6.6 Results

6.6.1 Airflow field

Fig. 6.7 displays the pressure loss between inside the nostril to the nasopharynx in the left and right nasal cavity for both inhalation conditions. Increased resistance was found in the left nostril due to the nozzle which occluded the nostril area and this led to higher pressure loss in the left chamber for both inhalation conditions. The pressure drop between left and right chamber for sniff breathing (time period of $0.1s$ to $0.15s$) was $30Pa$, which was six times larger than for the constant flow rate that was $5Pa$. The sniff peak flow rate during time $0.1s$ to $0.15s$ was approximately 2.85 times larger.

The oscillations observed in Fig. 6.7 for the sniff inhalation condition are produced by flow features occurring downstream of the nasal valve and instabilities in the main passage way. A key feature of the transitional flow downstream of the nasal valve is the vortex shedding and flapping motion of the shear layer, located on the boundary between the nasal valve jet and the superior separated flow region, which was reported in [6, 140].

The time-averaged velocity flow field provides an overview of persistent flow features and flow distribution; while temporal fluctuations describe the

81

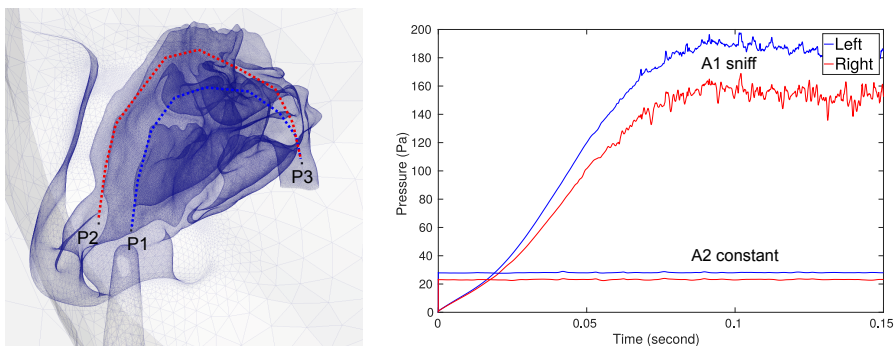Figure 6.7: Static pressure drop across the right and left nasal cavity during time period ($0.0s$ to $0.15s$) for A1 and A2 inhalation conditions.

turbulent kinetic energy (TKE). The mean flow and TKE was obtained in plane-A and plane-B, (Fig. 6.8,6.9).

The mean velocity for sniff inhalation was approximately two times higher than for the constant flow. Despite this difference, complex flow patterns caused by the nozzle insertion were found under both inhalation conditions (see Plane A of Fig. 6.8). In particular, there is high velocity and recirculation found in the vestibule and the nasal valve regions. In the coronal section (plane B), flow occurs through the middle of the nasal cavity for both inhalation conditions and there is higher velocity through the right chamber. The uneven flow distribution is more pronounced for the sniff inhalation condition where the inter-chamber difference in pressure was $30Pa$.

Fig. 6.9 shows velocity fluctuations on the sagittal/coronal sections where the order of magnitude is more than twice as large for sniffing condition compared with constant inhalation. The sagittal view (plane A) showed high TKE values in the vestibule and the nasal valve. The presence of the nozzle produced local unsteady flow fluctuations downstream, as the consequence of the left nostril area reduction and the complex geometry in the anterior nasal cavity. The coronal view (plane B) highlights the TKE difference between left/right chambers way and the difference in turbulent energy for both inhalation conditions. There is a non-negligible value of TKE on the left chamber particularly for the sniff (A1), which is a result of the upstream flow. The flow fluctuations occurring in the left vestibule gradually decreased in intensity as it is convected through the nasal cavity.

Figure 6.8: Mean velocity of sagittal plane of left nasal cavity (plane A) and coronal plane in the middle of nasal cavity (plane B) computed for the time period $0.1s$ to $0.15s$ for A1 and A2 inhalation conditions.

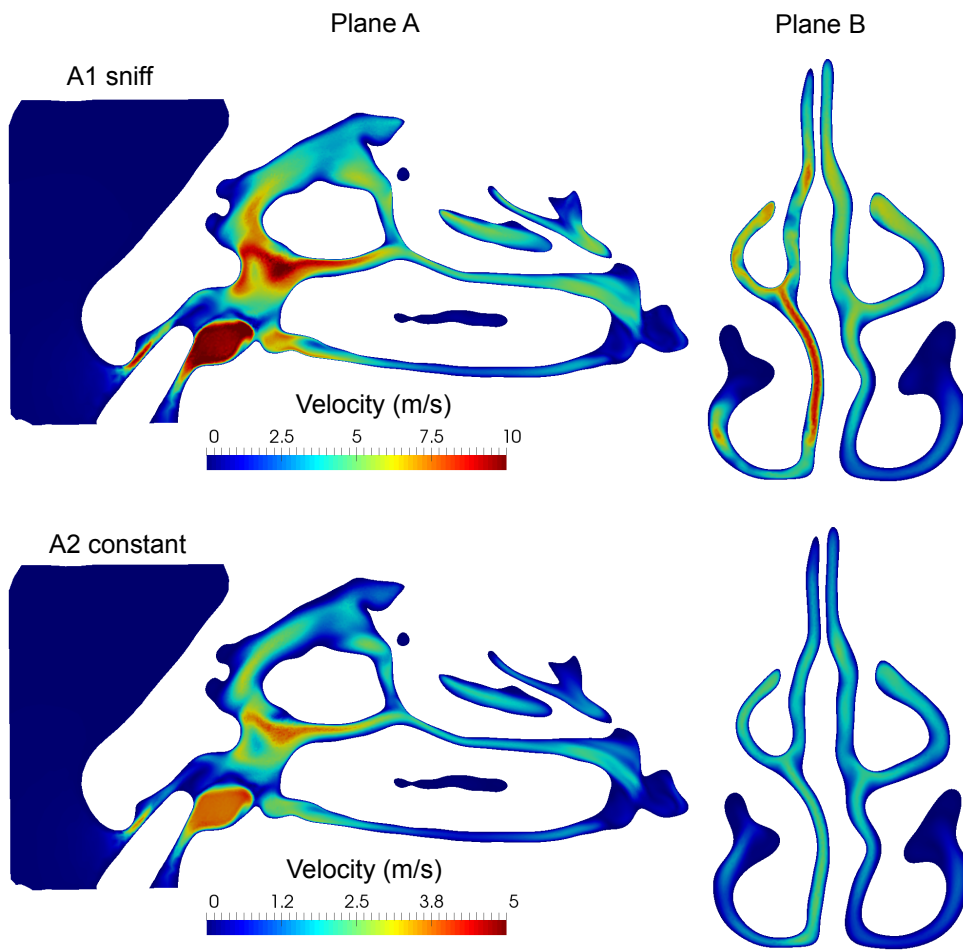Figure 6.9: Turbulent kinetic energy $(\mathrm{m}^2/\mathrm{s}^2)$ of sagittal plane of left nasal cavity (plane A) and coronal plane in the middle of nasal cavity (plane B) computed for the time period $[0.1 - 0.15s]$ for A1 and A2 inhalation conditions.
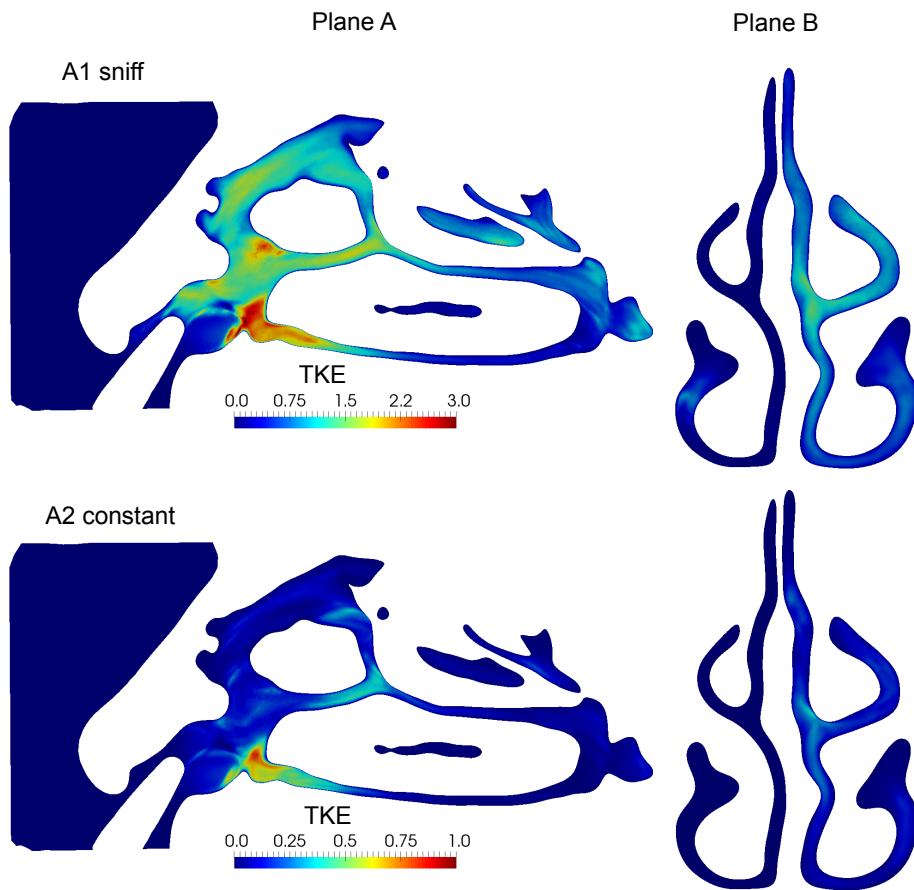
6.6.2 Particle deposition

Regional deposition

Sprayed particle deposition across the nasal cavity regions was affected by flow profile and particle size distribution (Fig. 6.10). When $Dv50 > 50\mu m$ deposition in the anterior region was stable at 80%. However, when $Dv50 < 50\mu m$ anterior deposition decreased for sniff and steady inhalation, while it increased for a breath hold (A3) reaching a peak deposition of 98%. A similar trend was found in the middle nasal cavity region, where $Dv50 > 50\mu m$ produced relatively constant deposition efficiency of 18-22% for all breathing profiles. For $Dv50 < 50\mu m$ a sniff condition increased deposition, while constant breath, and breath hold reduced the particle deposition. For $Dv50 = 10\mu m$ there was increase in deposition in the posterior region which suggests particles passed through the anterior region, it also passed through the main nasal passage, and increased deposition in the posterior region. This is attributed to a large proportion of the particle size distribution behaving with non or low inertial properties, typically $D_p < 5\mu m$.

In the posterior region, the sniff condition transported particles deep enough for deposition, although this influence was limited to particle size distributions with $Dv50 < 50\mu m$. The constant breath exhibited a small number of deposited particles ($< 1\%$) while no particles deposited in this region during breath hold. In all breathing cases, deposition in the olfactory region was very minimal with less than 0.3% deposition. This suggests the settings used to define the sprayed particle conditions are not suitable for attempting targeted drug delivery to the brain via the olfactory bulb.

Deposition Pattern

The deposition pattern for particle size distribution of $Dv50 = 50\mu m$ is similar for all breathing profiles − where the deposition region is inline with the direction of the nozzle. The location is superior to the main nasal passage opening, and just anterior of the olfactory region. Since micron particle deposition has strong dependence with the inertial properties of the particle, it is evident that the deposition pattern is a consequence of this. From Fig. 2.5, deposition of $D_p > 25\mu m$ produced $> 99\%$ deposition efficiency. The particle size distribution in Fig. 6.11 exhibited a larger proportion of particle diameters greater than $D_p > 25\mu m$. The effect of convection caused by inhalation is evident from the particle transport through the nasal passage.
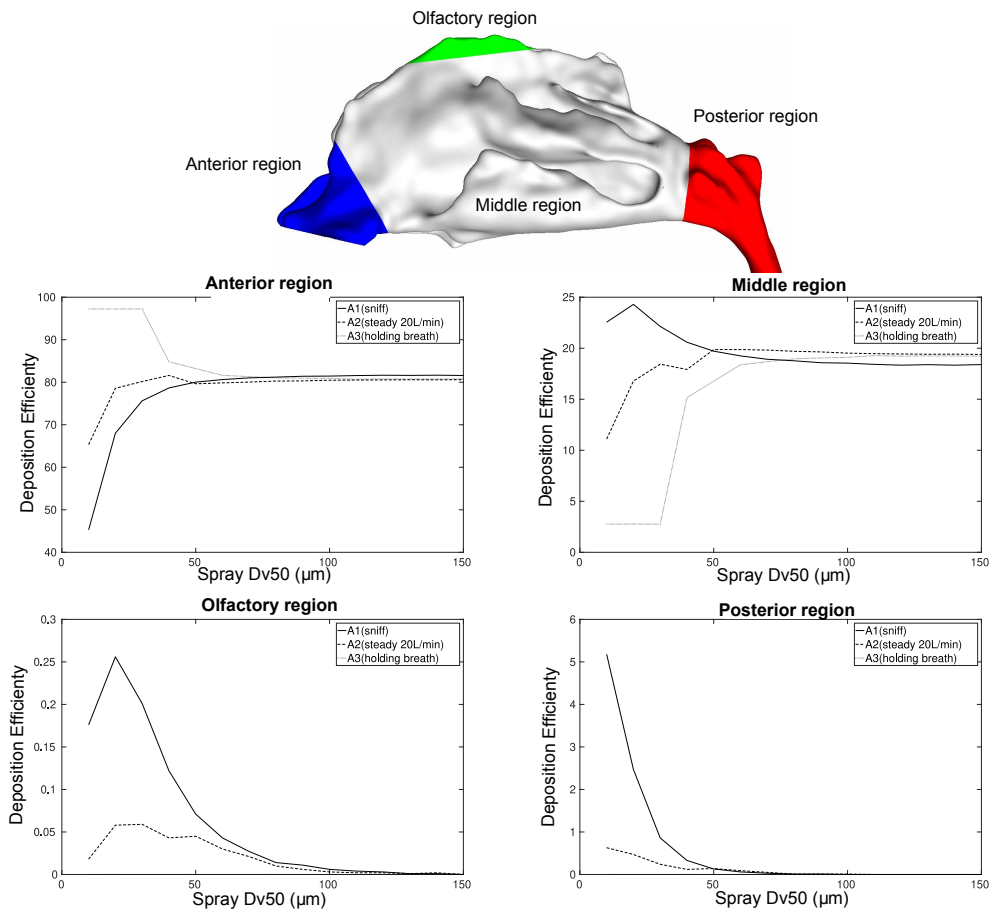
Figure 6.10: Regional deposition efficiency for the three inhalation conditions in function of particle size distribution $Dv50$.

The sniff condition produced greater scattering of particles followed by the constant inhalation, while the breath hold had no convective influence.

Deposition penetration

There is no established definition of where the anterior, middle, posterior boundaries are and in many cases these are arbitrarily defined. Therefore these boundaries can bias the reported deposition efficiency of the anterior and middle regions when there is high deposition clustered in the anterior half of the nasal cavity. The deposition pattern in Fig. 6.11 shows a near continuous region of particle deposition from the vestibule through to the middle nasal cavity region, and therefore deposition penetration can be used to demonstrate sprayed particle performance (Fig. 6.12). This was defined as the particles depositing in the regions between each slice in the axial flow direction. In all breathing conditions, peak deposition occurred between Slice 1 and 2. From Slice 2 to Slice 6, the deposition gradually decreased and a local maximum was found at Slice 7 to 8. This local maximum was caused by the presence of the turbinates in the airway passage increasing the local deposition. The deposition curves show $Dv50 < 50\mu m$ (red curves) had less deposition than $Dv50 > 50\mu m$ (blue curves) between slice 1-7. This was the opposite for slice 7-16 where the $Dv50 < 50\mu m$ had greater deposition than $Dv50 > 50\mu m$. With sniff and constant breath flow profiles Fig. 6.12(a) and (b) respectively the curves approximately collapsed until slice 7 then diverged, the logarithmic setting emphasises these differences.

Surface area deposition coverage

Targeted drug delivery for systemic action is most effective when drug particles can penetrate the highly vascularized main nasal passage surface. The surface area deposition coverage calculated from Eq 6.7 showed that when $Dv50 > 60\mu m$ the surface deposition was approximately 6cm^2, while for $Dv50 < 60\mu m$, the results exhibited increased deposition from sniffing, and constant flow breathing conditions with a maximum surface deposition of approximately 16cm^2 for $Dv50 = 20\mu m$. This is nearly three times the surface area coverage which could improve the therapeutic efficacy of drug delivery.
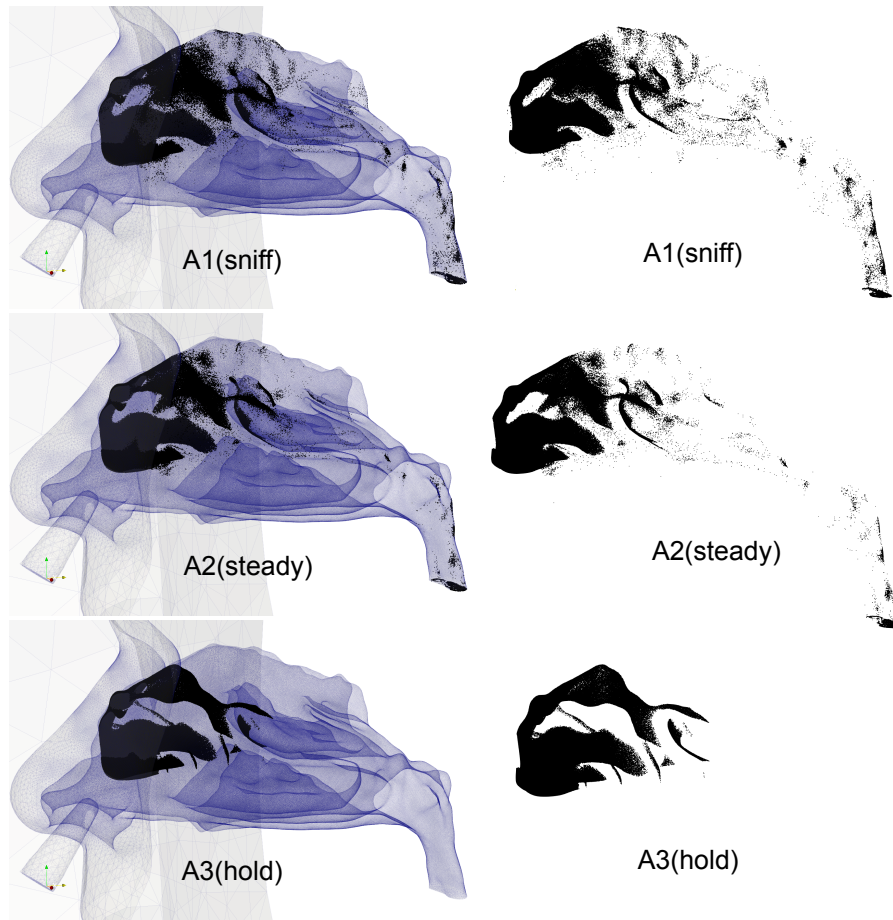
Figure 6.11: example of deposition pattern for the three inhalation conditions.
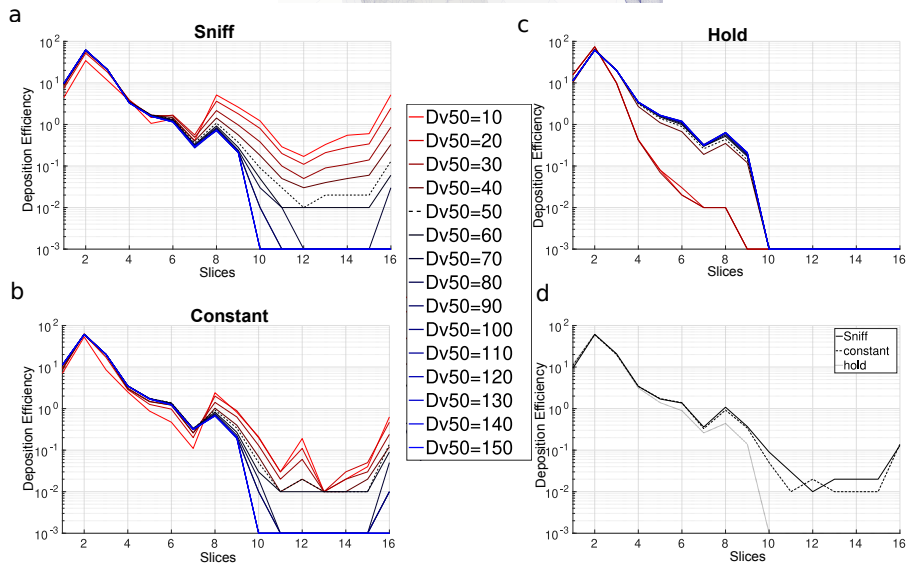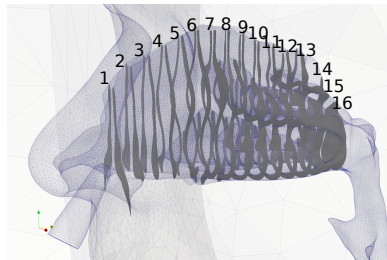
Figure 6.12: Particle deposition efficiency as a function of slice position; (a) to (c) corresponding to A1, A2 and A3 inhalation condition then (d) is the comparison of the three profile for $Dv50 = 50\mu m$.

89
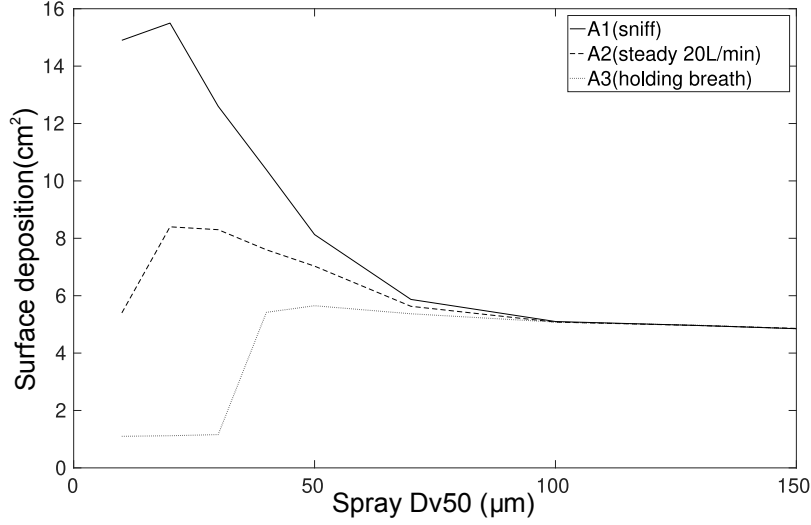
Figure 6.13: Surface deposition observed in the middle section.

Optimal configuration

To evaluate the best configuration of the nasal spray and inhalation condition an equation for an optimal combination was developed. Two parameters of interest are possible to define (P1 and P2) where a weighting (W1, and W2) is included for each parameter summing to a value of one, defined in Eq 6.8.

$$X = W_1 * \left(1 - \frac{Max(P_1) - P_1(D_{V50})}{Max(P_1)}\right) + W_2 * \left(1 - \frac{Max(P_2) - P_2(D_{V50})}{Max(P_2)}\right)$$
(6.8)

As an example of its application, Eq 6.8 was calculated for all volume median diameters, $Dv50$ and inhalation conditions, A1, A2, and A3. The two parameters chosen where P1 = surface area deposition coverage and P2 = deposition efficiency in the olfactory region (P2). For single parameters, W1 (or W2) is set to 1.0, and the remaining parameter is set to 0. The single parameter was not given as since the analysis can be deduced from Fig. 6.10 and 6.13. For the multi-parameter analysis, W1 = W2 = 0.5, although either weighting could be skewed up to a value of 1.0. The results are given Table 6.2 which shows that a $Dv50 = 20\mu m$ under sniffing condition (A1) provided the most effective strategy for maximum coverage deposition in the

90

D_{V50}	10	20	30	40	50	60	70	80	90	100	110	120	130	140	150
A1	0.82	1.00	0.80	0.57	0.40	0.31	0.24	0.20	0.19	0.18	0.17	0.16	0.16	0.16	0.16
A2	0.21	0.38	0.38	0.33	0.31	0.25	0.22	0.19	0.18	0.17	0.17	0.16	0.16	0.16	0.16
A3	0.04	0.04	0.04	0.17	0.18	0.18	0.17	0.17	0.17	0.16	0.16	0.16	0.16	0.16	0.16

Table 6.2: Optimal configuration in the olfactory region.

main nasal passage and a maximum deposition efficiency in olfactory region.

6.7 Summary

The deposition of polydisperse particles representing nasal spray application was performed under transient breathing profiles of sniffing, constant flow, and breath hold. Atomized particles emanating from a nasal spray device was represented by a polydisperse log-normal distribution. The spray nozzle was included in the geometry which created a realistic flow field in the anterior half of the nasal cavity. Of the three breathing profiles, the breath hold produced no transport due to the absence of fluid convection. The sniff condition, which exhibited peak flow of 57.4L/min produced the most significant reduction on anterior deposition. For monodisperse particles, sniff conditions increases the inertial parameter of a particle. However for polydisperse particles that have large proportion of particles with low inerital properties, the increased flow and turbulence can assist the transport of particles into the main nasal passage. The inertial parameter ($d_p^2 Q$) describes monodisperse micron deposition as a function of particle size (ie. diameter) to the square power, while the flow rate is to a linear power, thus the particle size is more important.

In monodisperse particles the cutoff value for 100% deposition efficiency was an inertial parameter of $10^5 \mu m^2 cm^3/s$. This study showed that a cutoff value also existed for polydisperse particle deposition. Constant deposition pattern, and efficiency that was independent of flow rate and profiles, was found when the particle size distribution $Dv50 = 50\mu m$.

The polydisperse particles under sniff conditions, produced an increase of 300% deposition in surface area coverage in the main nasal passage which is where the highly vascularised mucosal walls exist. Other targeted regions such as the olfactory region showed negligible deposition, thus the spray particle conditions is ineffective for olfactory deposition for possible drug delivery to the brain. The method presented allows any region to be targeted,

and therefore an optimisation equation was given to calculate the overall performance.

This study has produced the new deposition profiles for polydisperse particles. While a large set of parameters were evaluated (e.g. 15 particle size distributions, 3 breathing profiles, 4 regional deposition locations = 180 combinations), administration of nasal spray drug delivery presents a more parameters that were not considered. The LES modelling approach is very computationally intensive which makes it challenging for a massive parametrical study. In future larger patient samples, and spray parameters can be included for such studies to be evaluated.

Chapter 7

Conclusions

The purpose of this thesis was to explore the dynamics of unsteady flow in the large airways during a rapid inhalation through large-scale CFD on a highly-detailed geometry. Rapid inhalations are of relevance to sniffing for both olfaction and drug delivery of aerosols. The flow-rate considered (peak of $900mLs^{-1}$) corresponds to breathing at a somewhat elevated level but well below the transition from nasal to oro-nasal breathing. Resolving such flows poses a computational challenge and few previous attempts have been made to fully resolve the dynamics.

Furthermore, particle transport and deposition were investigated based on these dynamics of unsteady flow, revealing the role of filter playing by the nasal cavity for large particles (10 and 20 μm). On contrary, smaller particles (1 and 5 μm) with low inertia can penetrate further, along the respiratory tract even until the lungs. Some hot spots were observed, related to high turbulent activity, mainly located in the laryngeal region.

To finish, a drug delivery application was investigated. Nasal sprayed particle deposition in a human cavity under different inhalation conditions is presented.

Overall the key findings of this thesis can be summarised as follows:

- These simulations show that, despite the highly unsteady nature of the flow, the dominant features are established quite rapidly.

- It was also found that spontaneous fluctuations in nasal airflow velocities occur, resulting from shear layer instabilities (jet breakdown, flapping). The capture of these required the finest mesh resolution.

However the impact of these features on the fluctuation intensity was relatively low.

- High levels of wall-shear stress were observed where flow impacts on the nasal turbinates and in the confined space of the supra-glottic airway.

- Fourier spectral analysis showed that the spectrum of flow fluctuations in the nose is consistent with a transitional but not fully turbulent flow, being of limited bandwidth.

- The dominant pressure loss was associated with the laryngeal jet. The comparison of the pressure drop is very similar for 350 and 44 million elements but the mean pressure loss for the 44 million case is higher than that for the 350 million case.

- The turbulent flow in the laryngeal region is described, which is the dominant site of turbulence production. The spectral analysis demonstrates similarities to fully developed turbulence.

- The fluctuation level is decreasing as the flow progresses further downstream from the beginning of the trachea; approximately 10 cm appear sufficient to remove most fluctuations from the flow entering the bronchi.

- The nasal cavity is playing a role of particle filter due to the higher inertia for large particles (10 and 20 μm).

- On the other hand smaller particles (1 and 5 μm) with low inertia can penetrate further and have the tendency to be deposited more uniformly than larger particles along the respiratory tract even until the lungs.

- The turbulent flow in the laryngeal region highly promotes particle deposition.

- Olfactory region showed negligible deposition, thus the spray particle conditions is ineffective for olfactory deposition for possible drug delivery to the brain.

- The polydisperse particles under sniff condition, produced an increase of 300% deposition in surface area coverage compared with the different

94

inhalation conditions in the main nasal passage which is where the highly vascularised mucosal walls exist.

In this work, the complexity of a bio-engineering application was intended to be fully treated. It was made a series of assumptions and simplifications, leading to uncertainties.

Limitations of this study include the uniform initial particle velocity which in reality is subjected to velocity fluctuations. Furthermore, many nasal spray devices use a pressure-swirl atomizer [72] which implies some swirl component within the initial particle velocities. Discrete particles (non-deforming, inert, and no breakup or coalescence) were modeled with a one-way coupled assumption which provides simpler and efficient modeling. However, this may not be true in the near nozzle region of the spray device, because liquid sheets with peak mass loadings are present. Further downstream the coupling is not expected to be strong given that the concentration of particles become more disperse.

Result uncertainties are mainly physiological, physical and numerical. The physiological uncertainties come mostly from the difficulties in creating an accurate simulation scenario from patient and medical device data: the sniff flow rate, the particle distribution (size, density, shape), the geometrical setup defined from medical image, and others. Uncertainties on the physical side stem, for example; from the deposition model (deposition occurs once a particle touches the surface), the particle law of motion (selection of governing forces), the airflow-particle coupling (herein one-way), the airflow governing equations (incompressible flow with negligible heat transfer), the turbulence modeling (herein LES model), the air properties (viscosity, density), and others.

To assess the numerical uncertainties, consider the following; an exhaustive uncertainty analysis of physiological and physical aspects is almost impossible due to limited computational resources and is thus out of the scope of this thesis. However, some can be treated rather easily and are commonly used in such type of simulation. On the physiological side, a particle size distribution has been considered in Section 6.3. Once one has assumed the physiological and physical hypothesis delineate the scope of the study, one should control numerical uncertainties as much as possible to stay within the range established by the physical setup. Regarding the airflow, this was achieved through mesh convergence, as demonstrated in Section 6.2.

All the results presented in this thesis show the potential of large-scale

CFD simulations to further understanding of airway physiological mechanics and nasal drug delivery.

Bibliography

[1] K. Zhao, P. Dalton, G. C. Yang, P. W. Scherer, Numerical modeling of turbulent and laminar airflow and odorant transport during sniffing in the human and rat nose, Chemical senses 31 (2) (2006) 107–118.

[2] M. Se, K. Inthavong, J. Tu, Unsteady particle deposition in a human nasal cavity, in: Proceedings of the Seventh International Conference on CFD in the Minerals and Process Industries, CSIRO, 2009, pp. 1–6.

[3] J. Lindemann, T. Keck, K. Wiesmiller, B. Sander, H.-J. Brambs, G. Rettinger, D. Pless, Nasal air temperature and airflow during respiration in numerical simulation based on multislice computed tomography scan, American journal of rhinology 20 (2) (2006) 219–223.

[4] J.-H. Lee, Y. Na, S.-K. Kim, S.-K. Chung, Unsteady flow characteristics through a human nasal airway, Respiratory physiology & neurobiology 172 (3) (2010) 136–146.

[5] H. Bahmanzadeh, O. Abouali, M. Faramarzi, G. Ahmadi, Numerical simulation of airflow and micro-particle deposition in human nasal airway pre- and post-virtual sphenoidotomy surgery, Computers in Biology and Medicine 61 (2015) 8 – 18. `doi:https://doi.org/10.1016/j.compbiomed.2015.03.015`. URL `http://www.sciencedirect.com/science/article/pii/S0010482515000931`

[6] H. Calmet, A. Gambaruto, A. Bates, M. Vázquez, G. Houzeaux, D. Doorly, Large-scale CFD simulations of the transitional and turbulent regime for the large human airways during rapid inhalation, Computers in Biology and Medicine 69 (2016) 166–180. `doi:10.1016/j.compbiomed.2015.12.003`.

[7] A. J. Bates, A. Schuh, G. Amine-Eddine, K. McConnell, W. Loew, R. J. Fleck, J. C. Woods, C. L. Dumoulin, R. S. Amin, Assessing the relationship between movement and airflow in the upper airway using computational fluid dynamics with motion determined from magnetic resonance imaging, Clin Biomech (Bristol, Avon) 66 (2019) 88–96. `doi:10.1016/j.clinbiomech.2017.10.011`.

[8] J. Xi, J. Kim, X. A. Si, Effects of nostril orientation on airflow dynamics, heat exchange, and particle depositions in human noses, European Journal of Mechanics - B/Fluids 55, Part 1 (2016) 215–228. URL `http://www.sciencedirect.com/science/article/pii/S0997754615300960`

[9] J. H. Zhu, K. M. Lim, K. T. M. Thong, D. Y. Wang, H. P. Lee, Assessment of airflow ventilation in human nasal cavity and maxillary sinus before and after targeted sinonasal surgery: A numerical case study, Respiratory Physiology & Neurobiology 194 (2014) 29 – 36. `doi:https://doi.org/10.1016/j.resp.2014.01.004`. URL `http://www.sciencedirect.com/science/article/pii/S1569904814000056`

[10] I. Hörschler, M. Meinke, W. Schröder, Numerical simulation of the flow field in a model of the nasal cavity, Comp. Fluids 32 (1) (2003) 39–45.

[11] S. Naftali, M. Rosenfeld, M. Wolf, D. Elad, The air-conditioning capacity of the human nose, Annals of Biomedical Engineering 33 (2005) 545–553.

[12] P. Zamankhan, G. Ahmadi, Z. Wang, P. Hopke, Y.-S. Cheng, W. Chung Su, D. Leonard, Airflow and deposition of nano-particles in a human nasal cavity, Aerosol Science and Technology.

[13] J. H. Zhu, H. P. Lee, K. M. Lim, S. J. Lee, D. Y. Wang, Evaluation and comparison of nasal airway flow patterns among three subjects from caucasian, chinese and indian ethnic groups using computational fluid dynamics simulation, Respiratory Physiology & Neurobiology 175 (1) (2011) 62 – 69. `doi:https://doi.org/10.1016/j.resp.2010.09.008`. URL `http://www.sciencedirect.com/science/article/pii/S1569904810003642`

[14] A. Dastan, O. Abouali, G. Ahmadi, Cfd simulation of total and regional fiber deposition in human nasal cavities, Journal of Aerosol Science 69 (2014) 132 – 149. `doi:https://doi.org/10.1016/j.jaerosci.2013.12.008`.
URL `http://www.sciencedirect.com/science/article/pii/S0021850213002541`

[15] P. F. Ghalati, E. Keshavarzian, O. Abouali, A. Faramarzi, J. Tu, A. Shakibafard, Numerical analysis of micro- and nano-particle deposition in a realistic human upper airway, Computers in Biology and Medicine 42 (1) (2012) 39 – 49. `doi:https://doi.org/10.1016/j.compbiomed.2011.10.005`.
URL `http://www.sciencedirect.com/science/article/pii/S0010482511002010`

[16] J. X. Xi, J. Kim, X. H. A. Si, W. C. Su, Y. Zhou, Effects of the facial interface on inhalation and deposition of micrometer particles in calm air in a child airway model, Inhalation Toxicology 26 (8) (2014) 492–505.
URL `<GotoISI>://WOS:000339009600006`

[17] J. H. Zhu, H. P. Lee, K. M. Lim, S. J. Lee, L. T. L. San, D. Y. Wang, Inspirational airflow patterns in deviated noses: a numerical study, Computer Methods in Biomechanics and Biomedical Engineering 16 (12) (2013) 1298–1306, pMID: 22515677. `arXiv:https://doi.org/10.1080/10255842.2012.670850`, `doi:10.1080/10255842.2012.670850`.
URL `https://doi.org/10.1080/10255842.2012.670850`

[18] K. Inthavong, A. P. Mouritz, J. Dong, J. Y. Tu, Inhalation and deposition of carbon and glass composite fibre in the respiratory airway, Journal of Aerosol Science 65 (2013) 58 – 68. `doi:https://doi.org/10.1016/j.jaerosci.2013.07.003`.
URL `http://www.sciencedirect.com/science/article/pii/S0021850213001559`

[19] R. L. Walenga, G. Tian, M. Hindle, J. Yelverton, K. Dodson, P. W. Longest, Variability in nose-to-lung aerosol delivery, Journal of Aerosol Science 78 (2014) 11 – 29. `doi:https:`

//doi.org/10.1016/j.jaerosci.2014.08.003.
URL http://www.sciencedirect.com/science/article/pii/
S0021850214001281

[20] S.-K. Chung, G. Jo, S. K. Kim, Y. Na, The effect of a middle meatal antrostomy on nitric oxide ventilation in the maxillary sinus, Respiratory Physiology & Neurobiology 192 (2014) 7 – 16. doi:https://doi.org/10.1016/j.resp.2013.12.003.
URL http://www.sciencedirect.com/science/article/pii/
S156990481300390X

[21] Y. Zhang, Y. Shang, K. Inthavong, Z. Tong, B. Sun, K. Zhu, A. Yu, G. Zheng, Computational investigation of dust mite allergens in a realistic human nasal cavity, Inhalation Toxicology 31 (6) (2019) 224–235, pMID: 31431101. arXiv:https://doi.org/10.1080/08958378.
2019.1647315, doi:10.1080/08958378.2019.1647315.
URL https://doi.org/10.1080/08958378.2019.1647315

[22] I. Hörschler, C. Brücker, W. Schröder, M. Meinke, Investigation of the impact of the geometry on the nose flow, European Journal of Mechanics - B/Fluids 25 (4) (2006) 471 – 490. doi:https://doi.org/10.1016/j.euromechflu.2005.11.006.
URL http://www.sciencedirect.com/science/article/pii/
S0997754606000045

[23] J. Xi, P. W. Longest, Characterization of submicrometer aerosol deposition in extrathoracic airways during nasal exhalation, Aerosol Science and Technology 43 (8) (2009) 808–827. arXiv:https://doi.org/10.
1080/02786820902950887, doi:10.1080/02786820902950887.
URL https://doi.org/10.1080/02786820902950887

[24] N. L. Phuong, N. D. Khoa, K. Inthavong, K. Ito, Particle and inhalation exposure in human and monkey computational airway models, Inhalation Toxicology 30 (11-12) (2018) 416–428, pMID: 30618352. arXiv:
https://doi.org/10.1080/08958378.2018.1545810, doi:10.1080/
08958378.2018.1545810.
URL https://doi.org/10.1080/08958378.2018.1545810

[25] K. Inthavong, Q. Ge, C. M. K. Se, W. Yang, J. Y. Tu, Simulation of sprayed particle deposition in a human nasal cavity including a

nasal spray device, Journal of Aerosol Science 42 (2) (2011) 100–113.
doi:DOI:10.1016/j.jaerosci.2010.11.008.
URL   http://www.sciencedirect.com/science/article/
B6V6B-51N22D6-1/2/c10233d24d60c6f73ee29e3508b8d9db

[26] D. J. Doorly, D. J. Taylor, A. M. Gambaruto, R. C. Schroter, N. Tolley, Nasal architecture: Form and flow, Phil. Trans. Roy. Soc. A 366 (1879) (2008) 3225–3246.

[27] D. J. Doorly, D. J. Taylor, R. C. Schroter, Mechanics of airflow in the human nasal airways, Resp. Physiol. Neurobiol. 163 (1-3) (2008) 100–110.

[28] A. Lintermann, M. Meinke, W. Schröder, Fluid mechanics based classification of the respiratory efficiency of several nasal cavities, Computers in biology and medicine 43 (11) (2013) 1833–1852.

[29] D. J. Taylor, D. J. Doorly, R. C. Schroter, Inflow boundary profile prescription for numerical simulation of nasal airflow, Journal of the Royal Society Interface 7 (44) (2010) 515–527.

[30] S. T. Jayaraju, M. Brouns, C. Lacor, B. Belkassem, S. Verbanck, Large eddy and detached eddy simulations of fluid flow and particle deposition in a human mouth–throat, Journal of Aerosol Science 39 (10) (2008) 862–875.

[31] C. G. Ball, M. Uddin, A. Pollard, Mean flow structures inside the human upper airway, Flow, Turbulence and Combustion 81 (1-2) (2008) 155–188.

[32] E. Ghahramani, O. Abouali, H. Emdad, G. Ahmadi, Numerical analysis of stochastic dispersion of micro-particles in turbulent flows in a realistic model of human nasal/upper airway, Journal of Aerosol Science 67 (2014) 188–206.

[33] P. H. Saksono, P. Nithiarasu, I. Sazonov, S. Y. Yeo, Computational flow studies in a subject-specific human upper airway using a one-equation turbulence model. influence of the nasal cavity, International Journal for Numerical Methods in Engineering 87 (1-5) (2011) 96–114.

[34] C. L. Lin, M. H. Tawhai, G. McLennan, E. A. Hoffman, Characteristics of the turbulent laryngeal jet and its effect on airflow in the human intra-thoracic airways, Respiratory physiology & neurobiology 157 (2) (2007) 295–309.

[35] D. Elad, S. Naftali, M. Rosenfeld, M. Wolf, Physical stresses at the air-wall interface of the human nasal cavity during breathing, Journal of Applied Physiology 100 (3) (2006) 1003–1010.

[36] J. Choi, M. H. Tawhai, E. A. Hoffman, C. L. Lin, On inter- and intra-subject variabilities of airflow in the human lungs, Physics of Fluids 21 (101901).

[37] S. S. Varghese, S. H. Frankel, P. Fischer, Direct numerical simulation of stenotic flows. part 1. steady flow, Journal of Fluid Mechanics 582 (2007) 253–280.

[38] E. Buijs, V. Covello, C. Pipolo, A. Saibene, G. Felisati, M. Quadrio, Thermal water delivery in the nose: experimental results describing droplet deposition through computational fluid dynamics, ACTA Otorhinolaryngologica Italica.

[39] Y. Shang, K. Inthavong, J. Tu, Development of a computational fluid dynamics model for mucociliary clearance in the nasal cavity, Journal of biomechanics 85 (2019) 74–83.

[40] I. Balásházy, W. Hofmann, T. Heistracher, Local particle deposition patterns may play a key role in the development of lung cancer, Journal of Applied Physiology 94 (5) (2003) 1719–1725.

[41] J. Kesavanathan, D. L. Swift, Human nasal passage particle deposition: the effect of particle size, flow rate, and anatomical factors, Aerosol Science and Technology 28 (5) (1998) 457–463.

[42] J. Kesavanathan, R. Bascom, D. L. Swift, The effect of nasal passage characteristics on particle deposition, Journal of aerosol medicine 11 (1) (1998) 27–39.

[43] J. Kesavan, R. Bascom, B. Laube, D. L. Swift, The relationship between particle deposition in the anterior nasal passage and nasal passage characteristics, Journal of Aerosol Medicine 13 (1) (2000)

17–23. `doi:10.1089/jam.2000.13.17`.
URL `http://www.liebertonline.com/doi/abs/10.1089/jam.2000.13.17`

[44] Y. S. Cheng, Aerosol deposition in the extrathoracic region, Aerosol Science & Technology 37 (8) (2003) 659–671.

[45] Y. S. Cheng, T. D. Holmes, J. Gao, R. A. Guilmette, S. Li, Y. Surakitbanharn, C. Rowlings, Characterization of nasal spray pumps and deposition pattern in a replica of the human nasal airway, Journal of Aerosol Medicine 14 (2) (2001) 267–280.

[46] K. H. Cheng, Y. S. Cheng, H. C. Yeh, D. L. Swift, Deposition of ultrafine aerosols in the head airways during natural breathing and during simulated breath holding using replicate human upper airway casts, Aerosol science and technology 23 (3) (1995) 465–474.

[47] H. Calmet, C. Kleinstreuer, G. Houzeaux, A. Kolanjiyil, O. Lehmkuhl, E. Olivares, M. Vázquez, Subject-variability effects on micron particle deposition in human nasal cavities, Journal of Aerosol Science 115 (2018) 12–28. `doi:10.1016/j.jaerosci.2017.10.008`.

[48] P. F. Ghalati, E. Keshavarzian, O. Abouali, A. Faramarzi, J. Tu, A. Shakibafard, Numerical analysis of micro-and nano-particle deposition in a realistic human upper airway, Computers in Biology and Medicine 42 (1) (2012) 39–49.

[49] A. V. Kolanjiyil, C. Kleinstreuer, Nanoparticle mass transfer from lung airways to systemic regions–part i: Whole-lung aerosol dynamics, Journal of Biomechanical Engineering 135 (12) (2013) 121003. `doi:10.1115/1.4025332`.
URL `http://www.ncbi.nlm.nih.gov/pubmed/24008503`

[50] H. Shi, C. Kleinstreuer, Z. Zhang, Dilute suspension flow with nanoparticle deposition in a representative nasal airway model, Physics of Fluids 20 (1) (2008) 013301.

[51] H. Shi, C. Kleinstreuer, Z. Zhang, Modeling of inertial particle transport and deposition in human nasal cavities with wall roughness, Journal of Aerosol Science 38 (4) (2007) 398–419.

103

[52] Z. Zhang, C. Kleinstreuer, Computational analysis of airflow and nanoparticle deposition in a combined nasal–oral–tracheobronchial airway model, Journal of Aerosol Science 42 (3) (2011) 174–194.

[53] H. Bahmanzadeh, O. Abouali, G. Ahmadi, Unsteady particle tracking of micro-particle deposition in the human nasal cavity under cyclic inspiratory flow, Journal of Aerosol Science 101 (2016) 86–103.

[54] K. Zhao, P. W. Scherer, S. A. Hajiloo, P. Dalton, Effect of anatomy on human nasal air flow and odorant transport patterns: implications for olfaction, Chemical senses 29 (5) (2004) 365–379.

[55] G. J. M. Garcia, J. D. Schroeter, J. S. Kimbell, Olfactory deposition of inhaled nanoparticles in humans, Inhalation toxicology 27 (8) (2015) 394–403.

[56] I. Hahn, P. W. Scherer, M. M. Mozell, Velocity profiles measured for airflow through a large-scale model of the human nasal cavity, Journal of Applied Physiology 75 (5) (1993) 2273–2287.

[57] A. A. Hussain, Mechanism of nasal absorption of drugs, Prog Clin Biol Res 292 (1989) 261–272.

[58] L. Illum, Nasal drug delviery: new developments and strategies, Drug Discovery Today 7 (23) (2002) 1184–1189.

[59] K. Inthavong, Z. F. Tian, J. Y. Tu, W. Yang, C. Xue, Optimising nasal spray parameters for efficient drug delivery using computational fluid dynamics, Computers in Biology and Medicine 38 (6) (2008) 713–726.

[60] X. Tong, J. Dong, Y. Shang, K. Inthavong, J. Tu, Effects of nasal drug delivery device and its orientation on sprayed particle deposition in a realistic human nasal cavity, Computers in biology and medicine 77 (2016) 40–48.

[61] Y. Guo, B. Laube, R. Dalby, The effect of formulation variables and breathing patterns on the site of nasal deposition in an anatomically correct model., Pharmaceutical Research 22 (2005) 1871–1878.

104

[62] M. Y. Foo, Y. S. Cheng, W. C. Su, M. D. Donovan, The influence of spray properties on intranasal deposition, J Aerosol Med 20 (4) (2007) 495–508. doi:10.1089/jam.2007.0638.

[63] N. Sawant, M. D. Donovan, In Vitro Assessment of Spray Deposition Patterns in a Pediatric (12 Year-Old) Nasal Cavity Model, Pharmaceutical Research 35 (5) (2018) 108. doi:10.1007/s11095-018-2385-6.
URL https://doi.org/10.1007/s11095-018-2385-6

[64] Y. Pu, A. P. Goodey, X. Fang, K. Jacob, A Comparison of the Deposition Patterns of Different Nasal Spray Formulations Using a Nasal Cast, Aerosol Science and Technology 48 (9) (2014) 930–938. doi:10.1080/02786826.2014.931566.
URL https://doi.org/10.1080/02786826.2014.931566

[65] Z. N. Warnken, H. D. C. Smyth, D. A. Davis, S. Weitman, J. G. Kuhn, R. O. Williams, Personalized Medicine in Nasal Delivery: The Use of Patient-Specific Administration Parameters To Improve Nasal Drug Targeting Using 3D-Printed Nasal Replica Casts, Molecular Pharmaceutics 15 (4) (2018) 1392–1402. doi:10.1021/acs.molpharmaceut.7b00702.
URL https://doi.org/10.1021/acs.molpharmaceut.7b00702

[66] M. C. Fung, K. Inthavong, W. Yang, P. Lappas, J. Tu, External characteristics of unsteady spray atomization from a nasal spray device, Journal of Pharmaceutical Sciences 102 (3) (2013) 1024–1035. doi:10.1002/jps.23449.
URL https://www.scopus.com/inward/record.uri?eid=2-s2.0-84878149537&doi=10.1002%2fjps.23449&partnerID=40&md5=99a02873895e5306be77d7dd5b6dca2d

[67] K. Inthavong, M. C. Fung, W. Yang, J. Tu, Measurements of droplet size distribution and analysis of nasal spray atomization from different actuation pressure, Journal of aerosol medicine and pulmonary drug delivery.

[68] S. P. Newman, G. R. Pitcairn, R. N. Dalby, Drug delivery to the nasal cavity: In vitro and in vivo assessment, Critical Reviews™ in Therapeutic Drug Carrier Systems 21 (1) (2004) 46. doi:10.1615/CritRevTherDrugCarrierSyst.v21.i1.20.

URL http://dl.begellhouse.com/journals/3667c4ae6e8fd136,
58a387242a6d577c,51acf51f3b6704cf.html

[69] J. S. Kimbell, R. A. Segal, B. Asgharian, B. A. Wong, J. D. Schroeter, J. P. Southall, C. J. Dickens, G. Brace, F. J. Miller, Characterization of deposition from nasal spray devices using a computational fluid dynamics model of the human nasal passages, Journal Aeros. Medicine 20 (1) (2007) 59–74.

[70] J. A. Keeler, A. Patki, C. R. Woodard, D. O. Frank-Ito, A Computational Study of Nasal Spray Deposition Pattern in Four Ethnic Groups, Journal of Aerosol Medicine and Pulmonary Drug Delivery 29 (2) (2016) 153–166. doi:10.1089/jamp.2014.1205.
URL http://www.ncbi.nlm.nih.gov/pmc/articles/PMC4855781/

[71] M. Kiaee, H. Wachtel, M. L. Noga, A. R. Martin, W. H. Finlay, Regional deposition of nasal sprays in adults: A wide ranging computational study, International Journal for Numerical Methods in Biomedical Engineering 34 (5) (2018) n/a–n/a. doi:10.1002/cnm.2968.

[72] M. C. Fung, K. Inthavong, W. Yang, J. Tu, CFD Modeling of Spray Atomization for a Nasal Spray Device, Aerosol Science and Technology 46 (11) (2012) 1219–1226. doi:10.1080/02786826.2012.704098.
URL http://dx.doi.org/10.1080/02786826.2012.704098

[73] P. Djupesland, A. Skretting, M. Winderen, T. Holand, Bi-directional nasal delivery of aerosols can prevent lung deposition, Journal Aerosol Med 17 (2004) 249–259. doi:10.1089/jam.2004.17.249.

[74] K. Inthavong, Z. F. Tian, H. F. Li, J. Y. Tu, W. Yang, C. L. Xue, C. G. Li, A numerical study of spray particle deposition in a human nasal cavity., Aerosol Science and Technology 40 (11) (2006) 1034–1045.

[75] Y. Liu, E. Matida, J. Gu, M. Johnson, Numerical simulation of aerosol deposition in a 3-d human nasal cavity using rans, rans/eim, and les, Journal of Aerosol Science 38 (2007) 683–700. doi:10.1016/j.jaerosci.2007.05.003.

[76] E. Matida, W. Finlay, C. Lange, B. Grgic, Improved numerical simulation of aerosol deposition in an idealized

mouth–throat, Journal of Aerosol Science 35 (1) (2004) 1 – 19. doi:https://doi.org/10.1016/S0021-8502(03)00381-1.
URL http://www.sciencedirect.com/science/article/pii/S0021850203003811

[77] K. Inthavong, J. Tu, C. Heschl, Micron particle deposition in the nasal cavity using the v2–f model, Computers & Fluids 51 (1) (2011) 184 – 188. doi:https://doi.org/10.1016/j.compfluid.2011.08.013.
URL http://www.sciencedirect.com/science/article/pii/S0045793011002568

[78] A. Farnoud, X. Cui, I. Baumann, E. Gutheil, Numerical simulation of the dispersion and deposition of a spray carried by a pulsating airflow in a patient-specific human nasal cavity, Atomization and Sprays 27 (11).

[79] R. Payri Marín, M. Xandra Marcelle, Ilass europe. 28th european conference on liquid atomization and spray systems, in: Colección Congreso, Editorial Universitat Politècnica de València, 2017.

[80] V. Covello, C. Pipolo, A. Saibene, G. Felisati, M. Quadrio, Numerical simulation of thermal water delivery in the human nasal cavity, Computers in Biology and Medicine 100 (2018) 62 – 73. doi:https://doi.org/10.1016/j.compbiomed.2018.06.029.
URL http://www.sciencedirect.com/science/article/pii/S001048251830177X

[81] G. Mylavarapu, S. Murugappan, M. Mihaescu, M. Kalra, S. Khosla, E. Gutmark, Validation of computational fluid dynamics methodology used for human upper airway flow simulations, Journal of Biomechanics 42 (10) (2009) 1553 – 1559. doi:https://doi.org/10.1016/j.jbiomech.2009.03.035.
URL http://www.sciencedirect.com/science/article/pii/S0021929009001341

[82] C. Li, J. Jiang, H. Dong, K. Zhao, Computational modeling and validation of human nasal airflow under various breathing conditions, Journal of Biomechanics 64 (2017) 59 – 68. doi:https://doi.org/10.1016/j.jbiomech.2017.08.031.
URL http://www.sciencedirect.com/science/article/pii/S0021929017304542

[83] M. Vázquez, G. Houzeaux, S. Koric, A. Artigues, J. Aguado-Sierra, R. Ar\'\is, D. Mira, H. Calmet, F. Cucchietti, H. Owen, Others, Alya: Multiphysics engineering simulation toward exascale, Journal of Computational Science 14 (2016) 15–27.

[84] A. J. Bates, D. J. Doorly, R. Cetto, H. Calmet, A. M. Gambaruto, N. S. Tolley, G. Houzeaux, R. C. Schroter, Dynamics of airflow in a short inhalationand, J. R. Soc. Interface.

[85] G. Taubin, Curve and surface smoothing without shrinkage, in: Computer Vision, 1995. Proceedings., Fifth International Conference on, IEEE, 1995, pp. 852–857.

[86] D. A. Field, Laplacian smoothing and delaunay triangulations, Communications in applied numerical methods 4 (6) (1988) 709–712.

[87] http://148.204.81.206/Ansys/150/ANSYSMeshingUsersGuide.pdf (2000).

[88] S. K. Robinson, Coherent motions in the turbulent boundary layer, Annual Review of Fluid Mechanics 23 (1) (1991) 601–639.

[89] U. Piomelli, E. Balaras, Wall-layer models for large-eddy simulations, Annual review of fluid mechanics 34 (1) (2002) 349–374.

[90] G. Houzeaux, R. de la Cruz, H. Owen, M. Vázquez, Parallel uniform mesh multiplication applied to a navier–stokes solver, Computers & Fluids 80 (2013) 142–151.

[91] http://www.bsc.es/computer-applications/alya-system (2000).

[92] C. O, S. Badia, R. Codina, J. Principe, Assessment of variational multiscale models for the large eddy simulation of turbulent incompressible flows, Computer Methods in Applied Mechanics and Engineering 285 (2015) 32–63.

[93] G. Houzeaux, J. Principe, A variational subgrid scale model for transient incompressible flows, IJCFD 22 (3) (2008) 135–152.

[94] G. Houzeaux, R. Aubry, M. Vázquez, Extension of fractional step techniques for incompressible flows: The preconditioned orthomin(1) for

the pressure schur complement, Computers & Fluids 44 (2011) 297–313. `doi:DOI:10.1016/j.compfluid.2011.01.017`.

[95] R. Lohner, F. Mut, J. Cebral, R. Aubry, G. Houzeaux, Deflated preconditioned conjugate gradient solvers for the pressure-poisson equation: Extensions and improvements, Int. J. Numer. Meth. Engn. 87 (2011) 2–14.

[96] O. Soto, R. Löhner, F. Camelli, A linelet preconditioner for incompressible flow solvers, Int. J. Num. Meth. Heat Fluid Flow 13 (1) (2003) 133–147.

[97] G. Karypis, Metis: Serial graph partitioning and fill-reducing matrix ordering, available at: `http://glaros.dtc.umn.edu/gkhome/views/metis` (1995–2015).

[98] M. Folk, A. Cheng, K. Yates, Hdf5: A file format and i/o library for high performance computing applications, in: Proceedings of Supercomputing, Vol. 99, 1999, pp. 5–33.

[99] P. Corbett, D. Feitelson, S. Fineberg, Y. Hsu, B. Nitzberg, J.-P. Prost, M. Snir, B. Traversat, P. Wong, Overview of the mpi-io parallel i/o interface, in: IPPS'95 Workshop on Input/Output in Parallel and Distributed Systems, 1995, pp. 1–15.

[100] G. Houzeaux, M. Garcia, J. C. Cajas, A. Artigues, E. Olivares, J. Labarta, M. Vázquez, Dynamic load balance applied to particle transport in fluids, International Journal of Computational Fluid Dynamics 30 (6) (2016) 408–418.

[101] G. Ganser, A rational approach to drag prediction of spherical and nonspherical particles, Powder Technology 77 (1993) 143–152.

[102] G. Houzeaux, M. Garcia-Gasulla, J. C. Cajas, A. Artigues, E. Olivares, J. Labarta, M. Vázquez, Dynamic load balance applied to particle transport in fluids, Int. J. Comp. Fluid Dyn.

[103] C. E. Rennie, K. A. Gouder, D. J. Taylor, N. S. Tolley, R. C. Schroter, D. J. Doorly., Nasal inspiratory flow: at rest and sniffing., Int Forum Allergy Rhinol 1 (2) (2011) 128–135.

[104] H. Shi, C. Kleinstreuer, Z. Zhang, Modeling of inertial particle transport and deposition in human nasal cavities with wall roughness, Journal of Aerosol Science 38 (4) (2007) 398–419.

[105] J. T. Kelly, B. Asgharian, J. S. Kimbell, B. A. Wong, Particle deposition in human nasal airway replicas manufactured by different methods. Part I: Inertial regime particles, Aerosol Science and Technology 38 (11) (2004) 1063–1071.

[106] D. J. Hsu, M. H. Chuang, In-vivo measurements of micrometer-sized particle deposition in the nasal cavities of taiwanese adults, Aerosol Science and Technology 46 (6) (2012) 631–638. `doi:Doi10.1080/02786826.2011.652749.`
URL `<GotoISI>://WOS:000301773000004`

[107] J. D. Schroeter, G. J. M. Garcia, J. S. Kimbell, Effects of surface smoothness on inertial particle deposition in human nasal models, Journal of Aerosol Science 42 (1) (2011) 52–63. `doi:DOI:10.1016/j.jaerosci.2010.11.002.`
URL `http://www.sciencedirect.com/science/article/B6V6B-51M0NFD-1/2/4fe969fff47505f8d54bcd8dae1ee0ff`

[108] Y. D. Shang, K. Inthavong, J. Y. Tu, Detailed micro-particle deposition patterns in the human nasal cavity influenced by the breathing zone, Computers and Fluids 114 (2015) 141–150.

[109] H. Shi, C. Kleinstreuer, Z. Zhang, Modeling of inertial particle transport and deposition in human nasal cavities with wall roughness, Journal of Aerosol Science 38 (4) (2007) 398–419.
URL `http://www.sciencedirect.com/science/article/B6V6B-4N3WYPX-2/2/9709080f5ffc9deee53f3dc1b850c529`

[110] H. Bahmanzadeh, O. Abouali, M. Faramarzi, G. Ahmadi, Numerical simulation of airflow and micro-particle deposition in human nasal airway pre-and post-virtual sphenoidotomy surgery, Computers in biology and medicine 61 (2015) 8–18.

[111] E. Ghahramani, O. Abouali, H. Emdad, G. Ahmadi, Numerical investigation of turbulent airflow and microparticle deposition in a realistic

model of human upper airway using les, Computers & Fluids 157 (2017) 43–54.

[112] H. Shi, C. Kleinstreuer, Z. Zhang, Dilute suspension flow with nanoparticle deposition in a representative nasal airway model, Physics of Fluids (1994-present) 20 (1) (2008) 13301.

[113] B. M. Sumer, et al., Hydrodynamics around cylindrical strucures, Vol. 26, World scientific, 2006.

[114] J. C. R. Hunt, Vorticity and vortex dynamics in complex turbulent flows, in: Canadian Society for Mechanical Engineering, Transactions (ISSN 0315-8977), vol. 11, no. 1, 1987, p. 21-35., Vol. 11, 1987, pp. 21–35.

[115] P. Ligrani, R. Niver, Flow visualization of dean vortices in a curved channel with 40 to 1 aspect ratio, The Physics of fluids 31 (12) (1988) 3605–3617.

[116] D. C. Wilcox, Others, Turbulence modeling for CFD, Vol. 2, DCW industries La Canada, CA, 1998.

[117] A. M. Gambaruto, D. J. Taylor, D. J. Doorly, Modelling nasal airflow using a fourier descriptor representation of geometry, IJNMF 59 (11) (2009) 1259–1283.

[118] S. T. Jayaraju, M. Brouns, S. Verbanck, C. Lacor, Fluid flow and particle deposition analysis in a realistic extrathoracic airway model using unstructured grids, Journal of Aerosol Science 38 (5) (2007) 494–508.

[119] A. M. Gambaruto, D. J. Doorly, T. Yamaguchi, Wall shear stress and near-wall convective transport: Comparisons with vascular remodelling in a peripheral graft anastomosis, Journal of Computational Physics 229 (14) (2010) 5339–5356.

[120] S. B. Pope, Turbulent flows, Cambridge university press, 2000.

[121] S. G. Saddoughi, S. V. Veeravalli, Local isotropy in turbulent boundary layers at high reynolds number, Journal of Fluid Mechanics 268 (1994) 333–372.

[122] M. K. Bang, H. C. William, Experimental measurements of turbulence spectra distal to stenoses, Journal of Biomechanics 7 (4) (1974) 335 – 342. `doi:http://dx.doi.org/10.1016/0021-9290(74)90028-1`.

[123] J. Tu, K. Inthavong, G. Ahmadi, Computational fluid and particle dynamics in the human respiratory system, Springer, 2012.

[124] F. Nicoud, F. Ducros, Subgrid-scale stress modelling based on the square of the velocity gradient tensor, Flow, Turbulence and Combustion 62 (3) (1999) 183–200. `arXiv:arXiv:1503.01439v1`, `doi:10.1023/A:1009995426001`.

[125] P. Koullapis, S. C. Kassinos, J. Muela, C. Perez-segarra, J. Rigola, O. Lehmkuhl, Y. Cui, M. Sommerfeld, J. Elcner, M. Jicha, I. Saveljic, N. Filipovic, F. Lizal, L. Nicolaou, Regional aerosol deposition in the human airways : The SimInhale benchmark case and a critical assessment of in silico methods, European Journal of Pharmaceutical Sciences (June). `doi:10.1016/j.ejps.2017.09.003`.

[126] R. W. C. P. Verstappen, A. E. P. Veldman, Symmetry-preserving discretization of turbulent flow, Journal of Computational Physics 187 (1) (2003) 343–368. `doi:10.1016/S0021-9991(03)00126-8`.

[127] F. X. Trias, O. Lehmkuhl, A. Oliva, C. D. Pérez-Segarra, R. W. C. P. Verstappen, Symmetry-preserving discretization of Navier-Stokes equations on collocated unstructured grids, Journal of Computational Physics 258 (2014) 246–267. `doi:10.1016/j.jcp.2013.10.031`. URL `http://dx.doi.org/10.1016/j.jcp.2013.10.031`

[128] L. Jofre, O. Lehmkuhl, J. Ventosa, F. X. Trias, A. Oliva, Conservation Properties of Unstructured Finite-Volume Mesh Schemes for the Navier-Stokes Equations, Numerical Heat Transfer, Part B: Fundamentals 65 (August) (2013) 53–79. `doi:10.1080/10407790.2013.836335`. URL `http://www.tandfonline.com/doi/abs/10.1080/10407790.2013.836335`

[129] F. Capuano, G. Coppola, L. Rández, L. D. Luca, Explicit Runge – Kutta schemes for incompressible flow with improved energy-conservation properties, Journal of Computational Physics 328 (2017)

86–94. `doi:10.1016/j.jcp.2016.10.040`.
URL `http://dx.doi.org/10.1016/j.jcp.2016.10.040`

[130] F. X. Trias, O. Lehmkuhl, A Self-Adaptive Strategy for the Time Integration of Navier-Stokes Equations, Numerical Heat Transfer, Part B: Fundamentals 60 (July 2013) (2011) 116–134. `doi:10.1080/10407790.2011.594398`.
URL `http://www.tandfonline.com/doi/abs/10.1080/10407790.2011.594398`

[131] S. B. Pope, Turbulent flows (2001).

[132] H. Tennekes, J. L. Lumley, A first course in turbulence, MIT press, 1972.

[133] M. C. Fung, K. Inthavong, W. Yang, P. Lappas, J. Tu, External characteristics of unsteady spray atomization from a nasal spray device, Journal of Pharmaceutical Sciences (2013) n/a–n/a`doi:10.1002/jps.23449`.
URL `http://dx.doi.org/10.1002/jps.23449`

[134] K. Inthavong, M. C. Fung, X. Tong, W. Yang, J. Tu, High Resolution Visualization and Analysis of Nasal Spray Drug Delivery, Pharmaceutical Research (2014) 1–8`doi:10.1007/s11095-013-1294-y`.
URL `http://www.scopus.com/inward/record.url?eid=2-s2.0-84893840642{&}partnerID=40{&}md5=40fcee0ed780618cb649030f15d3ca44`

[135] K. Inthavong, M. C. Fung, W. Yang, J. Tu, Measurements of droplet size distribution and analysis of nasal spray atomization from different actuation pressure, Journal of Aerosol Medicine and Pulmonary Drug Delivery 28 (1) (2015) 59–67. `doi:10.1089/jamp.2013.1093`.
URL `http://www.scopus.com/inward/record.url?eid=2-s2.0-84922553348{&}partnerID=40{&}md5=5ddcb9842f582cd0576cb59acef6310e`

[136] K. Inthavong, W. Yang, M. C. Fung, J. Y. Tu, External and Near-Nozzle Spray Characteristics of a Continuous Spray Atomized from a Nasal Spray Device, Aerosol Science and Technology 46 (2) (2012) 165–177. `doi:10.1080/02786826.2011.617793`.
URL `http://dx.doi.org/10.1080/02786826.2011.617793`

[137] S. Basu, D. O. Frank-Ito, J. S. Kimbell, On computational fluid dynamics models for sinonasal drug transport: Relevance of nozzle subtraction and nasal vestibular dilation, International Journal for Numerical Methods in Biomedical Engineering 34 (4) (2017) e2946. `doi:10.1002/cnm.2946`.
URL `https://onlinelibrary.wiley.com/doi/abs/10.1002/cnm.2946`

[138] G. J. M. Garcia, J. D. Schroeter, R. A. Segal, J. Stanek, G. L. Foureman, J. S. Kimbell, Dosimetry of nasal uptake of water-soluble and reactive gases: A first study of interhuman variability, Inhalation Toxicology 21 (7) (2009) 607–618. `doi:10.1080/08958370802320186`.
URL `https://doi.org/10.1080/08958370802320186`

[139] M. S. Benninger, J. A. Hadley, J. D. Osguthorpe, B. F. Marple, D. A. Leopold, M. J. Derebery, M. Hannley, Techniques of intranasal steroid use, Otolaryngology-Head and Neck Surgery 130 (1) (2004) 5–24.

[140] H. Calmet, G. Houzeaux, M. Vázquez, B. Eguzkitza, A. Gambaruto, A. Bates, D. Doorly, Flow features and micro-particle deposition in a human respiratory system during sniffing, Journal of Aerosol Science 123 (2018) 171–184. `doi:10.1016/j.jaerosci.2018.05.008`.

Appendix

Point coordinates. The list of points used in this study, is given in the table 7.1. The points are normalised by the tip of the nose which here is considered to be the point 1.

Points	Coordinate X(m)	Coordinate Y(m)	Coordinate Z(m)
1	0.0	0.0	0.0
2	-0.1060	0.0484	0.0090
3	-0.0086	0.0487	0.0196
3A	-0.0073	0.0564	0.0273
3B	-0.0084	0.0501	0.0210
4	-0.0082	0.1256	0.0061
5	-0.0023	0.1379	-0.0104
7	0.0009	0.1500	-0.0704
8	0.0013	0.1437	-0.1123
9	-0.0061	0.1553	-0.1304
10	-0.0028	0.1735	-0.1504
11	-0.0052	0.1867	-0.1704
12	-0.0068	0.2024	-0.2046
13	-0.0394	0.2069	-0.2046

Table 7.1: Coordinates of the points in Figure 2.2 relative to the tip of nose.

Modelling of the sniff. To model the sniff inflow, we use a polynomial function of order 10 derived from the experimental work detailed in Rennie et al. [103]. The 10th order polynomial function describing the temporal evolution of the flow rate is provided in Figure 2.3.

Order	Coefficient
0	0.0015
1	0.6813
2	472.2648
3	-10790.8421
4	114269.4525
5	705483.2425
6	2736179.6777
7	-6773661.0554
8	10395525.1742
9	-9007136.2292
10	3364786.7418

Table 7.2: Coefficient values of the 10th order polynomial function

Medical case. A short description of the medical case is given bellow. A consultant radiologist reported the nasal airways as clear and of normal appearance. The position of the tongue base and other soft tissues in the pharynx were deemed consistent with the patient being scanned in the supine position. The vocal cords were noted to have the appearance of being abducted, whereas the trachea was considered to be of normal dimensions, not demonstrating any abnormalities. The airway in the pharynx may be narrower than if the patient had been standing, but the geometry is within the normal range.

TKE along the upper airway. TKE is calculated with the area-average of TKE of each slice during the plateau phase of [0.1-0.15 s]. The scale of TKE for the nasal cavity are low (less than 0.5). In contrary for the rest of the upper airway, the values of TKE are significantly high, emphasizing the transitional-turbulent state of the airflow.

Figure 7.1: Cross-sectional-area-average of TKE (m^2/s^2) along the airway during the plateau phase of [0.1-0.15 s].

Acknowledgements